

Institutionen för systemteknik

Department of Electrical Engineering

Examensarbete

Improved Temporal Resolution Using Parallel Imaging in Radial-Cartesian 3D functional MRI

Examensarbete utfört i bildbehandling
vid Tekniska högskolan vid Linköpings Universitet
av

Gustav Ahlman

LiTH-ISY-EX--11/4470--SE

Linköping 2011



Linköpings universitet

TEKNISKA HÖGSKOLAN

Department of Electrical Engineering
Linköping University
S-581 83 Linköping, Sweden

Linköpings tekniska högskola
Institutionen för systemteknik
581 83 Linköping

Improved Temporal Resolution Using Parallel Imaging in Radial-Cartesian 3D functional MRI

Examensarbete utfört i bildbehandling
vid Tekniska högskolan vid Linköpings Universitet
av


Gustav Ahlman

LiTH-ISK-EX--11/4470--SE

Handledare: **Maria Magnusson**
Datorseende, ISY och Radiofysik, IMH, Linköpings Universitet
Olof Dahlqvist Leinhard
Radiofysik, IMH, Linköpings Universitet
Peter Lundberg
Radiofysik, IMH, Linköpings Universitet

Examinator: **Maria Magnusson**
ISK, Linköpings Universitet

Linköping, 8 juni 2011

Presentationsdatum 2011-06-08 Publiceringsdatum (elektronisk version) 2011-09-08	Institution och avdelning Institutionen för systemteknik Department of Electrical Engineering	 Linköpings universitet
---	--	--

URL för elektronisk version

<http://www.ep.liu.se>

Språk Svenska X Engelska Antal sidor 76	Typ av publikation Licentiatavhandling X Examensarbete C-uppsats D-uppsats Rapport Annat (ange nedan)	ISBN (licentiatavhandling) ISRN LiTH-isy-ex--11/4470--SE Serietitel (licentiatavhandling) Serienummer/ISSN (licentiatavhandling)
---	--	--

Publikationens titel

Improved Temporal Resolution Using Parallel Imaging in Radial-Cartesian 3D functional MRI

Författare

Gustav Ahlman

Sammanfattning

MRI (Magnetic Resonance Imaging) är en medicinsk avbildningsmetod som använder magnetfält för att framställa bilder av människokroppen. Detta examensarbete kretsar kring en ny inläsningsmetod för 3D-fMRI (functional Magnetic Resonance Imaging) vid namn PRESTO-CAN som använder ett radiellt mönster för att sampla (k_x, k_z) -planet av k -rummet (frekvensdomänen), och ett kartesiskt samplingsmönster i k_y -riktningen. Det radiella samplingsmönstret möjliggör tätare sampling av k -rummets centrala delar, som innehåller den mest grundläggande frekvensinformationen om det inlästa objektets struktur. Detta leder till att en högre temporal upplösning kan uppnås jämfört med andra metoder eftersom det krävs ett mindre antal totala sampel för att få tillräcklig information om hur objektet har ändrats över tid. Eftersom fMRI framförallt används för att övervaka blodflödet i hjärnan innebär ökad temporal upplösning att vi kan följa snabba ändringar i hjärnaktivitet mer effektivt.

Den temporala upplösningen kan förbättras ytterligare genom att minska scanningstiden, vilket i sin tur kan uppnås genom att tillämpa parallell avbildning. En metod för parallell avbildning är SENSE (SENsitivity Encoding). Scanningstiden minskas genom att minska samplingstätheten, vilket orsakar vikning i de inlästa bilderna. Vikningen tas bort med SENSE-metoden genom att utnyttja den extra information som tillhandahålls av det faktum att ett flertal olika mottagarspolar med sinsemellan olika känsligheter används vid inläsningen. Genom att mäta upp känsligheterna för de respektive mottagarspolarna och lösa ett ekvationssystem med de vikta bilderna är det möjligt att beräkna hur de skulle ha sett ut utan vikning.

I detta examensarbete har SENSE framgångsrikt implementerats i PRESTO-CAN. Genom att använda normaliserad faltning för att förfinas mottagarspolarnas känslighetskartor har bilder med tillfredsställande kvalitet varit möjliga att rekonstruera när samplingstätheten av k -rummet minskats med en faktor 2, och bilder med relativt bra kvalitet också när samplingstätheten minskats med en faktor 4. På detta sätt har detta examensarbete kunnat bidra till förbättrandet av PRESTO-CAN-metodens temporala upplösning.

Nyckelord

fMRI, PRESTO-CAN, SENSE, parallel imaging, temporal resolution, radial-Cartesian sampling, normalized convolution

Abstract

MRI (Magnetic Resonance Imaging) is a medical imaging method that uses magnetic fields in order to retrieve images of the human body. This thesis revolves around a novel acquisition method of 3D fMRI (functional Magnetic Resonance Imaging) called PRESTO-CAN that uses a radial pattern in order to sample the (k_x, k_z) -plane of k -space (the frequency domain), and a Cartesian sample pattern in the k_y -direction. The radial sample pattern allows for a denser sampling of the central parts of k -space, which contain the most basic frequency information about the structure of the recorded object. This allows for higher temporal resolution to be achieved compared with other sampling methods since a fewer amount of total samples are needed in order to retrieve enough information about how the object has changed over time. Since fMRI is mainly used for monitoring blood flow in the brain, increased temporal resolution means that we can be able to track fast changes in brain activity more efficiently.

The temporal resolution can be further improved by reducing the time needed for scanning, which in turn can be achieved by applying parallel imaging. One such parallel imaging method is SENSE (SENSitivity Encoding). The scan time is reduced by decreasing the sampling density, which causes aliasing in the recorded images. The aliasing is removed by the SENSE method by utilizing the extra information provided by the fact that multiple receiver coils with differing sensitivities are used during the acquisition. By measuring the sensitivities of the respective receiver coils and solving an equation system with the aliased images, it is possible to calculate how they would have looked like without aliasing.

In this master thesis, SENSE has been successfully implemented in PRESTO-CAN. By using normalized convolution in order to refine the sensitivity maps of the receiver coils, images with satisfying quality was able to be reconstructed when reducing the k -space sample rate by a factor of 2, and images of relatively good quality also when the sample rate was reduced by a factor of 4. In this way, this thesis has been able to contribute to the improvement of the temporal resolution of the PRESTO-CAN method.

Sammanfattning

MRI (Magnetic Resonance Imaging) är en medicinsk avbildningsmetod som använder magnetfält för att framställa bilder av människokroppen. Detta examensarbete kretsar kring en ny inläsningsmetod för 3D-fMRI (functional Magnetic Resonance Imaging) vid namn PRESTO-CAN som använder ett radiellt mönster för att sampla (k_x, k_z) -planet av k -rummet (frekvensdomänen), och ett kartesiskt samplingsmönster i k_y -riktningen. Det radiella samplingsmönstret möjliggör tätare sampling av k -rummets centrala delar, som innehåller den mest grundläggande frekvensinformationen om det inlästa objektets struktur. Detta leder till att en högre temporal upplösning kan uppnås jämfört med andra metoder eftersom det krävs ett mindre antal totala sampel för att få tillräcklig information om hur objektet har ändrats över tid. Eftersom fMRI framförallt används för att övervaka blodflödet i hjärnan innebär ökad temporal upplösning att vi kan följa snabba ändringar i hjärnaktivitet mer effektivt.

Den temporala upplösningen kan förbättras ytterligare genom att minska scanningstiden, vilket i sin tur kan uppnås genom att tillämpa parallell avbildning. En metod för parallell avbildning är SENSE (SENsitivity Encoding). Scanningstiden minskas genom att minska samplingstätheten, vilket orsakar vikning i de inlästa bilderna. Vikningen tas bort med SENSE-metoden genom att utnyttja den extra information som tillhandahålls av det faktum att ett flertal olika mottagarspolar med sinsemellan olika känsligheter används vid inläsningen. Genom att mäta upp känsligheterna för de respektive mottagarspolarna och lösa ett ekvationssystem med de vikta bilderna är det möjligt att beräkna hur de skulle ha sett ut utan vikning.

I detta examensarbete har SENSE framgångsrikt implementerats i PRESTO-CAN. Genom att använda normaliserad faltning för att förfinas mottagarspolarnas känslighetskartor har bilder med tillfredsställande kvalitet varit möjliga att rekonstruera när samplingstätheten av k -rummet minskats med en faktor 2, och bilder med relativt bra kvalitet också när samplingstätheten minskats med en faktor 4. På detta sätt har detta examensarbete kunnat bidra till förbättrandet av PRESTO-CAN-metodens temporala upplösning.

Acknowledgements

I would like to give a great thanks to my examiner and supervisor Maria Magnusson, who have been incredibly helpful during all stages of the work on this thesis. I would also like to thank my co-supervisors Olof Dahlqvist Leinhard and Peter Lundberg for their additional guidance, ideas and suggestions. Big thanks also to my desk neighbors Anette Karlsson and Anders Tisell for all their valuable inputs and the opportunities of idea exchanges they have given, as well as the cheerful small talks during coffee and lunch breaks.

But most of all, I would like to thank Almighty God for all his abundant blessings, including having made it possible for me to finish this thesis. I dedicate this work to the Blessed Virgin Mary, Our Lady of Mount Carmel; and through her to her divine Son, our Lord and Saviour Jesus Christ.

Contents

Abstract	i
Sammanfattning	ii
Acknowledgements	iii
Contents	v
1 Introduction	1
1.1 Purpose and Goal	1
1.2 Expected Results	2
1.3 Limitations	2
1.4 Method	2
2 Abbreviations	3
3 Theory	4
3.1 Basics of MRI	4
3.1.1 History	4
3.1.2 Spin Physics	4
3.1.3 Spatial Encoding	6
3.1.4 Sampling of k -space	7
3.1.5 fMRI	10
3.1.6 Receiver Coils	10
3.2 PRESTO-CAN	11
3.2.1 Sampling Pattern	11
3.2.2 Determination of Angular Increment	13
3.2.3 Image Reconstruction	14
3.3 Parallel Imaging and SENSE	18
3.3.1 History of Parallel Imaging	18
3.3.2 Unfolding the Image Using SENSE	18
3.3.3 Noise Amplification	22
3.3.4 Determining Sensitivity Maps	22
4 Implementation	27
4.1 2D Implementation of SENSE	27
4.1.1 Simulation of Coils	27
4.1.2 Measuring Coil Sensitivity	29
4.1.3 SENSE Reconstruction	31
4.2 3D implementation of SENSE	32
4.2.1 Simulation of Coils	32
4.2.2 Simulation of Phantom	32

4.2.3	Image Reconstruction.....	32
4.2.4	Sensitivity Map Refinement.....	33
4.2.5	Results.....	33
4.3	3D Implementation of SENSE, Real Data Acquired With PRESTO-CART	35
4.4	3D Implementation of SENSE, Real Data Acquired With PRESTO-CAN	37
4.4.1	Acquisition of Quadrature Image and Surface Coil Images	37
4.4.2	Calculation of Raw Sensitivity Maps.....	38
4.4.3	Refinement of Sensitivity Maps Using Normalized Convolution	41
4.4.4	Acquisition of SENSE Reduced Data	42
4.4.5	SENSE Reconstruction.....	43
4.4.6	Adjustable Parameters.....	43
5	Results.....	46
5.1	Sensitivity Maps	46
5.2	Reconstruction of SENSE Reduction Performed by the MR-Scanner.....	48
5.3	Reconstruction of Manual SENSE Reduction	54
6	Discussion	57
6.1	Future Work.....	59
7	Conclusions.....	59
8	References.....	60
	Appendix A: Sensitivity Maps	63
	Appendix B: Results of SENSE Reconstruction	67

1 Introduction

MRI (Magnetic Resonance Imaging) is a medical imaging method that uses magnetic fields in order to retrieve images of the human body. By placing the subject in a magnetic field and applying electromagnetic pulses of certain frequencies, a signal emitted by the hydrogen nuclei (protons) of the subject can be recorded. This signal is acquired in the frequency domain, or k -space as it is conventionally called in MRI applications. This means that the signal needs to be reconstructed by inverse Fourier transforming in order to retrieve an image of the subject. A special type of MRI is fMRI (functional Magnetic Resonance Imaging), which produces sequences of low-resolution images where it is possible to track changes in the recorded tissue of the subject over time. The main application of this method is to track the blood flow of the brain in order to visualize brain activity. In order to be able to track quick and subtle changes, it is preferable that the temporal resolution of the images is as high as possible. However, this must of course not come to the cost of reduced image quality.

At the Center for Medical Image Science and Visualization (CMIV) at Linköping University and the Department of Radiation Physics at the University Hospital of Linköping, a novel acquisition method of fMRI called PRESTO-CAN has been developed [1], [2], [3], [4]. Conventional methods of retrieving MR images typically use Cartesian sampling patterns when sampling the signal in k -space, which can be directly reconstructed to the image domain using the inverse Fast Fourier Transform (FFT) algorithm. PRESTO-CAN samples k -space in 3D, using a Cartesian sampling pattern in the ky -direction but a radial sampling pattern in the (kx, kz) -plane. The main advantage of radial sampling is that the center of k -space, with the low frequency components containing the most important information about the image, is sampled denser than the outer parts. This allows for higher temporal resolution to be achieved compared with other sampling methods since a fewer amount of total samples are needed in order to retrieve enough information about how the object has changed over time. Thus, the method has potential of providing images with better temporal resolution than previous methods with maintained image quality, but it needs to be further developed before this can be fully proven.

One way of improving the method is to implement parallel imaging. With parallel imaging, it is possible to sample k -space less dense, allowing for a faster scanning time and higher temporal resolution, without loss of image quality. One such parallel imaging method is SENSE (SENSitivity Encoding) [5]. SENSE works by making use of the fact that the MR-scanner uses multiple receiver coils in order to record the signal from k -space, all with different sensitivities. This provides the extra information lost by the sparse sampling of k -space, and allows for increased temporal resolution with maintained image quality.

1.1 Purpose and Goal

This master thesis is based on and will continue to build on the previous work done on the PRESTO-CAN project [1], [2], [3], [4], [6], [7]. The aim is to improve the temporal resolution of 3D fMRI reconstructed with the PRESTO-CAN method by implementing parallel imaging according to the SENSE method. Since PRESTO-CAN works in 3D, the SENSE implementation also has to be done in 3D, even if SENSE itself only will be utilized in one dimension, namely the Cartesian sampled ky -direction. Using SENSE with Cartesian sampled 3D fMRI has been tried out in [8], and this thesis aims to move the work one step forward by solving the problems that might arise from the move from 2D to 3D, as well as from the interaction with the radial

sampling of the (k_x, k_z) -plane. The successful implementation of SENSE would be one step in improving PRESTO-CAN in order for it to become more efficient than conventional reconstruction methods. The result will be evaluated in order to investigate the relationships between time acceleration, signal-to-noise ratio and image quality, and to determine to what extent the temporal resolution can be increased with enough image quality maintained.

1.2 Expected Results

The main expected result of this master thesis is a Matlab script that makes it possible to use the PRESTO-CAN reconstruction method of fMRI with reduced scanning time and maintained image quality, using the SENSE method. The *reduction rate*, R , is defined as the ratio between the number of rows in the output image and the number of k -space rows sampled. According to [9], a reduction rate of at least between $N/2$ and $N/3$, N being the number of receiver coils, should be able to be obtained without loss of image quality. With parallel imaging such as SENSE, the reduction rate can theoretically be increased up to N , but increasing the reduction rate will always also decrease the SNR (signal-to-noise ratio). In this master thesis work, an MR-scanner with 8 receiver coils will be used, so in theory we should be able to get a reduction rate of 8, but it is likely that the highest possible rate with an acceptable noise level is much lower. As stated in [9], the minimum reduction rate should however at least be somewhere between $8/2 = 4$ and around $8/3 \approx 2.66$. Since even higher temporal resolution is expected to be achieved at the price of some decrease in SNR, a thorough description of the relationships between reduction rate, increase of temporal resolution, signal-to-noise ratio and image quality in order for the user to be able to decide a well-balanced trade-off, is also expected as a result of the master thesis. Specific numerical values of these are, however, hard to predict before the method has been implemented.

1.3 Limitations

Even though one of the main uses of fMRI is to see how brain activity changes over time, for which a 4D volume is needed (3 spatial dimensions + time) this implementation will concentrate on analyzing still 3D volumes and apply SENSE to these. If this is successful, it should be quite elementary to also apply it to 4D data sets. Limiting ourselves to work with 3 dimensions will, however, also limit the conclusions that can be drawn about the increase of temporal resolution. Since we won't have unlimited access to an MR-scanner either, it probably won't be possible to thoroughly investigate all different settings that can be chosen when recording images, and for the real data we will therefore have to limit ourselves to for example only using SENSE reduction factors of 2 and 4. Results with other reduction factors should, however, be able to be retrieved by simulation.

1.4 Method

Relevant literature, both books and journal articles, will be studied in order to find out the different methods of applying SENSE to Cartesian sampled MR. Matlab scripts earlier developed in this project that reconstructs images sampled with PRESTO-CAN will then be studied and expanded to include parallel imaging according to the SENSE method. At first, simulations completely performed in Matlab will be done. Real data will then be recorded using a Philips Achieva 1.5 T MR-scanner and read into Matlab.

2 Abbreviations

The following abbreviations will be used throughout this thesis.

B_0 – Static magnetic field

B_1 – Rotating magnetic field corresponding to the RF-pulse

BOLD – Blood-oxygen-level dependent

EPI – Echo Planar Imaging

fMRI – functional Magnetic Resonance Imaging

FOV – Field of View

G_x – Gradient in the x-direction

G_y – Gradient in the y-direction

G_z – Gradient in the z-direction

in vitro – In phantoms (i.e. bottles)

in vivo – In a living human

k -space – An alternative designation of the Fourier (frequency) domain, used in MR applications

MRI – Magnetic Resonance Imaging

PRESTO – Principles of Echo-Shifting with a Train of Observations

PRESTO-CAN – The radial-Cartesian fMRI acquisition method used in this thesis

RF-pulse – Radio Frequency pulse

SENSE – SENSitivity Encoding

SNR – Signal to Noise Ratio

3 Theory

3.1 Basics of MRI

For readers who have no background knowledge of MRI, following is a brief description of what it is and how it works. It is, however, beyond the scope of this thesis to give a thorough explanation of the physics and mathematics behind MRI. The interested reader is therefore directed to an MRI text book such as [10] or Internet sources such as [11] or [12], on which the information of this section is based.

3.1.1 History

The magnetic resonance phenomenon was discovered independently by Felix Bloch and Edward Purcell in 1946, and they were both rewarded with the Nobel Prize in 1952. The technique was at first called Nuclear Magnetic Resonance (NMR), but the word nuclear was dropped in the 1970's because of its negative associations. The first MR image was published in 1973 and clinical use of was started in 1984 by Philips. In 1992, fMRI was developed, which made it possible to visualize brain activity and map which parts of the brain that corresponds to different functions. In 2003, Paul Lauterbur and Peter Mansfield were awarded with the Nobel Prize for their discoveries in the MRI field, primarily regarding the use of gradients to determine spatial localization.



Figure 1. The Philips Achieva 1.5 Tesla MR scanner used in this thesis. The coordinate system of the MR-scanner has been marked. (Image source: [13])

3.1.2 Spin Physics

At the basis of magnetic resonance stands the fundamental property of elemental particles called spin. Spin can both be positive and negative, and it is possible for the net spin of a molecule to cancel out if it consists of two or more particles with opposite spin signs. Particles that do have a

net spin can absorb energy of frequency ω , called the *Larmor* frequency, when placed in a magnetic field B_0 along the z-axis of the MR-scanner (see Figure 1) according to the formula

$$\omega = \gamma B_0, \quad (1)$$

where γ is the gyromagnetic ratio, specific for all particles. For hydrogen, the particle most commonly studied in MRI, $\gamma = 42.58$ MHz/T. When placed in a magnetic field B_0 , particles with net spin will align with the direction of the field, either parallel to the magnetic field (corresponding to a low-energy state), or anti-parallel to it (high-energy state). There will be a small excess of particles in the low energy state, where the ratio between the number of high-energy state particles n_+ and low-energy particles n_- is determined by

$$\frac{n_+}{n_-} = e^{\frac{-\Delta E}{kT}}, \quad (2)$$

where ΔE is the energy difference between the two energy states, k is Boltzmann's constant $1.3805 \cdot 10^{-23}$ J/K and T is the temperature in Kelvin. At room temperature, this ratio is around 1.000007, which differs just enough from 1 in order to give rise to a net magnetization vector \mathbf{M} along B_0 . How this is further utilized in order to retrieve images can be thoroughly described using quantum mechanics, but here we will limit ourselves to the simplified, classical description. In an MR-scanner, the direction of the B_0 field corresponds to the z-axis of the MR-scanner's coordinate system. By applying an RF-pulse with the Larmor frequency ω perpendicular to the B_0 field, a magnetic field B_1 is generated, which causes \mathbf{M} to flip down to the xy-plane while precessing around the z-axis with the Larmor frequency (see Figure 2). Note that the flip angle of \mathbf{M} does not necessarily need to be 90° as indicated in Figure 2. In the PRESTO-CAN acquisition method regarded in this thesis, the flip angle is around 10° - 15° .

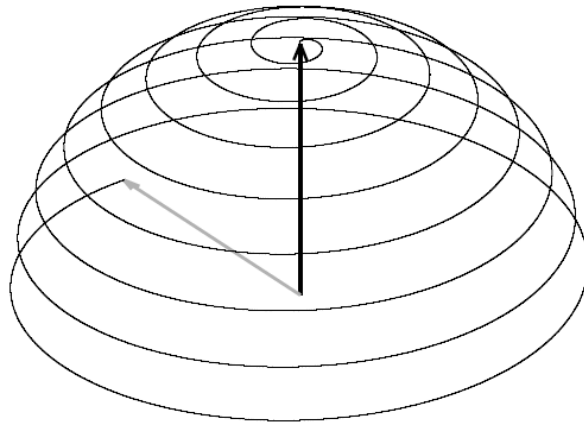


Figure 2. The magnetization vector \mathbf{M} starts to precess around B_0 and is flipped down to the xy-plane when the rotating magnetic field B_1 is applied. (Image source: [14])

When B_1 is turned off, \mathbf{M} will gradually return to its original state. The magnetization in the z-direction, M_z , will thus vary according to

$$M_z(t) = M_z(0)(1 - e^{-\frac{t}{T_1}}). \quad (3)$$

The time constant T_1 is called the *spin lattice relaxation time*, and is defined by when the magnitude of M_z has returned to $(1 - e^{-1}) \approx 63\%$ of its original value. As soon as the B_1 field is turned off, the \mathbf{M} vector will start to decrease in magnitude because of dephasing of the spin

packages making up the vector. This comes from the fact that the different spin packages experience different magnetic field strengths, which makes their respective Larmor frequencies vary slightly. The net magnetization in the xy -plane, M_{xy} , will therefore slowly decrease from its original value M_{xy} with time according to

$$M_{xy}(t) = M_{xy}(0)e^{-\frac{t}{T_2}}. \quad (4)$$

The time constant T_2 is called the *spin-spin relaxation time*, and is defined by when the magnitude of M_{xy} has decreased to $e^{-1} \approx 37\%$ of its original value. The T_1 and T_2 processes occur simultaneously, and T_2 is always equal or less than T_1 . While T_2 is defined as only depending on the dephasing of the spin packages, M_{xy} will decrease additionally because of inhomogeneities in the B_0 field. The time constant that results from both these factors is denoted as T_2^* .

3.1.3 Spatial Encoding

The magnetization vector \mathbf{M} induces currents in the receiver coils of the MR-scanner, and the signal can thus be measured (see Figure 3). By analyzing the signal received by the coils, it is possible to determine the values of T_1 , T_2 and T_2^* . Since these in turn depend on the concentration of hydrogen of the various different tissues of the object in the MR-scanner, as well as how strongly the hydrogen is bound to other particles, it is possible to differentiate the various tissue types from each other. By varying the magnetic field locally, it is also possible to get information from different spatial positions of the volume. In 2D MRI, the strength of B_0 varies linearly somewhat in the z -direction, and consequently also the Larmor frequency. By changing the frequency of the RF-pulse, it is therefore possible to excite only a slice of the object in the z -direction. During 3D acquisition, as is the case with PRESTO-CAN, a slab-selection gradient is used in order to excite a whole 3D volume at a time, and a phase-encoding gradient is used to navigate through the third direction [15].

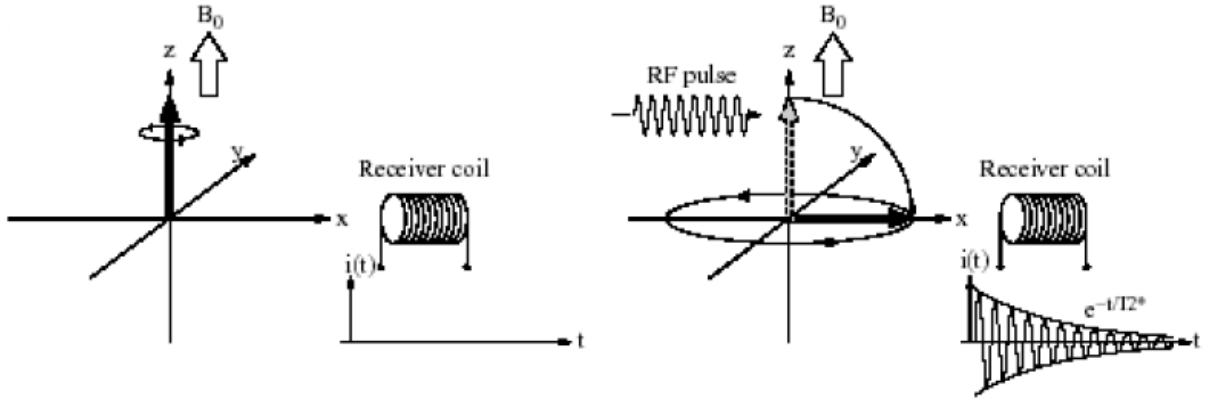


Figure 3. The magnetization vector \mathbf{M} is flipped down to the xy -plane when an RF-pulse corresponding to the magnetic field B_1 is applied, thus inducing a current $i(t)$ into the receiver coil(s). Due to the different kinds of relaxation processes, the current will decay, and from this it is possible to measure the T_1 , T_2 and T_2^* values. (Image source: [16])

Further spatial encoding is done by adding gradient fields, $G(\mathbf{x})$, $\mathbf{x} = (x, y, z)^T$, that make the magnetic field vary spatially. The local magnetization, m , becomes

$$m(\mathbf{x}, t) = m_0 e^{-j\omega t}, \quad (5)$$

where $\omega = \omega_0 + \gamma G(\mathbf{x})$ such that

$$m(\mathbf{x}, t) = m_0 e^{-j(\omega_0 + \gamma G(\mathbf{x}))t}. \quad (6)$$

The signal $S(t)$ measured by the receiver coil is the integral of (6) over the whole excited object Ω , after demodulation of the spatially constant term $\omega_0 t$, according to

$$S(t) = \int_{\Omega} m_0 e^{-j\gamma G(\mathbf{x})t} dt. \quad (7)$$

In other words, the receiver coil is measuring the Fourier transform of the signal emitted from the object, the definition of the Fourier transform being

$$\mathcal{F}\{f(t)\} = \int_{-\infty}^{\infty} f(t) e^{-j\omega t} dt. \quad (8)$$

From this follows that by varying the local magnetic field gradients $G(\mathbf{x})$, it is possible to navigate in k -space (the Fourier domain) and retrieve the Fourier transform of the magnetization signal $m(\mathbf{x})$ from different spatial positions. If we separate $G(\mathbf{x})$ into G_x , G_y and G_z , the Fourier transform of $m(\mathbf{x})$ can be written as

$$\mathcal{F}\{m(\mathbf{x})\} = \int_{-\infty}^{\infty} m(\mathbf{x}) e^{-j \int_0^t \gamma (G_x(\tau)x + G_y(\tau)y + G_z(\tau)z) d\tau} d\mathbf{x}. \quad (9)$$

The multi-dimensional Fourier transform of $m(\mathbf{x})$ is usually written as

$$\mathcal{F}\{m(\mathbf{x})\} = \int_{-\infty}^{\infty} m(\mathbf{x}) e^{-j\mathbf{x}^T \mathbf{u} t} d\mathbf{x}, \quad (10)$$

where $\mathbf{u} = (u, v, w)^T$ and the positions of the sample in k -space at the time point t , $u(t)$, $v(t)$ and $w(t)$, are given by

$$u(t) = \gamma \int_0^t G_x(\tau) d\tau, \quad v(t) = \gamma \int_0^t G_y(\tau) d\tau, \quad w(t) = \gamma \int_0^t G_z(\tau) d\tau. \quad (11)$$

3.1.4 Sampling of k -space

After the excitation of a slice (2D) or slab (3D) of the object as explained in Section 3.1.3, k -space is navigated by changing the G_x , G_y and (in 3D) G_z gradients. The best possible image quality is acquired if only one row is recorded for every excitation, but since after each excitation you have to wait until the magnetization vector \mathbf{M} has returned to its original position until another excitation can be done, this means that scanning of the whole object will take a very long time. A faster way to retrieve images is therefore to sample multiple rows of k -space in the same excitation. A method that does this is Echo Planar Imaging (EPI).

3.1.4.1 Multishot

Figure 4 shows how k -space is navigated during an MR scan that uses EPI. In Figure 4 (a), a whole slice of k -space is scanned in one single excitation. Since the strength of the signal will decay during the scan, this will give quite low image quality. In order to avoid this, the scanning can be divided into multiple excitations as is done in Figure 4 (b), a method called multishot. Using multishot will, however, make the scanning take longer time. The number of rows that are sampled every excitation is referred to as the EPI-factor. Using multishot with different EPI-factors can thus be utilized in order to change priority between image quality and acquisition speed.

3.1.4.2 Pulse Sequences

Figure 5 shows how the gradient fields and RF pulses are applied in order to produce a 2D EPI sequence, and Figure 6 shows the corresponding sequence for 3D EPI.

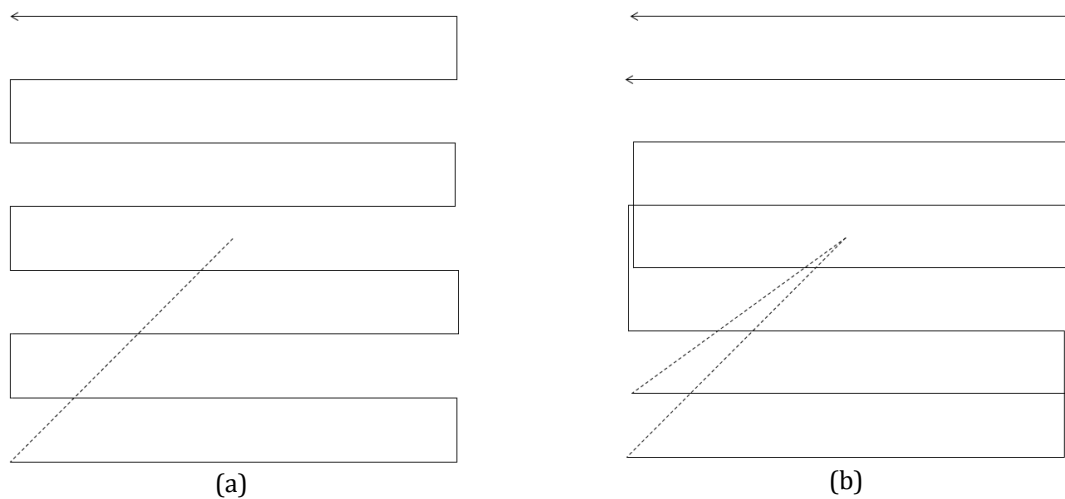


Figure 4. Schematic depiction of how 8 rows of k -space is sampled using EPI with (a) singleshot, EPI-factor 8, (b) multishot = 2, EPI-factor 4.

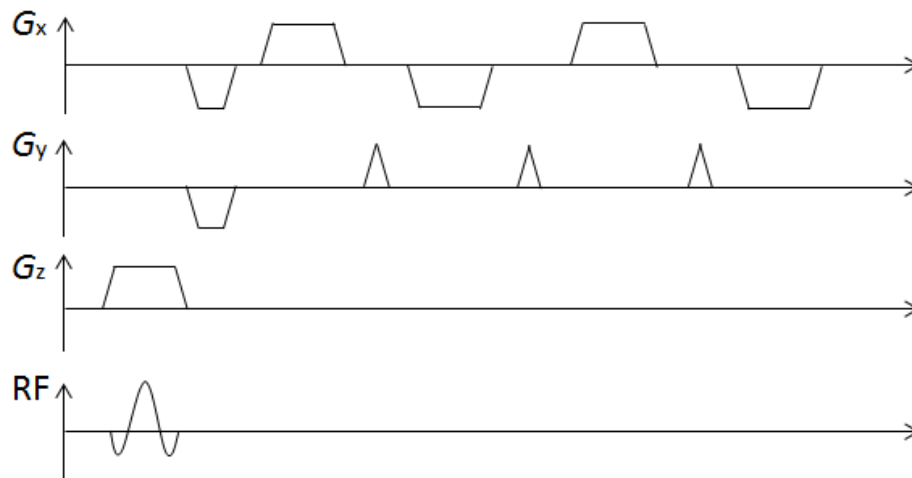


Figure 5. Graph of the pulse sequence showing how the different gradients and the RF pulse are used during a 2D EPI sequence that scans 4 rows of k -space.

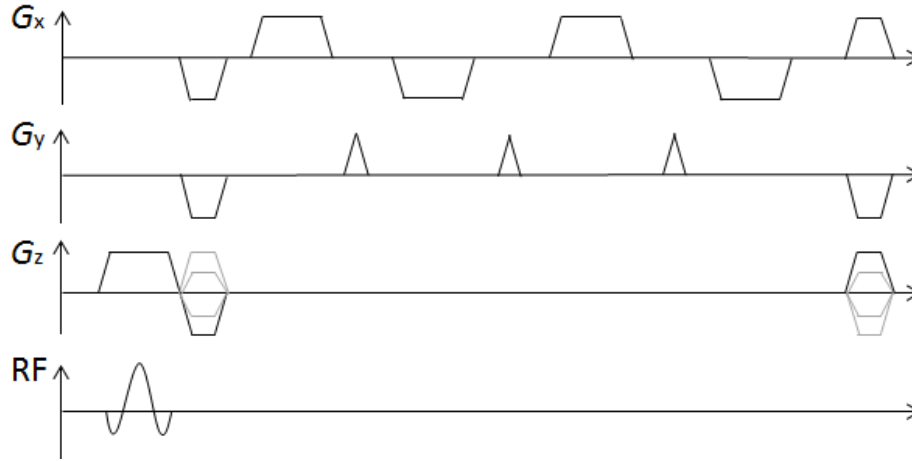


Figure 6. Graph of the pulse sequence showing how the different gradients and the RF pulse are used during a 3D EPI sequence that scans 4 rows of k -space at different slices in the z direction.

In the 2D sequence, the positive and negative lobes of the G_x gradient correspond to moving to the right and left in the x -direction, and the small blips of the G_y gradient correspond to moving to the next row in the y -direction. The G_x and G_y gradients are also used to produce prephasing lobes that are applied before the actual scanning starts in order to begin the scanning in the down-left corner. In order to move back to the center after each profile has been scanned, similar lobes are added at the end of the sequence. During 3D acquisition, the sign and magnitude of the G_z gradient is also changed between each profile in order to navigate between different slices in the z -direction. This is in turn compensated by a dephasing lobe with the opposite sign after acquisition of each profile in order to balance the sequence [6].

3.1.4.3 Inverse Fourier Transformation

In order to acquire a spatial image of the object in the MR-scanner, the signal measured by the receiver coil has to be inversely Fourier transformed, usually by means of the inverse Fast Fourier Transform algorithm (IFFT). The resulting image will have the same resolution, but its properties will differ depending on how densely k -space is sampled. In this case, the inverse sampling theorem holds:

$$\Delta k_x \leq \frac{1}{FOV_x}, \Delta k_y \leq \frac{1}{FOV_y}, \Delta k_z \leq \frac{1}{FOV_z}, \quad (12)$$

where Δk_x , Δk_y and Δk_z are the distances between samples in the k_x , k_y and k_z directions, and FOV_x , FOV_y and FOV_z are the field of views of the image in the x , y and z directions, respectively. In other words, a longer distance between the samples in k -space leads to a smaller field of view. If the object in the MR-scanner is larger than the field of view, spatial aliasing will occur, which leads to a folded image. This fact is central to the SENSE method that we will implement in this thesis. Spatial aliasing is avoided by keeping the sampling distance small enough to make the FOV larger than the object in each direction according to (12). The resolution of the resulting image can on the other hand be increased by increasing the number of samples by sampling further out in k -space. How different manners of sampling k -space affect the resulting spatial image is visualized in Figure 7.

3.1.5 fMRI

Functional Magnetic Resonance Imaging (fMRI) is a modality of MRI that makes it possible to measure brain activity. When a certain part of the brain is activated, the level of oxygenated blood increases. This also leads to an increased T_2^* relaxation, which can thus be measured and visualized by the MR-scanner. The measured signal is said to be Blood-oxygen-level dependent (BOLD). The first fMRI images were published in 1992 by Seiji Ogawa. By making use of EPI and keeping the image resolution low in order to be able to reduce the scan time and increase the temporal resolution, it is possible to track changes of the brain activity in real time. By also adding a third dimension, scanning full 3D volumes of the brain, we get one step closer to the method used in this thesis.

3.1.6 Receiver Coils

In the MR-scanner, there are two types of receiver coils. When scanning whole body images, a so-called *body coil* is used, which results in an image with almost homogenous intensity and SNR. When scanning a smaller part of the body, usually *surface coils* are used, which are placed directly on the object. In fMRI where only the head is scanned, an array of surface coils placed in a “helmet” around the object is used (see Figure 8). Since the different coils are placed at different parts of the object, the intensity of the received signal will vary between each coil. This fact is utilized in parallel imaging, explained in section 0. The separate signals from the different surface coils can also be combined by the MR-scanner into an image with homogenous intensity using a quadrature method, and the resulting image is therefore referred to in this thesis as a “*quadrature image*”.

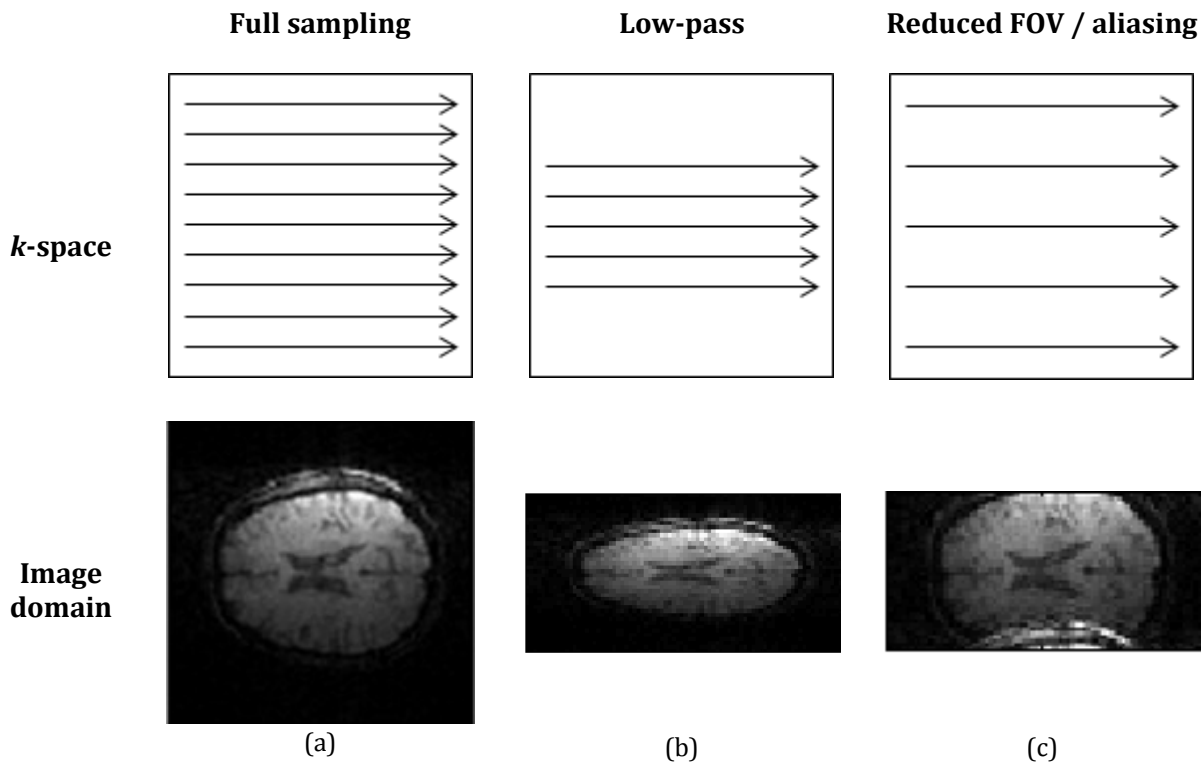


Figure 7. Visualization of the relationship between the sampling of k -space and the resulting image. The arrows depicts which rows of k -space are sampled. In (a), the image is fully sampled. In (b), the number of samples is reduced by half while the sample distance is the same as in (a), which gives an image with the same FOV but twice as low resolution. In (c), the number of samples is reduced by half by removing every second sample, making the sampling distance twice as long, which results in a reduced FOV and an aliased image.

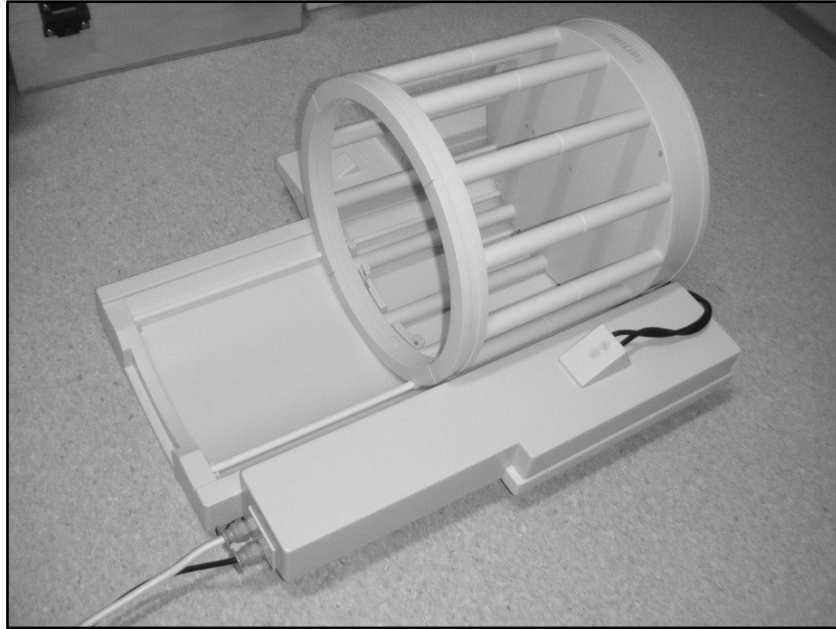


Figure 8. Example of a helmet shaped receiver containing an array of surface receiver coils.

3.2 PRESTO-CAN

PRESTO-CAN is a 3D fMRI acquisition method that samples k -space using a radial sampling pattern, developed at CMIV (Center for Medical Image Science and Visualization) and the Division of Radiation Physics at Linköping University. It is based on the PRESTO method for sampling 2D planes in fMRI, which combines the Priniples of Echo-Shifting with a Train of Observations [17].

3.2.1 Sampling Pattern

In conventional, fully Cartesian 3D fMRI, profiles (slices) parallel to the (k_x, k_y) -plane are sampled one at a time, and new sample profiles are lined up in the k_z -direction. In PRESTO-CAN, the individual 2D profiles are still sampled with an ordinary EPI/PRESTO Cartesian sample pattern in the k_y -direction, but the way the profiles are sampled in the (k_x, k_z) -plane is determined by a radial sampling pattern. Figure 9 shows the PRESTO-CAN pulse sequence for four different angular profiles. The main difference compared to Cartesian 2D and 3D EPI is that the G_x and G_z gradients are applied simultaneously when recording diagonal profiles. A comparison between a 3D EPI Cartesian sampling pattern and PRESTO-CAN can be seen in Figure 10.

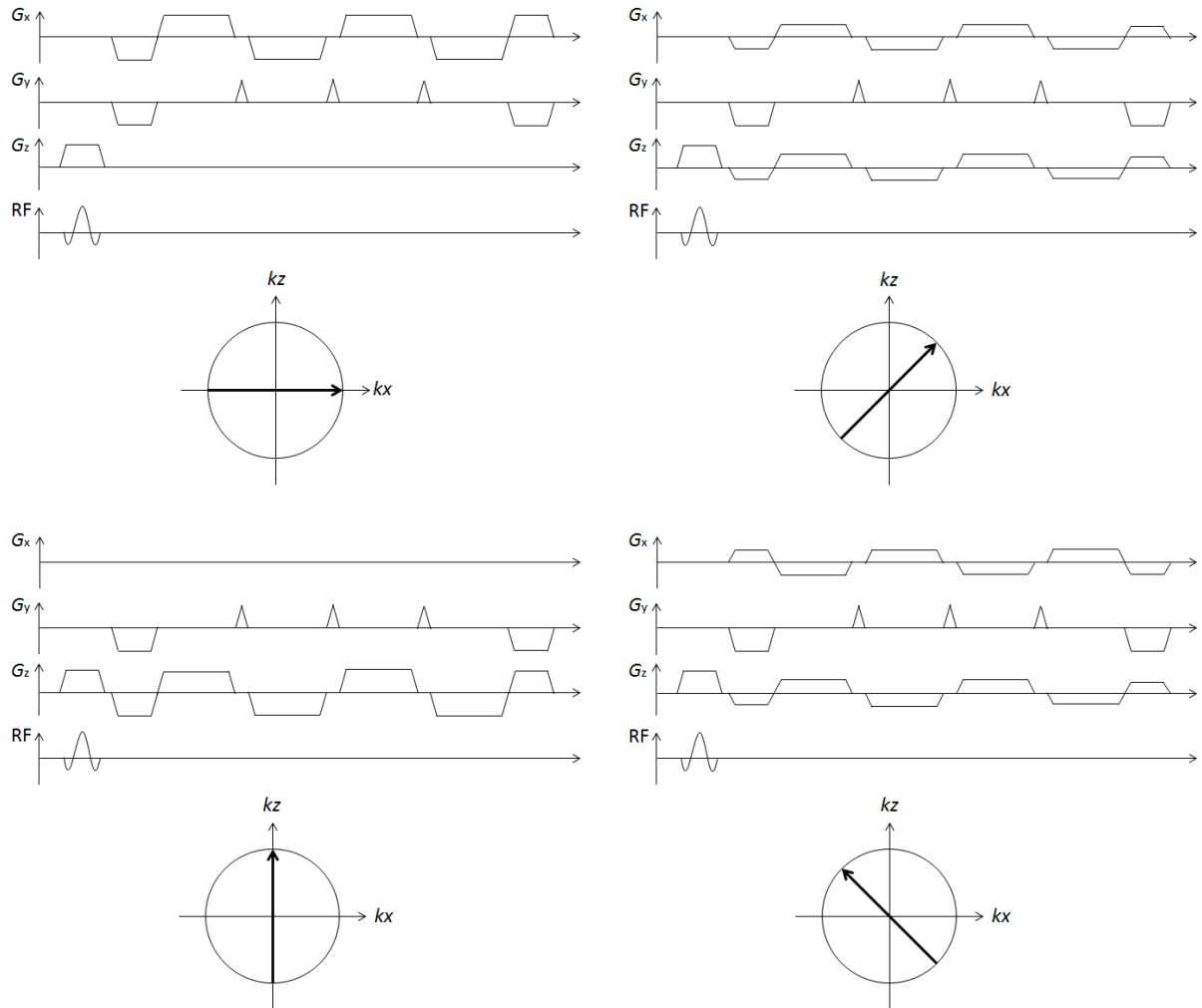


Figure 9. Graphs showing the PRESTO-CAN pulse sequence for four different angular profiles in the (kx, kz) -plane, with corresponding graphs showing how k -space is recorded in each case. (Image idea from [6]).

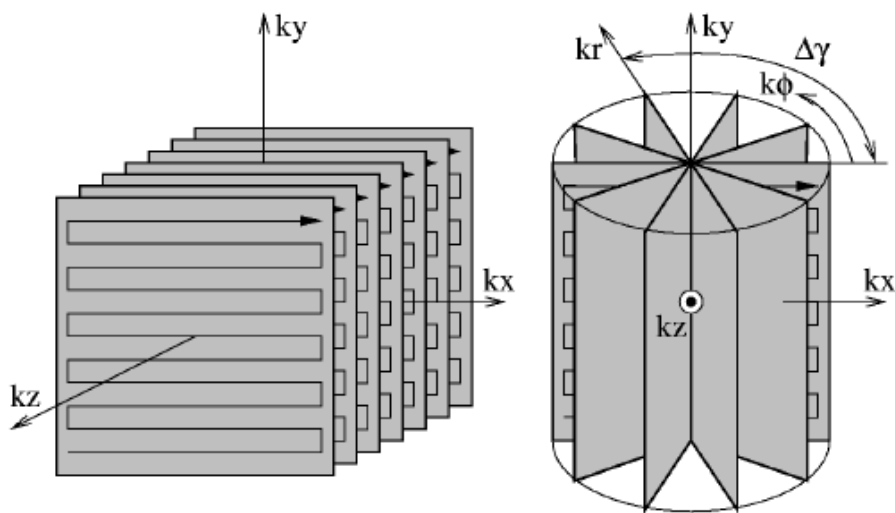


Figure 10. Left: Cartesian sampling. Right: Radial sampling according to PRESTO-CAN. (Image source: [1]).

As stated in the introduction in Section 1, the advantage of PRESTO-CAN is that the central parts of k -space, containing the low-frequency components of the image constituting the most basic information of the structure of the object in the MR-scanner, are sampled more densely than the outer parts. This means that fewer profiles are needed in order to produce a 3D volume that gives at least a rough image of the object, providing with enough information in order to be able to know how it has changed over time. Since not all profiles are updated at the same time but continuously replaced by new ones, this allows for higher temporal resolution to be achieved compared with other sampling methods, which in terms of clinical applications means that changes in brain activity can be discovered faster.

3.2.2 Determination of Angular Increment

Another principle used is that the angular increment between the radial profiles $\Delta\gamma_{orig}$ is determined by dividing 180° with the so-called “golden ratio” according to

$$\Delta\gamma_{orig} = 180^\circ \frac{2}{\sqrt{5} + 1} \approx 111^\circ. \quad (13)$$

This ensures that the most recently sampled profiles will be optimally evenly spread across k -space. In order to also make sure that the same angle is not sampled twice before going through all the number of profiles used to produce an image volume, the number of profiles is set to be a prime number. The angular increment is thus adjusted to

$$\Delta\gamma = 360^\circ \frac{M}{N}, \quad (14)$$

where N is the number of profiles and the integer M chosen such that $\Delta\gamma$ is as close to $\Delta\gamma_{orig}$ as possible. The sample distance at distance r from the origin, $r\pi/N$, should not be larger than $\Delta = \frac{1}{FOV_x}$ in order to avoid under-sampling, which leads to a minimum number of profiles N depending on the radial size of the object. It turns out, however, that some under-sampling in the radial direction can be accepted since it does not affect the resulting image quality significantly. Also, since the central parts of k -space would become too densely sampled if we would keep all the samples from every profile, the central parts of some of the angles do not need to be sampled. If these parts are skipped, the temporal resolution is increased, and when plotted against time, the profiles form an hourglass-shape. Figure 11 shows how the profiles are sampled in the (kx, kz) -plane and Figure 12 shows them plotted against time.

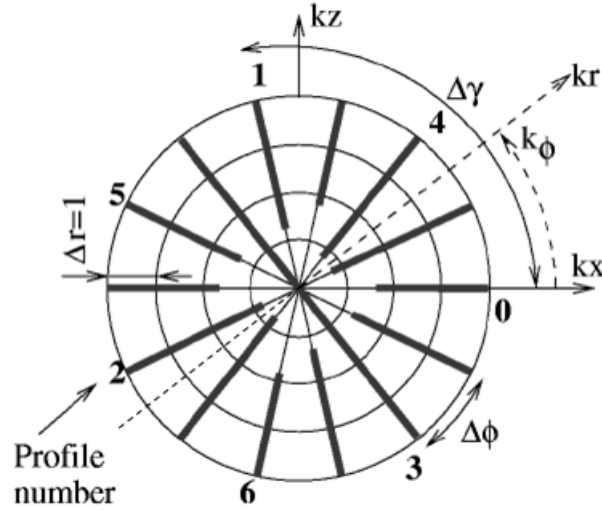


Figure 11. The PRESTO-CAN k -space sampling pattern in the (kx, kz) -plane. (Image source: [1]).

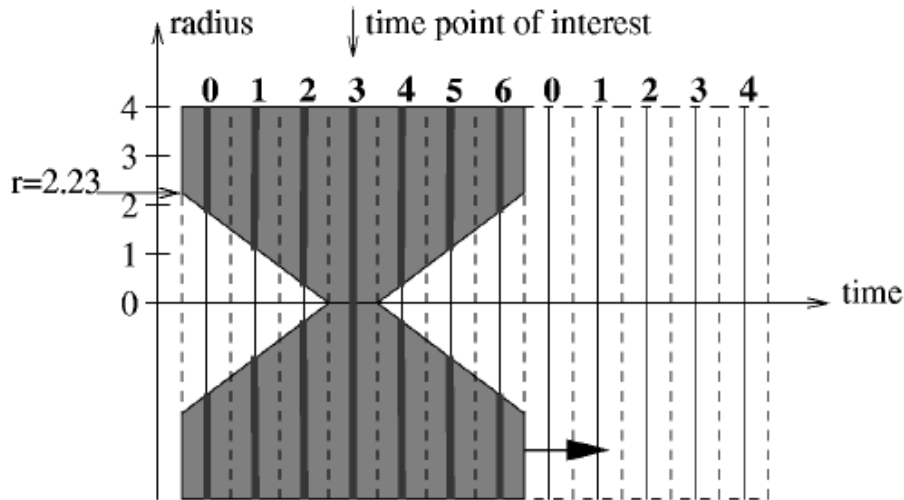


Figure 12. The profiles in the (kx, kz) -plane plotted against time, revealing the shape of the hourglass-filter. (Image source: [1]).

3.2.3 Image Reconstruction

The angular profiles are sampled using the order determined by the golden ratio, and when sorted in this order they are referred to as “golden angles”. The kr -direction is oversampled by a factor of 2 since this does not cost any extra time. In order to compensate for this, the angular profiles are low-pass filtered in the kr -direction. Some data corrections are also performed, namely forward-and-back correction, correction of the rotation-angle position and phase-drift correction.

3.2.3.1 Forward-and-back correction

Forward-and-back correction, also needed for ordinary Cartesian sampled PRESTO, is performed in order to compensate for the small changes in the position of the sampled points based on whether the sampling is performed from left to right or from right to left during EPI acquisition. This is done by first transforming the data to the spatial domain using one-

dimensional inverse Fast Fourier Transformation in the sample direction, followed by multiplication with $\exp(-j2\pi\varphi)$, which corresponds to a translation in k -space. The phase correction vector φ represents the position shifts of all the sample points, and is measured at an earlier reference scan by comparing rows sampled in the opposite direction with each other. The data is finally transformed back to k -space using Fast Fourier Transformation.

3.2.3.2 Correction of the Rotation-Angle Position

When we sample the different profiles in k -space, ideally the origin should be located at the central pixel, which is a prerequisite for the gridding during the PRESTO-CAN reconstruction to work properly. However, it is not guaranteed that there will even be a sample at the exact position of the origin. In order to find out the position of the origin, we compare each $k\varphi$ -profile with its corresponding $k\varphi+180^\circ$ profile. To calculate the profiles for the missing angles which have not been sampled, interpolation is used. If we compare the $(k\varphi, k\varphi+180^\circ)$ profiles with each other using complex correlation and making use of the fact that the value in the origin should be the same in all of them, we are able to obtain the rotation-angle position for every profile. In the implementation, a line is adjusted to this result in order to use the same rotation-angle position for all profiles. This is an approximation that works well, since the correction done is relatively small anyways. In the implementation of this thesis, 0.25 was used.

3.2.3.3 Phase-Drift Correction

Since the object that is recorded in the MR-scanner is a real, physical object, the resulting image after inverse Fourier transformation theoretically should be purely real. This is, however, not the case. Because of different kinds of disturbances in the MR-scanner, we get as a result complex images where the phase varies spatially over the whole image. On top of this, the phase also varies somewhat over time for the same spatial points in the image. This is referred to as phase-drift. After having corrected the rotation-angle-position according to the previous section, the central pixel of each profile should represent the origin. With a diametrical resolution of 160 pixels, this corresponds to $kr = 81$. However, when looking at the phase image of all the profiles, it shows up that in the general case the phase varies in the whole phase range of $[-\pi, \pi]$ between different profiles for $kr = 81$. Since this point is sampled in each profile, and we know that it should be constant if there had been no phase-drift, it is possible to calculate the phase-drift and to correct the values of the different profiles to compensate for this.

3.2.3.4 Cartesian Interpolation and Inverse Fourier Transformation

The results after the previously described steps, showing one slice at constant ky , is presented in Figure 13. The profiles are then sorted and put in the correct order (i.e. 0-360°, see Figure 14). This is followed by resampling to a Cartesian pattern using the gridding method originally presented in [18] and further developed in [19], which has been expanded to three dimensions and involves interpolation with a 4x4-point Kaiser-Bessel filter. The result can be seen in Figure 15. The resampling to a Cartesian pattern is needed in order to be able to perform inverse Fourier transforming using the Fast Fourier Transform algorithm. Before this, however, some post-compensation using a weight function is applied. Then, the data is transformed to the spatial (image) domain using 3D inverse Fourier transformation. In order to correct the intensity, division by the inverse Fourier transform of the Kaiser-Bessel filter applied earlier in the process is performed, followed by cropping. The result is shown in Figure 16 and Figure 17.

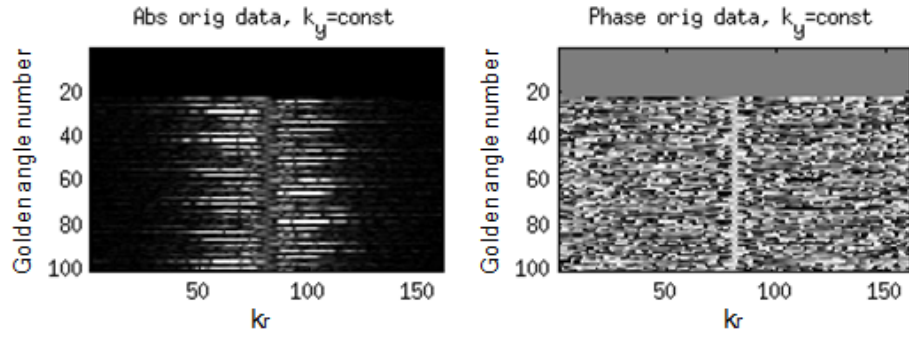


Figure 13. Magnitude and phase for angular profiles at constant k_y sampled with PRESTO-CAN and low pass filtered. The uppermost rows are empty due to programming technical reasons.

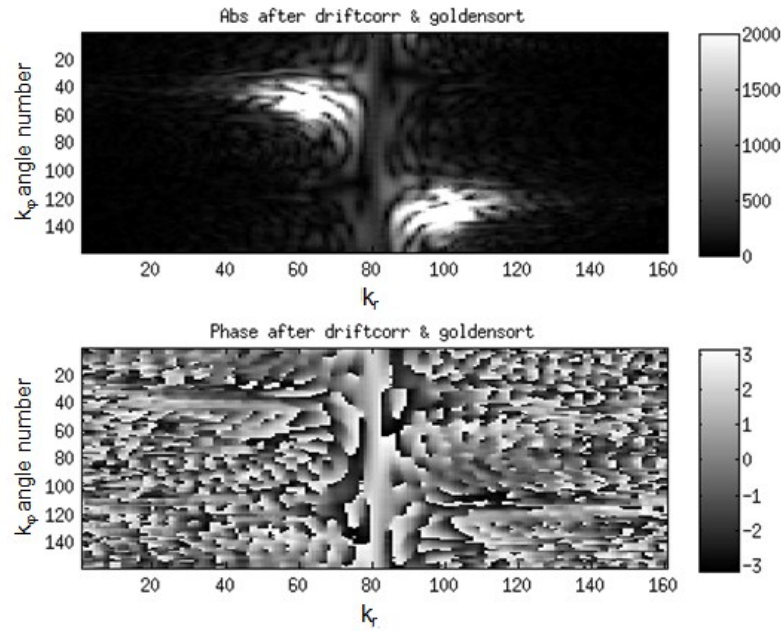


Figure 14. Magnitude and phase for constant k_y of angular profiles sampled with PRESTO-CAN after sorting to the correct order (0-360°).

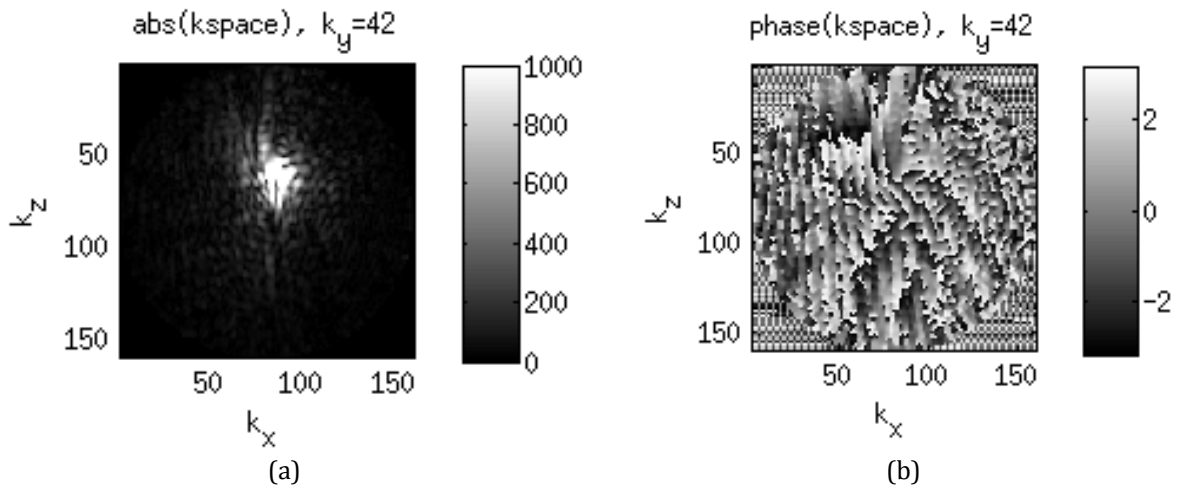


Figure 15. (a) Magnitude and (b) phase for constant k_y of PRESTO-CAN data after resampling to a Cartesian pattern.

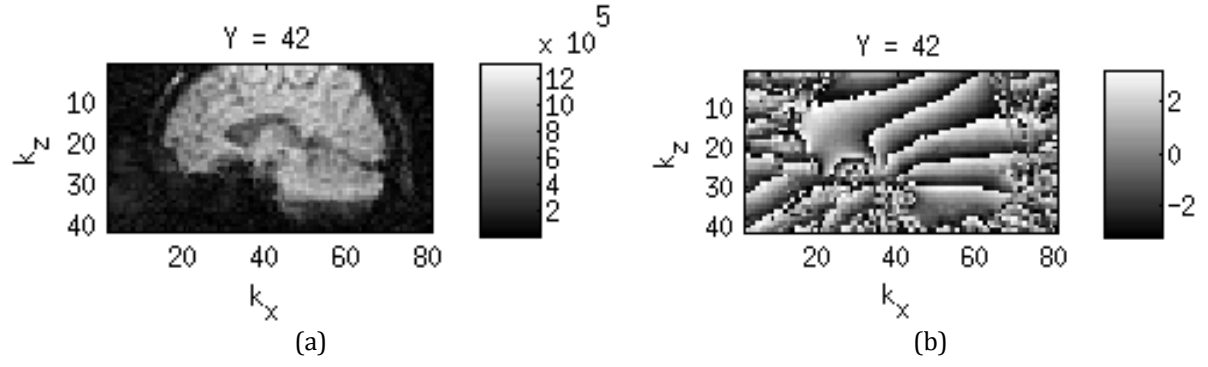


Figure 16. (a) Magnitude and (b) phase of one slice in the (k_x, k_z) -plane data acquired with the PRESTO-CAN method after inverse Fourier transformation to the spatial domain and cropping.

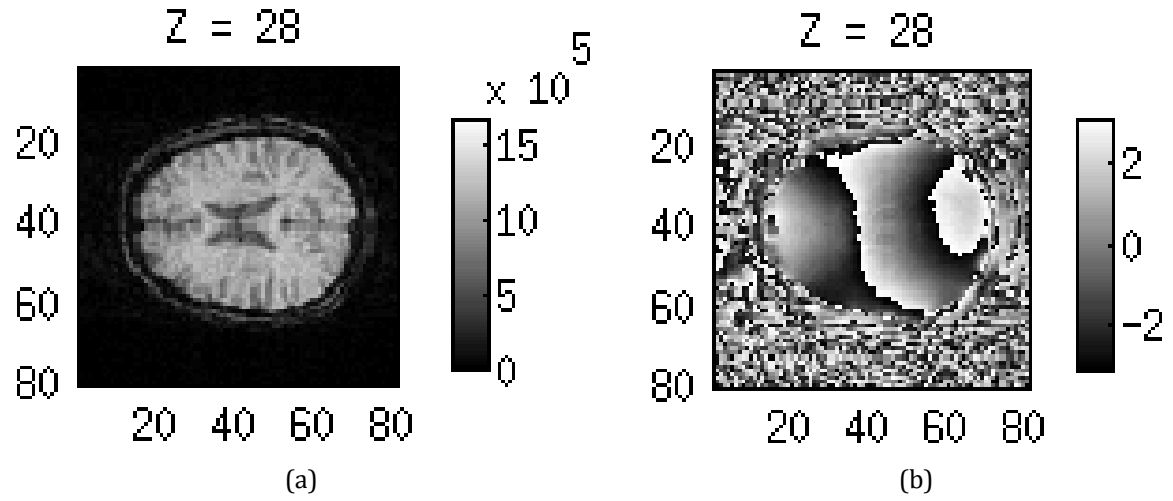


Figure 17. (a) Magnitude and (b) phase of one slice in the (k_x, k_y) -plane data acquired with the PRESTO-CAN method after inverse Fourier transformation to the spatial domain and cropping.

3.3 Parallel Imaging and SENSE

Parallel imaging makes it possible to reduce the scan time with maintained image quality by making use of multiple receiver coils. There is a multitude of different parallel imaging methods that has been developed mainly for Cartesian sampled data, of which SENSitivity Encoding (SENSE) is one. Since PRESTO-CAN uses Cartesian sampled 2D profiles in the ky -direction, it is possible to implement SENSE in this dimension, which is the purpose of this thesis.

3.3.1 History of Parallel Imaging

The use of multiple receiver coils with differing sensitivity during acquisition of MR images, so-called phased array coils or multicoil arrays, was originally developed in order to reduce SNR [20]. Soon after their development, multiple researchers also suggested how they can be utilized in order to reduce scan time [21], [22]. This principle was named parallel imaging, and two main methods were developed: SMASH (SiMultaneous Acquisition of Spatial Harmonics) [23], which works by preventing the aliasing while still in k -space; and SENSE [5], which in contrast to SMASH works by removing the aliasing after the transformation to the spatial domain. The SENSE method was later further developed [24] in order to make it possible to use it also with non-Cartesian sample patterns, called CG-SENSE after the conjugate-gradient (CG) iteration method which it is based on. Non-Cartesian SENSE processing is however much more complicated than ordinary SENSE, which is the reason this thesis will concentrate on implementing SENSE in a Cartesian sampled plane only. Another widely spread parallel imaging method is GRAPPA (Generalized Autocalibrating Partially Parallel Acquisitions) [25], which is based on SMASH and also works in k -space.

3.3.2 Unfolding the Image Using SENSE

As stated above, the SENSE method seeks to restore the information lost due to the under-sampling of k -space after the image has been transformed to the spatial domain through inverse Fourier transformation, by making use of the varying sensitivities of the multiple receiver coils. When SENSE is applied, scan time is reduced by skipping rows of k -space, increasing the sample distance. As explained in section 3.1.4, this leads to a reduced FOV and aliased or folded images, where the outer parts has been folded in and superimposed on the central parts.

In order to be able to unfold the image, we need to know exactly how the folding is done. Let the number of rows in the original image be L , and the number of rows of the folded image (= the number of rows of k -space scanned) be L/R . R is the reduction rate (also known as acceleration factor or SENSE factor), representing the times of rows of k -space less that will be scanned when using SENSE. R has to be chosen such that L/R becomes an even integer number. Let the number of pixels from the unfolded image that are superimposed at one point in the folded image be N_A . N_A either takes the value $\lfloor R \rfloor$ or $\lceil R \rceil$ ¹. If R is an integer, N_A is consequently the same in all pixels of the folded image; otherwise it will vary between different parts of the image.

¹ As a reminder, $\lfloor \cdot \rfloor$ denotes downwards rounding to the nearest integer and $\lceil \cdot \rceil$ upwards rounding.

Let us take a look at the example in Figure 18, with the acceleration factor 4 and the same number of coils (A to D). The value of a pixel in the folded image from coil A (I_A) is a summation of the pixel values in the unfolded image M that has been superimposed (M_1, \dots, M_4) times the coil sensitivity at their respective positions (C_{A1}, \dots, C_{A4}). Similarly for all coils give:

$$\begin{aligned} I_A &= C_{A1}M_1 + C_{A2}M_2 + C_{A3}M_3 + C_{A4}M_4 \\ I_B &= C_{B1}M_1 + C_{B2}M_2 + C_{B3}M_3 + C_{B4}M_4 \\ I_C &= C_{C1}M_1 + C_{C2}M_2 + C_{C3}M_3 + C_{C4}M_4 \\ I_D &= C_{D1}M_1 + C_{D2}M_2 + C_{D3}M_3 + C_{D4}M_4 \end{aligned} \quad (15)$$

The number of superimposed pixels N_A is the number of unknowns in the equation that gives us the pixel value of I_A , and in this case $N_A = 4$. If we have the same amount of linearly independent equations, it is possible to solve the equation system. More equations can be gained by adding multiple receiver coils. In order for the equation system to be solvable, the number of receiver coils has to be at least as high as the reduction rate.

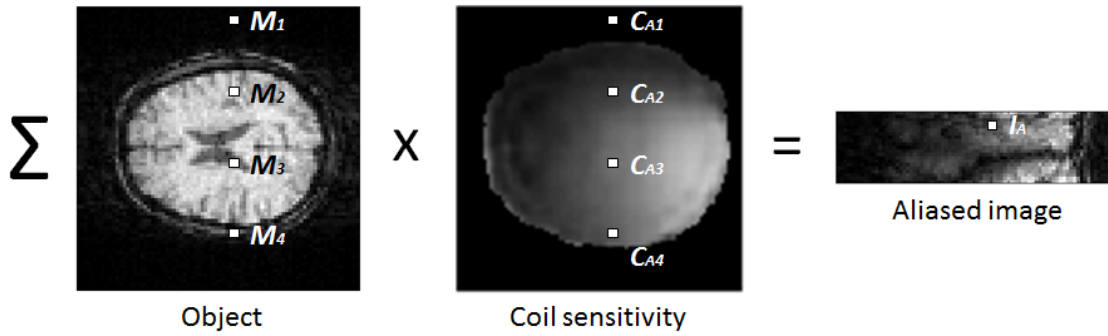


Figure 18. Schematic depiction of how the pixel values of a folded image is calculated. (Image idea from [26]).

In order to solve the equation system, we need to know exactly which rows that are superimposed at different values of the reduction rate. The aliasing can occur in different manners depending on the way k -space is sampled. During the simulated k -space sampling that was performed in the initial steps of the implementation in this thesis (Section 4.1-4.2), as well as when sampled k -space rows are removed a posteriori in order to increase the reduction rate (Section 5.3), the folding of the image is done in a way that we can call “from both sides”. Table 1 gives a schematic view of how such aliasing from both sides occurs in the case of an image with 16 rows.

R	1	1,33	2	2,66	4
L/R	16	12	8	6	4

1					
2					
3	y				
4	1	3 15			
5	2	4 16			
6	3	5	y		
7	4	6	1	5 13	
8	5	7	2	6 14	
9	6	8	3	7 15	
10	7	9	4	8 16	
11	8	10	5	9 1	
12	9	11	6	10 2	
13	10	12	7	11 3	
14	11	13 1	8	12 4	
15	12	14 2			
16					

1					
2					
3					
4					
5					
6					
7					
8					
9					
10					
11					
12					
13					
14					
15					
16					

1					
2					
3					
4					
5					
6					
7					
8					
9					
10					
11					
12					
13					
14					
15					
16					

1					
2					
3					
4					
5					
6					
7					
8					
9					
10					
11					
12					
13					
14					
15					
16					

1					
2					
3					
4					
5					
6					
7					
8					
9					
10					
11					
12					
13					
14					
15					
16					

1					
2					
3					
4					
5					
6					
7					
8					
9					
10					
11					
12					
13					
14					
15					
16					

1					
2					
3					
4					
5					
6					
7					
8					
9					
10					
11					
12					
13					
14					
15					
16					

1					
2					
3					
4					
5					
6					
7					
8					
9					
10					
11					
12					
13					
14					
15					
16					

1					
2					
3					
4					
5					
6					
7					
8					
9					
10					
11					
12					
13					
14					
15					
16					

1					
2					
3					
4					
5					
6					
7					
8					
9					
10					
11					
12					
13					
14					
15					
16					

1					
2					
3					
4					
5					
6					
7					
8					
9					
10					
11					
12					
13					
14					
15					
16					

1					
2					
3					
4					
5					
6					
7					
8					
9					
10					
11					
12					
13					
14					
15					
16					

1					
2					
3					
4					
5					
6					
7					
8					
9					
10					
11					
12					
13					
14					
15					
16					

1					
2					
3					
4					
5					
6					
7					
8					
9					
10					
11					
12					
13					
14					
15					
16					

1					
2					
3					
4					
5					
6					
7					
8					
9					
10					
11					
12					
13					
14					
15					
16					

1					
2					
3					
4					
5					
6					
7					
8					
9					
10					
11					
12					
13					
14					
15					
16					

1					
2					
3					
4					
5					
6					
7					
8					
9					
10					
11					
12					
13					
14					
15					
16					

1					
2					
3					
4					
5					
6					
7					
8					
9					
10					
11					
12					
13					
14					
15					
16					

1					
2					
3					
4					
5					
6					
7					
8					
9					
10					
11					
12					
13					
14					
15					
16					

1					
2					
3					
4					
5					
6					
7					
8					
9					
10					
11					
12					
13					
14					
15					
16					

1					
2					
3					
4					
5					
6					
7					
8					
9					
10					
11					
12					
13					
14					
15					
16					

1					
2					
3					
4					
5					
6					
7					
8					
9					
10					
11					
12					
13					
14					
15					
16					

1					
2					
3					
4					
5					
6					
7					
8					
9					
10					
11					
12					
13					
14					
15					
16					

1					
2					
3					
4					
5					
6					
7					
8					
9					
10					

In the case where the folding is done “from both sides”, we can derive the following summation formula of how the pixel values of each of the rows y in the aliased images I_k are calculated:

$$I_k(y) = \sum_{n=0}^{N_B} C_k(y + (L - L/R)/2 \pm nL/R) M(y + (L - L/R)/2 \pm nL/R) \quad \forall k = 1, \dots, N_c. \quad (16)$$

N_c denotes the number of coils, and N_B either takes the value $\lfloor N_A/2 \rfloor$ or $\lceil N_A/2 \rceil$, determined by the limitation that the indices of C_j and M must be between 1 and L . Basically, all additions and subtracting of different multiples of the L/R term that can be done without the indices exceeding this limit should be included in the summation. The equation system can also be written in matrix form according to the following:

$$\begin{bmatrix} I_1(y) \\ I_2(y) \\ \vdots \\ I_{N_c}(y) \end{bmatrix} = \begin{bmatrix} C_1(y + (L - \frac{L}{R})/2) & \cdots & C_1(y + (L - \frac{L}{R})/2 \pm N \frac{L}{R}) \\ \vdots & \ddots & \vdots \\ C_{N_c}(y + (L - \frac{L}{R})/2) & \cdots & C_{N_c}(y + (L - \frac{L}{R})/2 \pm N \frac{L}{R}) \end{bmatrix} \begin{bmatrix} M(y + (L - \frac{L}{R})/2) \\ \vdots \\ M(y + (L - \frac{L}{R})/2 \pm N \frac{L}{R}) \end{bmatrix}. \quad (17)$$

The number of columns in C and the number of rows in M is determined by how many times the factor L/R can be added as long as the indices of $C_{ij}(y)$ and $M_i(y)$ are still between 1 and L . The corresponding summation formula and equation system in the case when the folding is done “from one side” becomes as follows:

$$I_k(y) = \sum_{n=0}^{N_A} C_k(y + nL/R) M(y + nL/R) \quad \forall k = 1, \dots, N_c. \quad (18)$$

Written on matrix form, the equation system likewise becomes

$$\begin{bmatrix} I_1(y) \\ I_2(y) \\ \vdots \\ I_{N_c}(y) \end{bmatrix} = \begin{bmatrix} C_1(y) & \cdots & C_1(y + N_A \frac{L}{R}) \\ \vdots & \ddots & \vdots \\ C_{N_c}(y) & \cdots & C_{N_c}(y + N_A \frac{L}{R}) \end{bmatrix} \begin{bmatrix} M(y) \\ \vdots \\ M(y + N_A \frac{L}{R}) \end{bmatrix}. \quad (19)$$

This matrix equation (for either of the two types of aliasing) can finally also be notated in dense form as

$$I = CM. \quad (20)$$

If both I and C are known, the original image M can be solved. If C is a square matrix, which is the case when the number of superimposed rows equals the number of coils, and if we disregard the influence of noise, M is solved simply as

$$M = C^{-1}I. \quad (21)$$

The most general solution is however

$$\hat{M} = [(C^H \psi^{-1} C)^{-1} C^H \psi^{-1}] I, \quad (22)$$

where ψ is the $N_c \times N_c$ noise correlation matrix, the diagonal elements containing noise variance from single coil elements and the off-diagonal elements containing the noise correlation between different coil elements. The superscript H denotes the transposed complex conjugate. However, very often the correlation between different coils are negligible while the noise variance of the different coils are equal, which makes it possible to replace ψ by the identity matrix [10], and the solution simplifies to

$$\hat{M} = [(C^H C)^{-1} C^H] I, \quad (23)$$

where $(C^H C)^{-1} C^H$ is the pseudo-inverse of C (also denoted C^+), which gives a least squares approximation in cases when C is not square. If $N_c > N_A$, the equation system becomes overdetermined, and the extra degrees of freedom are used to decrease the noise.

3.3.3 Noise Amplification

Using SENSE will always increase the noise since the total acquisition time is shorter. The relation between the SNR when using SENSE compared to when not using it is described by

$$\text{SNR}_{\text{SENSE}} = \frac{\text{SNR}_{\text{NORMAL}}}{g\sqrt{R}}, \quad (24)$$

where g is the so-called geometry factor, which varies from pixel to pixel in the unfolded image. It depends on the matrix $(C^T \psi^{-1} C)$ and its inverse according to

$$g_i = \sqrt{[(C^H \psi^{-1} C)^{-1}]_{ii} [C^H \psi^{-1} C]_{ii}} \geq 1, \quad (25)$$

where $[(C^H \psi^{-1} C)^{-1}]_{ii}$ and $[C^H \psi^{-1} C]_{ii}$ denotes the diagonal element of row/column i [5]. The more pixels superimposed and the less sensitivity difference between the receiver coils, the greater the geometry factor will be. Another factor that affects the noise amplification is the *conditioning* of the matrix $[C^H \psi^{-1} C]$. The conditioning number of a matrix \mathbf{A} is defined as $\|\mathbf{A}\| \cdot \|\mathbf{A}^{-1}\|$, where $\|\mathbf{A}\|$ is the *matrix norm* of \mathbf{A} , related to the vector norm as $\|\mathbf{A}\| = \sup_{x \neq 0} \frac{\|\mathbf{A}x\|}{\|x\|}$ [27]. The noise amplification that follows from poor conditioning of $[C^H \psi^{-1} C]$ can be reduced by a process called *regularization*. One regularization method proposed in [28] is to simply add a term λ proportional to the unit matrix. In this case, equation (23) for determining M is changed to

$$\hat{M} = [(C^H C + \lambda I') C^H] I, \quad (26)$$

where the identity matrix has been notated as I' in order not to confuse it with the aliased image I . Adding this term will increase the SNR at the cost of the unfolding not becoming as precise. According to [28], a good choice is $\lambda = 10^{-3}$ since this gives a slight increase of SNR without significantly affecting the unfolding in a negative way. That this is generally a good value of λ has also been confirmed in [29].

3.3.4 Determining Sensitivity Maps

The sensitivity maps of the receiver coils show how the intensity of the output images varies spatially. In order to achieve good results with SENSE, it is crucial to be able to determine high quality sensitivity maps. Estimation of the sensitivity maps is usually done by a reference scan with full FOV. Three main methods exist to achieve the sensitivity map: division between the surface coil images and a body coil or quadrature image, division between the surface coil images and a sum-of-squares image, and theoretical determination using Biot-Savart's law.

3.3.4.1 Division by Body Coil or Quadrature Image

The most intuitive way of determining the sensitivity maps is to divide the images from the respective surface receiver coils of varying sensitivity with a reference image of homogenous sensitivity from a so-called body coil:

$$C(x, y) = \frac{I_k(x, y)}{I_{ref}(x, y) + \epsilon} \quad \forall k = 1 \dots N_C, \quad (27)$$

where I_k denotes the image from receiver coil k and I_{ref} is the reference image to which an arbitrarily small value ϵ is added in order to avoid division by 0. The unreliable values that still result when this occurs is dealt with during the refinement of the sensitivity maps described further on. In this thesis, a quadrature image calculated from the surface coil images is used instead of a body coil image (cf. Section 3.1.6).

3.3.4.2 Division by Sum-of-Squares image

Alternatively, instead of the body coil or quadrature image the so-called sum-of-squares [30] of the surface coil images can be used, which is calculated according to

$$I_{sos}(x, y) = \sqrt{\sum_{k=1}^{N_C} |I_k(x, y)|^2}, \quad (28)$$

where I_k denotes the images from the N_C different surface receiver coils. Division by the body coil image usually gives a more homogenous result, but dividing with the sum-of-squares might be more reliable since the body coil image cannot be retrieved at the exact same moment as the images from the surface coils. Another problem with the sum-of-squares image is that it becomes purely real since the magnitude of the surface coil images are used in the summation. Since it is supposed to resemble the original image that we want to reconstruct, and this is complex due to heterogeneities in the magnetic field, a phase resembling the one of the original image need to be added somehow. In our implementation, this was done by summing the surface coil images, dividing by the magnitude of the sum in order to get only the phase, and multiplying this with the sum-of-squares image according to the following:

$$I_{sos}(x, y) = \sqrt{\sum_{k=1}^{N_C} |I_k(x, y)|^2} \cdot \frac{\sum_{k=1}^{N_C} I_k}{|\sum_{k=1}^{N_C} I_k|}. \quad (29)$$

In this way, the phase variations of the images from the receiver coils and that of the sum-of-squares image become somewhat similar. The division between them, by which the sensitivity maps are calculated, will therefore contain fairly slow phase variations.

3.3.4.3 Biot-Savart's law

A possible third method to determine the sensitivity maps is to calculate them theoretically using the Biot-Savart's law [31], but this is very impractical because of several reasons. First, the coil sensitivity is usually not static but dependent on the object in the MR-scanner since it will affect the magnetic field, and separate sensitivity maps should therefore be calculated for every new subject. Furthermore, this method presupposes knowledge of the exact placement of the coils, and is furthermore generally very complicated to use and thus not regarded in this thesis.

3.3.4.4 Refining the Raw Sensitivity Maps

One problem that arises during the division with a body coil/quadrature or sum-of-squares image is that ambiguous results will be rendered in areas where the proton density is zero or dominated by noise. The sensitivity maps will also be noisy. These problems have to be dealt with so that the resulting sensitivity maps become more or less independent on the exact proton density during the reference scan. There are several different methods to improve the raw sensitivity maps by fixing these problems, of which two are polynomial fitting [32], [5] and normalized convolution [33], [34].

3.3.4.5 Polynomial Fitting

Polynomial fitting is the method for improving the sensitivity maps which Pruessman et al. suggests in the original SENSE article [5]. First, the area which the sensitivity map is supposed to cover must be defined. In order to identify the areas of the raw sensitivity maps containing pure noise, a threshold is used. The noise is then removed by density filtering (for example erosion² followed by dilation³ [35]). Then, the holes are filled and the borders extended using a region growing algorithm. A polynomial is then locally fit on all the pixels (x_0, y_0) belonging to this area, given by

$$s(x, y) = \sum_{l,m=0}^P c_{l,m} (x - x_0)^l (y - y_0)^m, \quad (30)$$

where P is the order of the polynomial. The least squares problem that arise when minimizing the error between the fitted polynomial and the value of the raw sensitivity map in every pixel gives the following set of equations:

$$\sum_{l',m'=0}^P c_{l,m} A_{ll'mm'} = b_{lm}, \quad (31)$$

where

$$A_{ll'mm'} = \sum_{x,y} w(x, y) (x - x_0)^{l+l'} (y - y_0)^{m+m'}, \quad (32)$$

$$b_{lm} = \sum_{x,y} w(x, y) s_{x,y} (x - x_0)^l (y - y_0)^m, \quad (33)$$

where $s_{x,y}$ are the values of the raw sensitivity map and $w(x,y)$ is a weighting function reflecting the significance of the values of $s_{x,y}$, based on a Gaussian function.

3.3.4.6 Normalized Convolution

Normalized convolution is a method that locally reconstructs a signal via projections on a set of basis functions $\{\mathbf{b}_i\}$, and also makes use of a certainty function that tells how reliable each of the pixel values in the input signal is. The basis functions are usually polynomials, $\{1, x, y, x^2, y^2, xy, \dots\}$, and in this case the method becomes equivalent to a local Taylor series expansion [36]:

$$\hat{f}(\mathbf{x}, \mathbf{x}_0) = r_0(\mathbf{x}_0) + r_1(\mathbf{x}_0)x + r_2(\mathbf{x}_0)y + r_3(\mathbf{x}_0)x^2 + r_4(\mathbf{x}_0)xy + r_4(\mathbf{x}_0)y^2, \quad (34)$$

² A method that expands and softens the edges of a binary object.

³ A method that shrinks and prunes the edges of a binary object.

where $\{x, y\}$ are the local coordinates with respect to \mathbf{x}_0 and $\mathbf{r}(\mathbf{x}_0)$ are the projection coefficients, which in turn are determined by solving least-squares problem that makes up the approximation error [37]

$$\varepsilon(\mathbf{x}_0) = \sum (f(\mathbf{x}_0) - \hat{f}(\mathbf{x}, \mathbf{x}_0))^2 c(\mathbf{x}) a(\mathbf{x} - \mathbf{x}_0), \quad (35)$$

where $0 \leq c(\mathbf{x}) \leq 1$ is the certainty function that defines how reliable the value of every pixel is. The most simple way of defining the certainty function, which in many cases is enough to make it usable, is to simply let $c(\mathbf{x}) \in [0,1]$. $a(\mathbf{x})$ is the so-called applicability function that localizes the polynomial fit, and can also be seen as a kind of certainty for the basis functions. It can have several different looks depending on the application, but a simple and usual case is to let it be an isotropic Gaussian kernel, where the standard deviation can be adjusted according to the specific needs. The solution to this least-squares problem turns out to be

$$\mathbf{r} = (\mathbf{B}^T \mathbf{W}_a \mathbf{W}_c \mathbf{B})^{-1} \mathbf{B}^T \mathbf{W}_a \mathbf{W}_c \mathbf{f}, \quad (36)$$

where \mathbf{B} is the set of the basis functions $\{\mathbf{b}_i\}_1^m$, $\mathbf{W}_a = \text{diag}(\mathbf{a})$ and $\mathbf{W}_c = \text{diag}(\mathbf{c})$. If we write out the contents of the matrices, we get the expression

$$\mathbf{r} = \begin{bmatrix} (\mathbf{a} \cdot \mathbf{c} \cdot \mathbf{b}_1, \mathbf{b}_1) & \cdots & (\mathbf{a} \cdot \mathbf{c} \cdot \mathbf{b}_1, \mathbf{b}_m) \\ \vdots & \ddots & \vdots \\ (\mathbf{a} \cdot \mathbf{c} \cdot \mathbf{b}_m, \mathbf{b}_1) & \cdots & (\mathbf{a} \cdot \mathbf{c} \cdot \mathbf{b}_m, \mathbf{b}_m) \end{bmatrix}^{-1} \begin{bmatrix} (\mathbf{a} \cdot \mathbf{c} \cdot \mathbf{b}_1, \mathbf{f}) \\ \vdots \\ (\mathbf{a} \cdot \mathbf{c} \cdot \mathbf{b}_m, \mathbf{f}) \end{bmatrix}. \quad (37)$$

If only a 0th grade polynomial is used as basis function (that is, a function which is constantly 1), normalized convolution simplifies to normal averaging. This consists of two convolutions and a point-wise division according to the following:

$$\bar{f}(x, y) = \frac{(f(x, y) \cdot c(x, y)) * a(x, y)}{c(x, y) * a(x, y)}. \quad (38)$$

Normalized convolution with polynomials as basis functions in large parts carry out the same thing as the polynomial fitting proposed in [2]. In the implementation in this thesis, we will therefore examine how good normalized convolution works as an alternative to polynomial fitting in order to refine sensitivity maps.

3.3.4.7 Possibility of Using Lower Resolution

Applying normalized convolution or polynomial fitting to a raw sensitivity map can be quite computationally demanding, especially in 3D. Since the sensitivity normally changes spatially slowly over the volume, time can be saved by using volumes of lower resolution to create the sensitivity map than is used for the reconstructed image volumes themselves, and later use interpolation to change them into the same resolution. [10] suggests using resolutions as low as 32 x 32 x 32 voxels for a volume of size 40 x 48 x 48 cm³. This possibility has, however, not been utilized in this implementation since it was regarded that the risk of lost image quality because of the up- and down sampling was not worth the decreased computational time.

3.3.4.8 Applying Normalized Convolution on Complex Images

A problem that arises especially when working with in vivo data is that normalized convolution cannot be used right away on the raw sensitivity maps in all cases. Normalized convolution was originally intended mainly for use on purely real images. The raw sensitivity maps that we are applying it on in this implementation are, however, complex because of inhomogeneities in the

magnetic field. In computer simulations and in vitro experiments with phantoms, the phase variations over the image are usually quite slow. When working with in vivo MR data, however, the phase can change quickly, not at least including jumps between $-\pi$ and π .

When normalized convolution is applied on a region where the values of neighboring voxels differ significantly from each other, the result might be that they cancel out each other. The resulting magnitude image will also be affected in unexpected ways. This problem can be solved by only applying normalized convolution on the magnitude of the raw sensitivity maps while keeping the phase as it is. That can be done by using the magnitude of the raw sensitivity map as input to the normalized convolution, and multiplying the output with $\exp(j\varphi(C_k))$, where $\varphi(C_k)$ is the phase of the raw sensitivity maps.

Alternatively, normalized convolution can be performed separately on the magnitude and the phase, using an applicability function with a smaller standard deviation in order to reduce the risk of unwanted cancelling out of nearby voxels of strongly varying values. In this case, normalized convolution is performed twice on each raw sensitivity map using different applicability functions, and the magnitude of the first output is multiplied with $\exp(j\varphi(C_k))$, where $\varphi(C_k)$ is the phase of the second output.

4 Implementation

In this chapter, the process of implementing the SENSE reconstruction in Matlab is described.

4.1 2D Implementation of SENSE

The first step of creating a SENSE reconstruction algorithm was to implement it in a Cartesian sampled 2D environment. This was done based on a Matlab script developed earlier in the project that reconstructs images from k -space, as well as a function that generates ellipses in k -space that can be used to create phantom images to test the algorithm on.

4.1.1 Simulation of Coils

In order to be able to simulate SENSE reconstruction in Matlab before using data from a real MR scan, the first thing that had to be done was to simulate varying coil sensitivity. Since the MR-scanner that was going to be used for the in vivo experiments has an array of 8 receiver coils, the same number of coils were simulated in the Matlab script. The sensitivities were presumed to vary sinusoidally according to:

$$c(x, y) = (0.5 + 0.5 \sin(2\pi f_x x)) (0.5 + 0.5 \cos(2\pi f_y y)). \quad (39)$$

The sensitivity difference was also presumed to be complex with a linear phase varying in the same direction as the sine wave in the function above. This is achieved by multiplying the function above with a factor $\exp(j2\pi f_0 x)$, such that the sensitivity map function is adjusted to

$$c(x, y) = \exp(j2\pi f_0 x) (0.5 + 0.5 \sin(2\pi f_x x)) (0.5 + 0.5 \cos(2\pi f_y y)), \quad (40)$$

where f_x and f_y defines how fast the sensitivity changes spatially. In order for the absolute value to vary between 0 and 1 in the x -direction and in the y -direction be 1 in the middle with 0 in the edges, with a resolution of 80×80 pixels, f_x and f_0 should be set to $1/40$ and f_y to $1/20$. Examples of how the absolute value and phase of the sensitivity maps varies in the spatial domain can be seen in Figure 19.

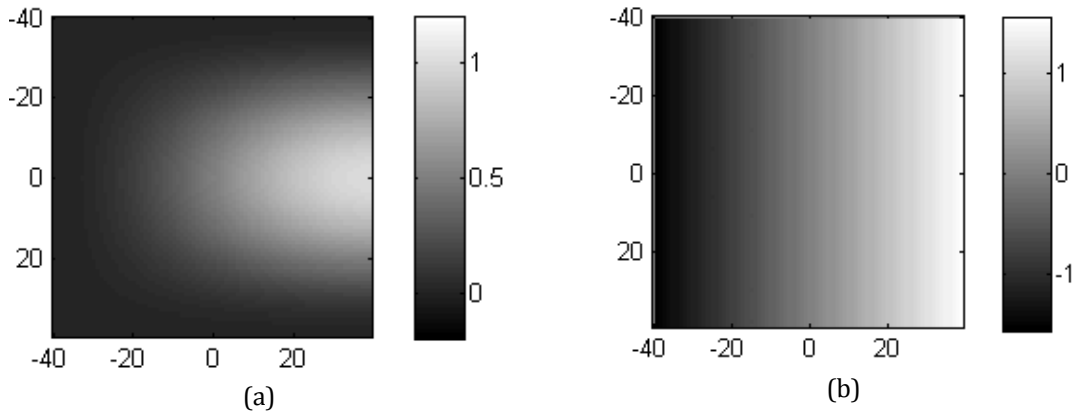


Figure 19. Theoretical sensitivity map of a simulated surface coil showing the (a) absolute value and (b) phase.

However, since the phantom images used in the simulation were generated directly in the Fourier domain, the Fourier transform of the coil sensitivity functions had to be used and then convolved with the generated images (since multiplication in the spatial domain corresponds to convolution in the Fourier domain). The Fourier transform of (40) is a convolution of the Fourier transform's sine part and cosine part according to

$$C(u, v) = (0.5 \delta(u - f_0) + 0.25j(\delta(u + f_x - f_0) - \delta(u - f_x - f_0))) * (0.5 \delta(v) + 0.25(\delta(v + f_y) + \delta(v - f_y))) \quad (41)$$

This can be visualized graphically according to Figure 20 below.

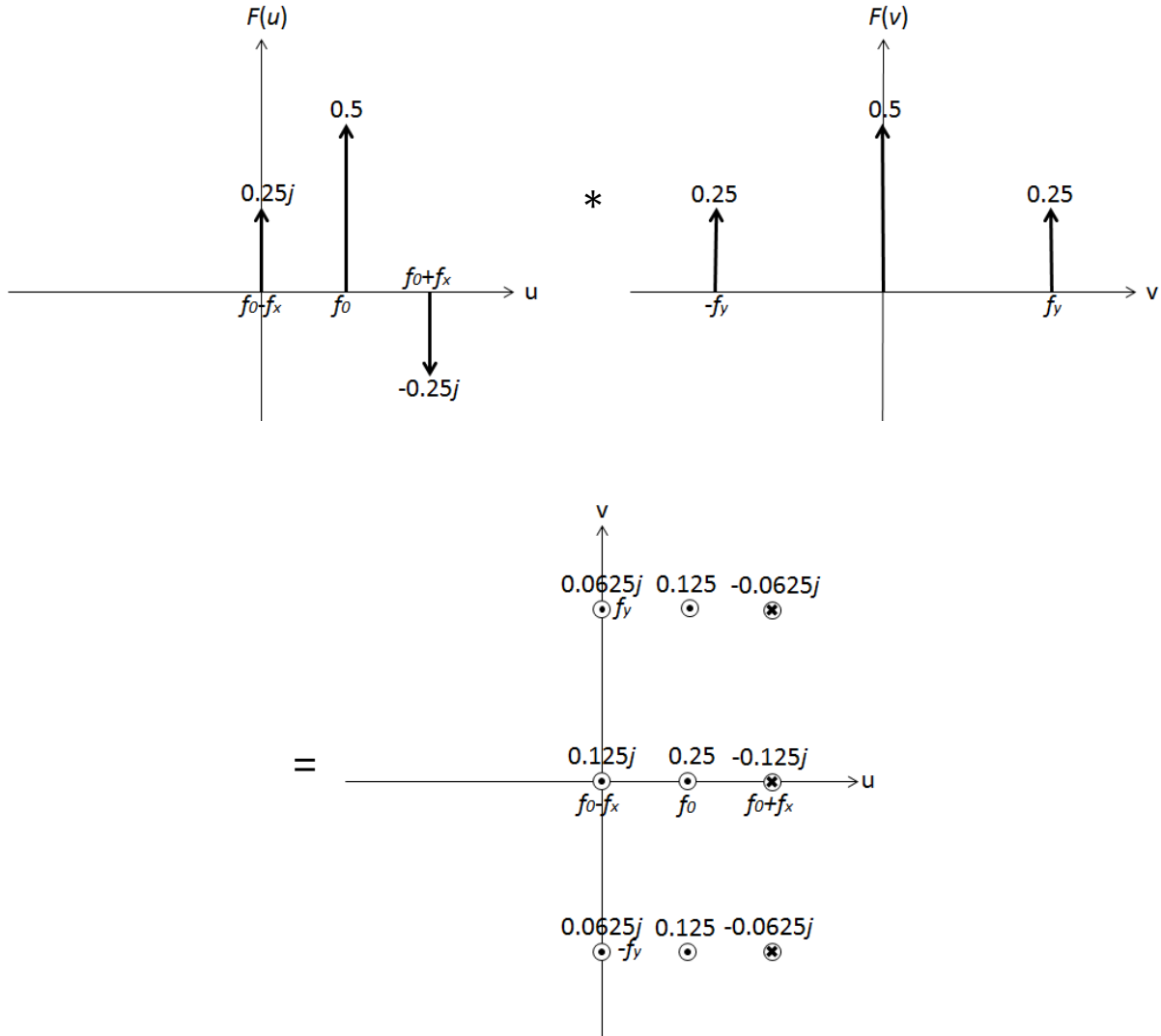


Figure 20. Graphical depiction of the Fourier transform of the simulated sensitivity maps.

As can be seen, the Fourier transform of the sensitivity map is a summation of nine Dirac delta functions according to

$$C(u, v) = 0.25 \delta(u - f_0, v) + 0.125j \delta(u - f_0 + f_x, v) - 0.125j \delta(u - f_0 - f_x, v) + 0.125 \delta(u - f_0, v - f_y) + 0.125 \delta(u - f_0, v + f_y) + 0.0625j \delta(u - f_0 + f_x, v - f_y) + 0.0625j \delta(u - f_0 + f_x, v + f_y) - 0.0625j \delta(u - f_0 - f_x, v - f_y) - 0.0625j \delta(u - f_0 - f_x, v + f_y). \quad (42)$$

Since multiplication in the spatial domain corresponds to convolution in the Fourier domain, generating phantoms with intensity varying according to the sensitivity map shown in Figure 19 is done by convolving it with the result in Figure 20. Since this function only consists of Dirac delta functions, the convolution simply consists of additions of phase shifted versions of the phantom function. And since rotation in the spatial domain corresponds to rotation in the Fourier domain, sensitivity maps where the intensity varies in other directions can be achieved simply by rotating the function in Figure 20. This was done in the implementation in order to

simulate eight different surface coils. The phantom was simulated by summing ellipses that were generated in k -space. The Fourier transform of an ellipse is a sinc-like so-called “jinc”-function containing a first-order Bessel function. A previously developed Matlab function that generates these functions was used in the implementation.

4.1.2 Measuring Coil Sensitivity

A body coil image was simulated by generating a phantom image without any additional convolutions, giving a perfectly homogenous image. The eight surface coils images were likewise generated using the technique described above. The phantom used was a simplified variant of the one used in [5]. The phantom included some “holes” of value 0 in order to test the algorithm’s ability to reconstruct the sensitivity map also at these areas. The possibility of adding Gaussian distributed noise to the image resulting in a given SNR was implemented. As an alternative to the body coil image, the sum-of-squares image was calculated according to (28). As described in Section 3.3.4, the raw sensitivity maps were calculated by dividing the 8 surface coil images with either the body coil image or the sum-of-squares image. See Figure 22 for images of the phantom.

The method chosen for improving the raw sensitivity maps was normalized convolution, partly because it is a method developed at Linköping University, partly in order to evaluate how good it works as an alternative to polynomial fitting, and partly because of that the Matlab code for it is included in the Spatial Domain Toolbox by Farnebäck, available online [38]. As basis functions, polynomials up to order 3 were created. As applicability function a Gaussian with selectable spatial size and standard deviation was used, generated with a function also included in the mentioned toolbox. The basis functions and examples of applicability functions are shown in Figure 21.

The certainty function was defined by putting a threshold on the sum-of-squares image, setting it to 0 for areas only containing noise and 1 elsewhere. One advantage of the sum-of-squares image is that much of the noise is averaged out due to the summation. With the mentioned basis functions, applicability function and certainty function used as input, the normalized convolution was carried out. The normalized convolution both fills out holes in the raw sensitivity map as well as performs some extrapolation. How large holes that can be filled and the amount of extrapolation done depends on the size of the applicability function.

In areas where the whole or large parts of the applicability function covers values deemed by the certainty function to be certain, we will get useful values for the refined sensitivity map, and in areas where the applicability function only covers uncertain values, the result is undefined and later set to 0. However, where just a small portion of the pixels covered by the applicability function are certain, i.e. at the outer edges of the raw sensitivity map, the result will be heavily varying, unreliable values. In order to avoid these causing disturbances, they are filtered out by multiplying the refined sensitivity map with a mask that is retrieved by filling the holes and dilating [35] the certainty function to a given degree. This can also be preceded by eroding [35] it in order to put to zero certainty pure noise areas that might have survived the previous threshold.

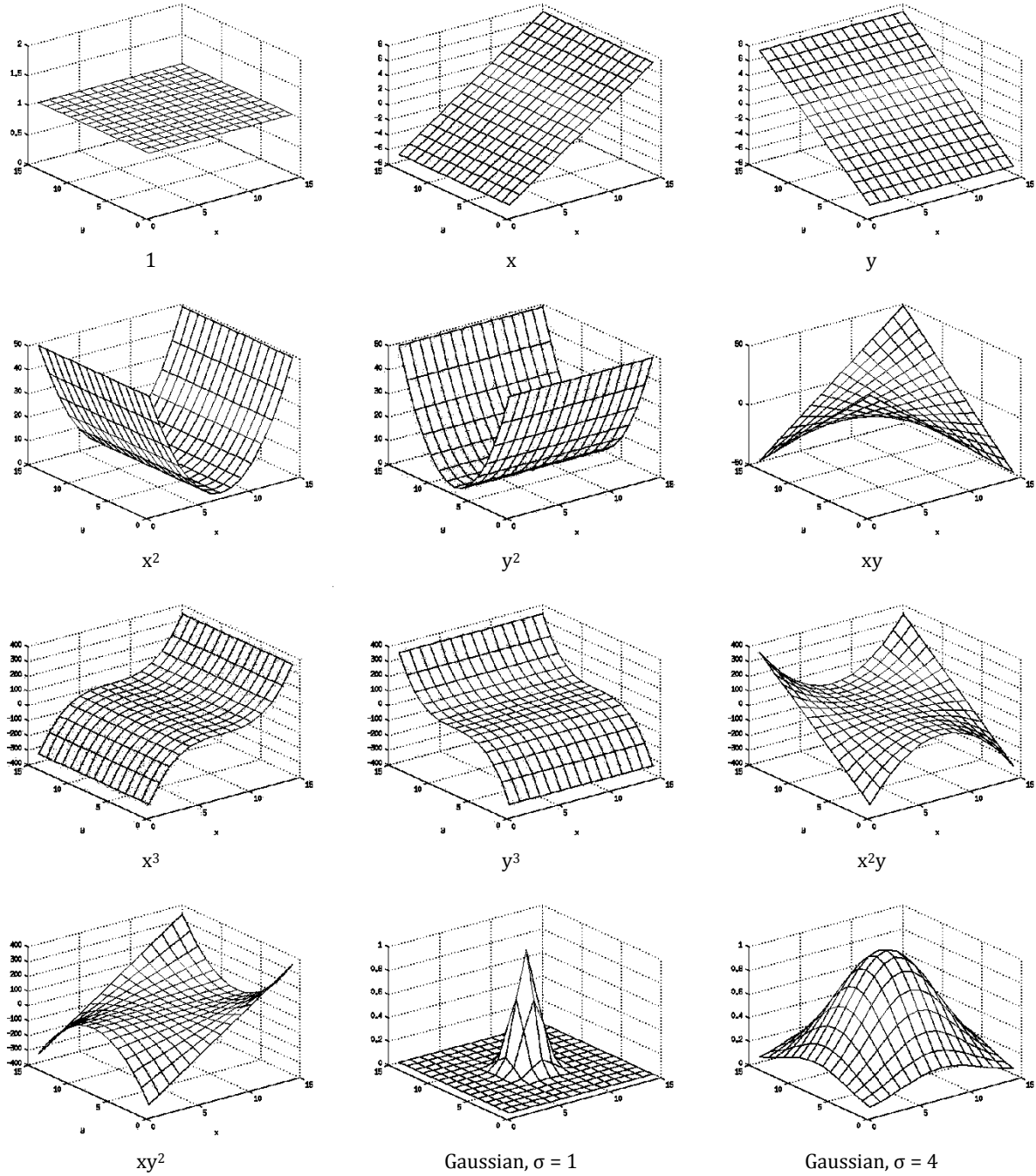


Figure 21. 2D polynomial basis functions and two Gaussian applicability functions with differing standard deviations, used as input to normalized convolution.

Figure 22 shows the various steps in the process of creating a sensitivity map. The image size was 80×80 pixels, and as applicability function for the normalized convolution a Gaussian kernel of size of 11×11 pixels with standard deviation 10 was used (for in vivo images with much faster variations in intensity, much smaller values of the standard deviation should be used in order not to smooth out details). Some random Gaussian noise was added, with an estimated SNR = 20.

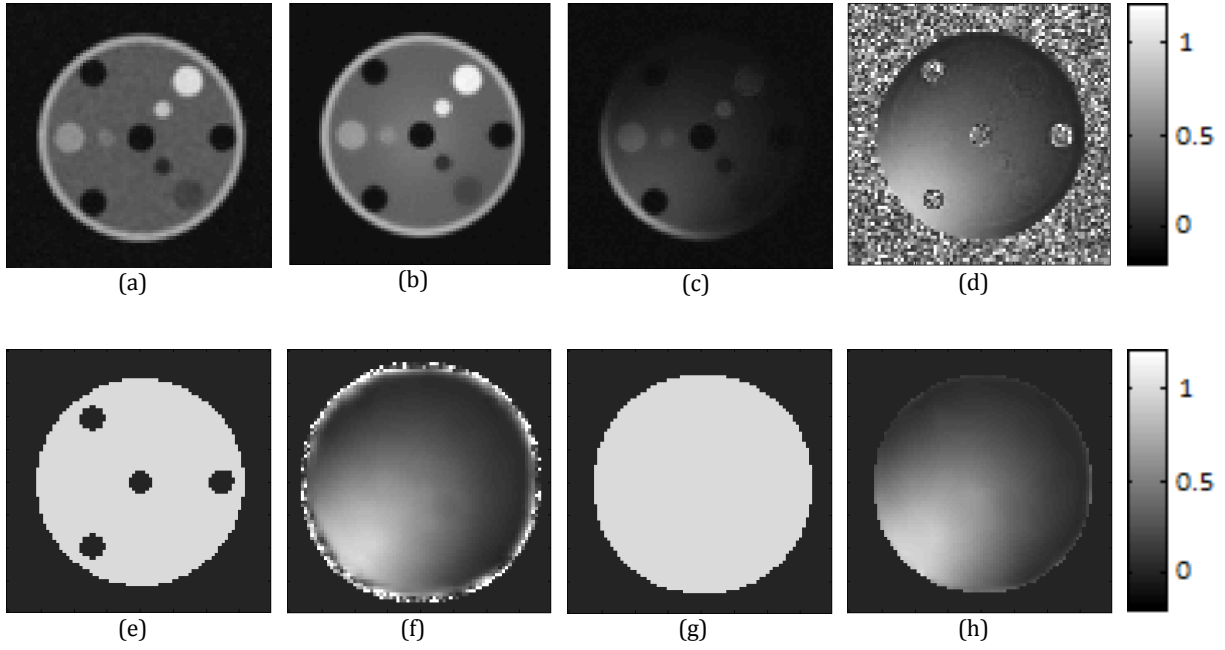


Figure 22. (a) Simulated body coil image. (b) Sum-of-squares image. (c) Simulated surface coil image. (d) Raw sensitivity map. (e) Certainty function. (f) After normalized convolution. (g) Mask defining reliable pixels. (h) Final sensitivity map.

4.1.3 SENSE Reconstruction

The phantom to be reconstructed was generated in the same way as the one used to measure the coil sensitivities. It was changed slightly by replacing the 0 value holes with ellipses of positive values in order to test that they can be reconstructed properly. This phantom was generated in k -space using a coordinate system of R times fewer rows than the phantom used during the simulated reference scan, where R is the reduction factor chosen by the user. In the following example shown in Figure 23, $R = 3$. After inverse Fourier transformation, the result is a set of folded images from the 8 simulated receiver coils (see Figure 23 (a)).

Using the theory from Section 3.3.2 on how the folding is done, a C matrix for each of the pixels in the folded images was determined. Using (26) in order to retrieve the original image results in a set of images where the pixels superimposed in the folded images have been separated. Combining and reshuffling the order of the rows gives the reconstructed image (see (b)-(e)). The output in (e) shows very small differences to the simulated original image in (f), and the experiment must therefore be regarded as successful. This motivated taking the step to simulation in three dimensions.

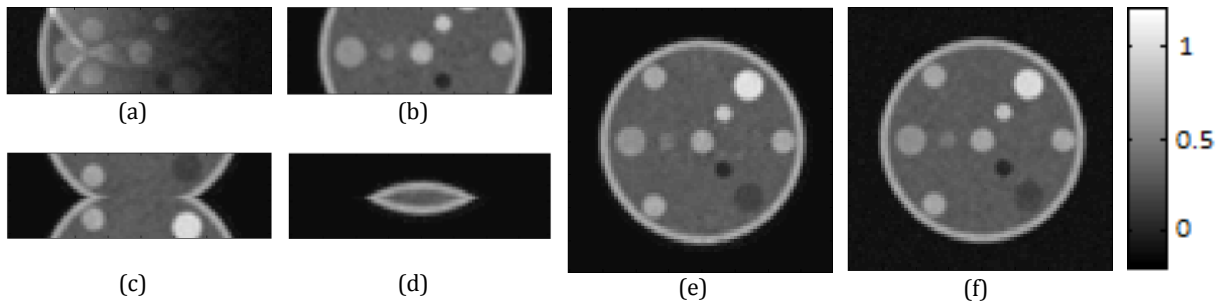


Figure 23. (a) Folded image from one of the surface coils. (b-c) Unfolded parts of the original image. (e) Reconstructed image. (f) Original image (generated separately with reduction factor 1).

4.2 3D implementation of SENSE

The next step was to write a script that reconstructs simulated 3D volumes using the same radial sampling pattern as PRESTO-CAN, with SENSE included. This was done by combining the previous 2D Cartesian script with another script previously developed in the PRESTO-CAN project that reconstructs images of 2D phantoms sampled radially. The way these images are reconstructed is identical to how PRESTO-CAN works in the xz -plane. In other words, the new script basically adds the third dimension where SENSE is performed (the Cartesian sampled y -direction) to a script representing a 2D version of the PRESTO-CAN method.

4.2.1 Simulation of Coils

Like in the previous script, phantoms were generated in k -space, only this time they were composed of 3D ellipsoids rather than ellipses. These ellipsoids were generated using the same coordinate system used when sampling k -space with PRESTO-CAN, that is, radially in the xz -plane and Cartesian in the y -direction. The coil sensitivity was simulated using sine and cosine functions similarly to the 2D case according to (40). The sensitivities did not vary in the z -direction. In order to more clearly test the script's ability to reconstruct SENSE, a 3D phantom somewhat resembling the one used in the 2D simulation was created, of spherical shape with an outer bound of higher intensity and four elongated ellipsoids of differing intensities extending in the z -direction. Some Gaussian noise was also added during the generation of the phantom.

4.2.2 Simulation of Phantom

The 3D phantom was generated using three coordinate matrices resembling the radial sample pattern. The result is for every row in the y -direction a collection of angle profiles, sampled with the golden ratio that is characteristic for PRESTO-CAN, as explained in Section 3.2.2. The number of samples in the radial direction, N_r , was set to 160, which corresponds to oversampling by a factor of 2 since $N_{r,min} = \frac{1}{FOV_x} = 80$. The number of samples in the angular direction, N_ϕ , can be set to an arbitrary prime number, but in order for the sample theorem to be fulfilled, $N_\phi \geq \frac{\pi}{2} N_{r,min}$, i.e. $N_\phi \geq 127$. As explained in section 3.2.2, some under-sampling can be accepted, and it turns out that in most cases it is enough to let the number of angular samples be approximately the same as $N_{r,min}$, i.e. 80. In this implementation, however, N_ϕ was set to 257 in order to rule out all possibilities of lost image quality due to undersampling (albeit it would have been enough if $N_\phi \geq 127$).

4.2.3 Image Reconstruction

To perform the 3D inverse Fast Fourier transform, the volume must be converted to a Cartesian sample pattern (cf. Section 3.2.3). This is done using a function that performs data driven 2D Cartesian interpolation using a Kaiser-Bessel filter in all the rows in the y -direction. In order to get rid of sharp edges that can give rise to artifacts after the inverse Fourier transformation, the volume was low pass filtered using a cosine shaped weighting function. Then, the inverse 3D Fourier transform was performed. The resulting spatial volume has much higher values in the center than at the borders, an effect that comes from pre-weighting performed as part of the Cartesian interpolation. This was countered by dividing the volume with a corresponding 3D weighting function. The resulting Cartesian sampled volume had a resolution of 160×160 in the xz -plane, which has been oversampled by a factor of 2 in both directions in order for the gridding algorithm used for the Cartesian interpolation to work. The resolution in the y -direction was 80. The oversampled xz -plane was finally cropped so that the resolution of the resulting volume became $80 \times 80 \times 80$.

4.2.4 Sensitivity Map Refinement

In this way, we get a set of nine 3D phantoms exactly as in the 2D case, with one resembling the homogenous volume from the body coil and eight resembling the separate volumes from the surface coils with varying sensitivity, and we can calculate 3D sensitivity maps. Refining these with normalized convolution is possible to do row-by-row, using the same 2D basis functions as before, but the result is of course much better if true 3D implementation of normalized convolution is used. In order to do this, 3D basis functions are needed, i.e. the set of second degree polynomials used is expanded to $\{1, x, y, z, x^2, y^2, z^2, xy, xz, yz\}$. These are however a little tedious to plot in 2D.

4.2.5 Results

The procedure of creating the eight SENSE reduced phantoms is exactly the same, and the algorithm for SENSE reconstruction is basically the same as the one used in the 2D case, with the only difference that we have to loop over all the rows in the z (or x) direction. The different steps in the reconstruction procedure are shown in Figure 24. Some artificial noise was added to the original phantom, which has been amplified somewhat in the folded image (Figure 24 (f)). As explained in section 3.3.3, this is unavoidable. As a complement to this experiment, another one without added noise and with an identical phantom used for constructing the sensitivity maps as the one to be reconstructed, i.e. without any “hole” of intensity 0.

The results are shown in Figure 25. The output in Figure 25 (f) should be identical to Figure 25 (a), but we can see that it contains some edge artifacts due to that the refined sensitivity map is not extrapolated enough. Further extrapolation is however hard to do since the sharp jump between the high intensity edge of the phantom and the low intensity background causes horizontal streaks in the raw sensitivity map (see Figure 24 (c)). These edge artifacts are actually reduced when a moderate noise level is added (compare Figure 25 (c) with Figure 24 (c)). Over all, the results in these experiments were however deemed to be good enough, showing that the principle of the implemented method works, and this motivated the move on to using real data.

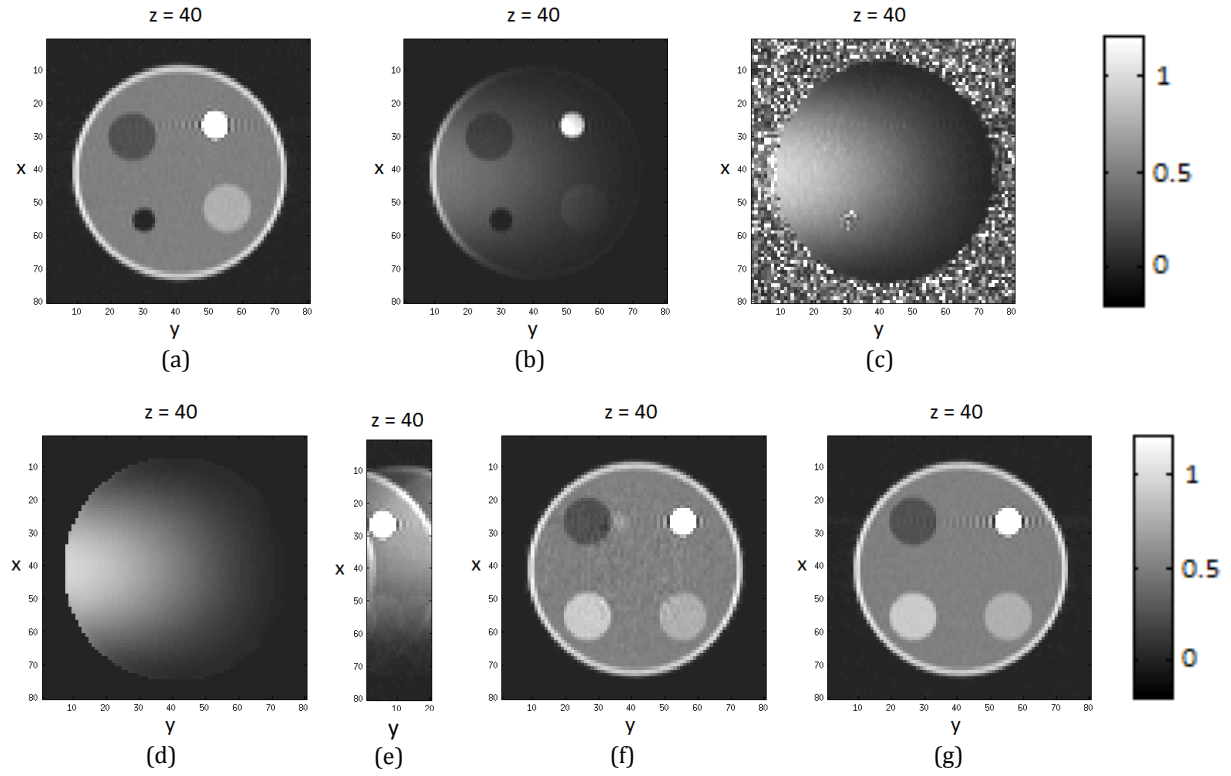


Figure 24. Simulated SENSE reconstruction in 3D with radial sample pattern. (a) Surface coil volume of the phantom used to calculate the sensitivity maps. It includes an ellipsoid of value 0 in order to test the algorithm's ability to fill out holes in the raw sensitivity map. (b) Volume from one of the surface coils. (c) Raw sensitivity map. (d) Refined sensitivity map after normalized convolution and masking. (e) Volume folded in the y -direction from one of the surface coils after SENSE reduction with a reduction factor of 4. (f) Reconstructed phantom. (g) The phantom used for SENSE reconstruction for comparison. One slice of the volume in the z -direction is shown.

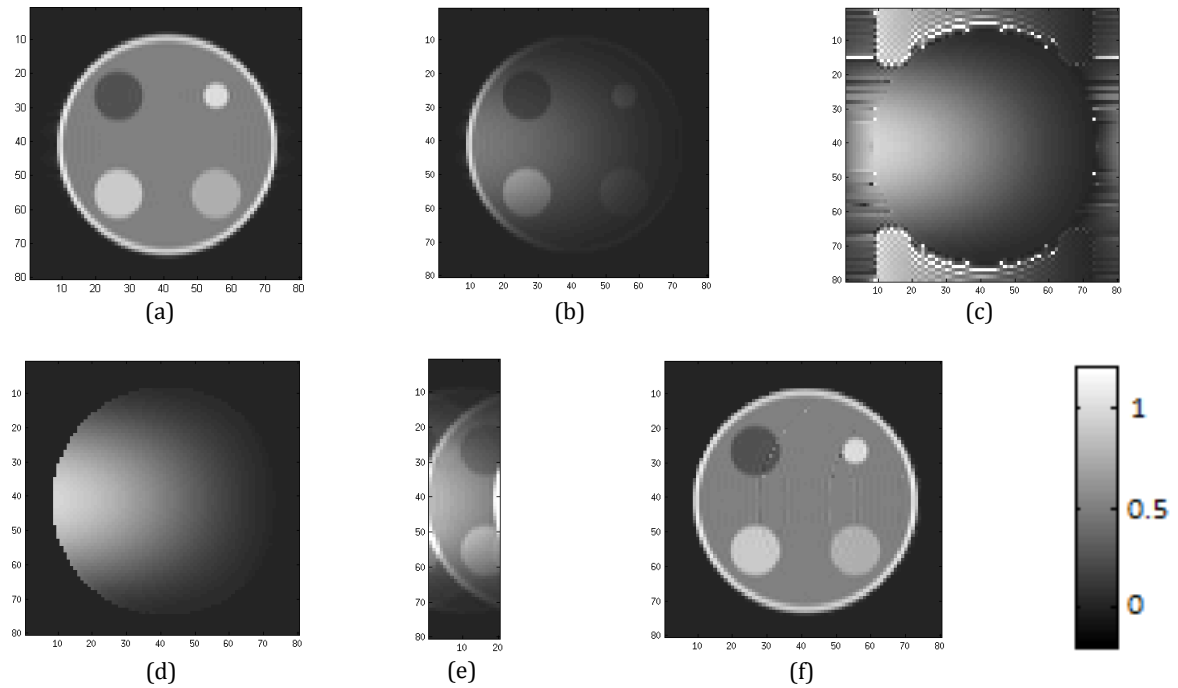


Figure 25. Similar as the previous experiment but without added noise. (a) Surface coil volume of the phantom used to calculate the sensitivity maps. (b) Volume from one of the surface coils. (c) Raw sensitivity map. (d) Refined sensitivity map after normalized convolution and masking. (e) Volume folded in the y -direction from one of the surface coils after SENSE reduction with a reduction factor of 4. (f) Reconstructed phantom, which contains some edge artifacts as compared to (a). One slice of the volume in the z -direction is shown.

4.3 3D Implementation of SENSE, Real Data Acquired With PRESTO-CART

Before moving on to testing the algorithm on real PRESTO-CAN data, it was seen as natural to first develop a script that reconstructs MR images acquired with an ordinary Cartesian sampled PRESTO sequence, here called PRESTO-CART in order to clearly distinguish it from PRESTO-CAN. The advantage with this is that we can compare the results with the MR-scanner's own reconstruction of both fully sampled volumes as well as volumes sampled more sparsely with SENSE reduction and see if we can come up with comparably good results. That would be a prerequisite for being able to reconstruct images sampled with the PRESTO-CAN sequence. This makes it possible to differ between problems that arise in our results because of difficulties with reconstructing images acquired with PRESTO-CAN – especially with SENSE reduction – and our ability (or lack thereof) to reconstruct even ordinary Cartesian sampled data.

Image volumes were acquired with PRESTO-CART using a phantom consisting of a bottle filled with a water solution. Acquisition of in vivo image volumes of a human brain was also conducted, but unfortunately none of the fully sampled images from surface coil 2-8 was able to be retrieved correctly from the MR-scanner, making it impossible to create our own sensitivity maps: Because of this, in vivo images are not considered in this implementation step. The image volumes were acquired in two different ways. First, an ordinary homogenous image acquired by interconnecting the eight head surface coils with each other using a quadrature method (cf. Section 3.1.6). Secondly, eight separate images from the respective surface coils, either with a reduction rate of 1 (i.e. no reduction), 2 or 4. The sensitivity maps were calculated by dividing the eight separate coil images acquired with full sample rate with the quadrature image or a sum-of-squares image of the separate coil images, as explained in Section 3.3.4.

The main thing that had to be changed from the script for radial 3D data was to replace the generation of the phantom including the interpolation to a Cartesian grid with a previously developed script that reads the real volume data from a file, as well as performing forward-and-back correction as explained in Section 3.2.3. It turned out that the way the folding of the images when SENSE reduction was done by the MR-scanner itself either with reduction rate 2 or 4, was “from one side” rather than “from both sides” that was the case when k -space rows are deleted manually (cf. Section 3.3.2). Since the exact k -space resolution of the image vary somewhat depending on what EPI factors are used, it was necessary to manually investigate for each case which rows of the original image are superimposed on which in the folded image. This was done by carefully examining the folded images with an unfolded. The k_y -resolution of the folded image with reduction rate 4 was in this case 21 rows, and for the unfolded image 80. It turned out that the 80 rows of the unfolded image was superimposed on the 21 rows of the folded images according to Table 3. The reconstruction algorithm was modified accordingly, and the results can be seen in Figure 26 and Figure 27.

Rows of original image	Rows of folded image
1-14	8-21
15-36	1-21
37-58	1-21
59-80	1-21

Table 3. Example of how the folding is done when 80 rows are reduced to 21.

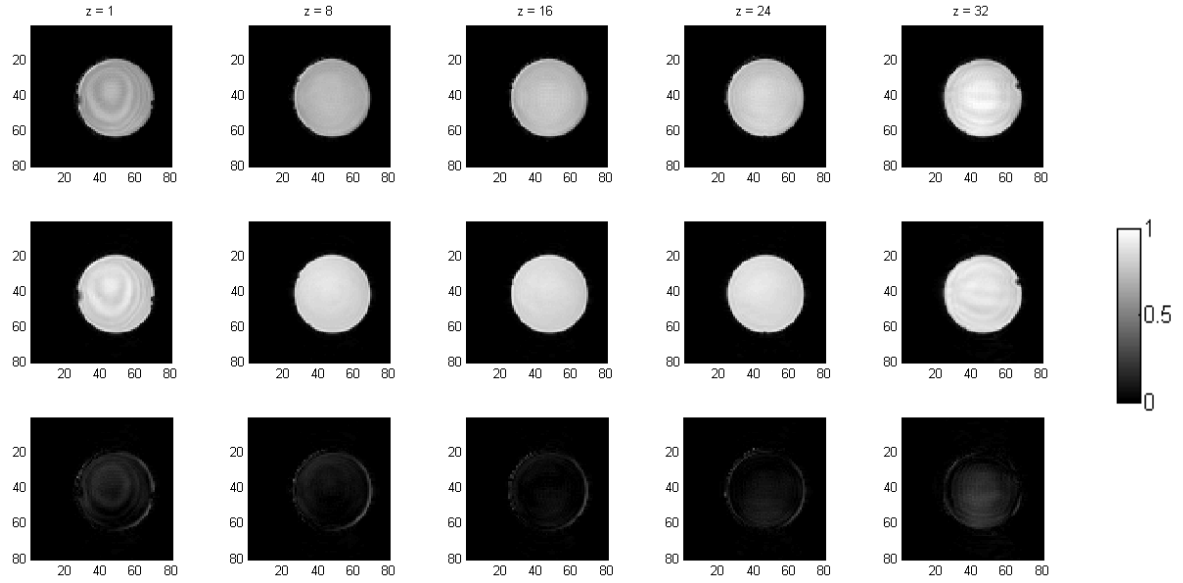


Figure 26. Result of SENSE reconstruction of real in vitro PRESTO-CART data, reduction rate 2. The upper row shows the outcome from the developed algorithm, the middle row shows the reconstruction made by the MR-scanner itself and the lower row shows the differences between the two. 5 slices in the (kx, ky) -plane of an $80 \times 80 \times 32$ sized volume are shown.

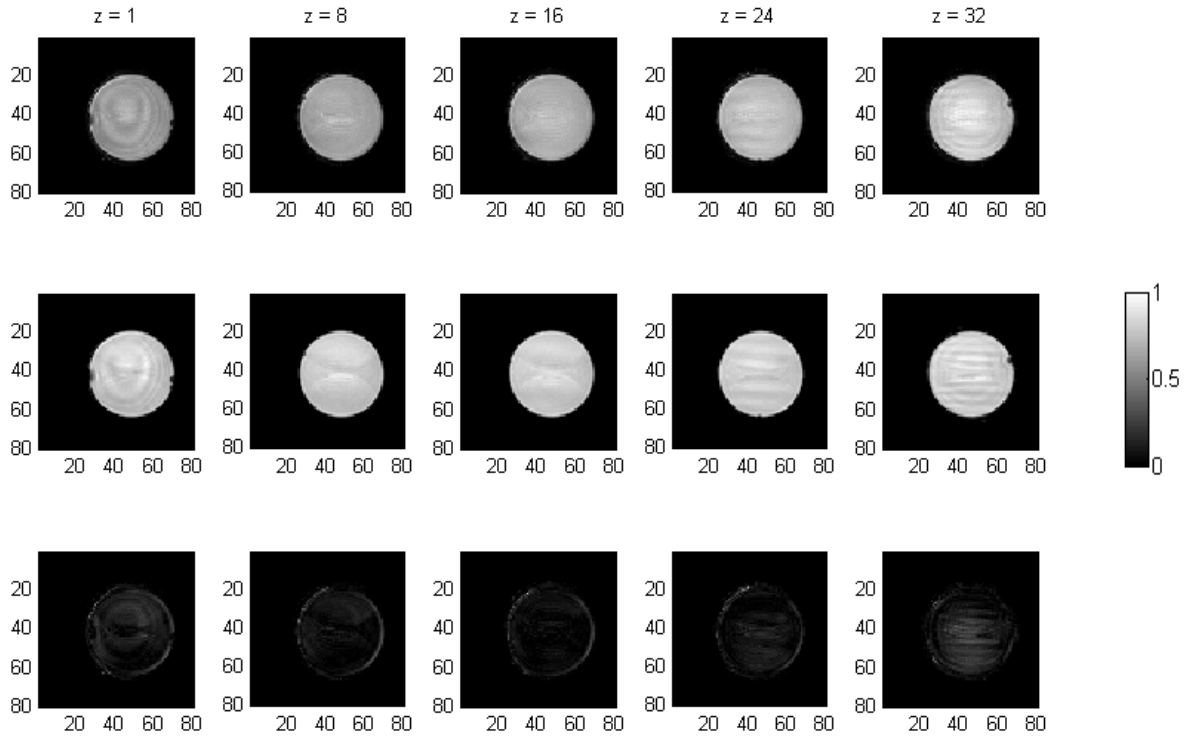


Figure 27. Same as the previous figure, but with reduction rate 4.

The small differences that still can be seen could possibly be decreased even further by normalizing the images in another manner, but overall the resulting images from the reconstructions made by the developed algorithm were deemed to be close enough to those made by the MR-scanner itself. Note that even the SENSE reconstruction made by the MR-scanner itself with reduction rate 4 contain clearly visible edge artifacts (it is possible to see remnants of where the edges of the original image was superimposed on the middle part due to the aliasing).

4.4 3D Implementation of SENSE, Real Data Acquired With PRESTO-CAN

After having made sure that our algorithm for reconstructing SENSE reduced images acquired by the MR-scanner itself using a Cartesian grid works sufficiently well, it was finally possible to move on to working with real data acquired by the PRESTO-CAN method. Two different types of reconstruction experiments were conducted. First, reconstruction of images sampled with reduction rate 2 and 4, and secondly, reconstruction of data with other SENSE factors by manually removing a number of k -space rows before the final inverse Fourier transform. However, since k -space has to be sampled evenly, only reduction factors of integer values could be used.

Scans were performed with different multishot and EPI factors, but in the analysis only the scans with the best quality was used, namely with EPI = 3. Since the resolution in k -space is supposed to be as close as possible to 80 rows, this corresponds to multishot = 26, which gives $26 * 3 = 78$ rows. The forward-and-back correction, performed in order to compensate in data changes based on which direction it has been sampled in as described in Section 3.2.3.1, had to be adjusted in order to work together with SENSE. In order to perform forward-and-back correction, we need to know which k -space rows have been sampled in the same direction and then compensate accordingly. With multishot = 26 and EPI = 3, only the central 26 rows (27-52) are unshifted and do not have to be corrected. When applying SENSE, however, the number of rows is decreased and accordingly also the number of rows that have to be corrected. With SENSE reduction factor 2, we get multishot = 14 and 42 rows, which means that rows 15-28 do not have to be corrected. Similarly, with reduction factor 4 and multishot = 7 giving a resolution of 21 rows, row 8-14 do not have to be corrected. Information about which order the rows of k -space are scanned is contained in the .list file that accompanies each MR scan. One might consider writing an algorithm that automatically calculates which rows that has to be corrected given a specific EPI factor and SENSE reduction factor, but this has not been included in the implementation. Instead, for each combination the correct rows had to be entered specifically in the script.

Following is a step-by-step description on how SENSE was implemented on MR volumes acquired with the PRESTO-CAN method. More images of the resulting sensitivity maps and SENSE reconstructed image volumes are presented in Appendix A and B.

4.4.1 Acquisition of Quadrature Image and Surface Coil Images

Data without SENSE reduction was recorded in order to create the sensitivity maps. Both a homogenous quadrature image volume (Figure 28) as well as image volumes from the 8 different surface receiver coils with varying sensitivity (Figure 29) was acquired, as explained in section 3.1.6. The forward-and-back correction, correction of the rotation-angle position and phase-drift corrections were calculated based on separate reference scans with $k_y = 0$. The full quality scans were then reconstructed to the image domain according to the procedure explained in Section 3.2.3. The phase-drift correction was applied individually to the 9 different volumes, based on the correction vectors calculated from their respective reference scans.

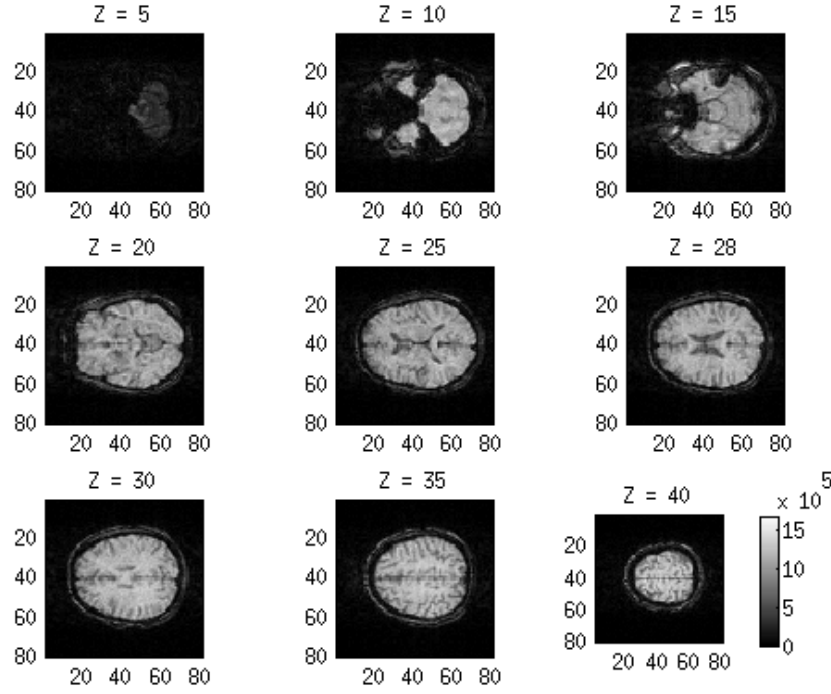


Figure 28. Magnitude of a homogenous quadrature image volume retrieved with PRESTO-CAN, used as reference when calculating the sensitivity maps. Different slices of the (k_x, k_y) -plane are shown.

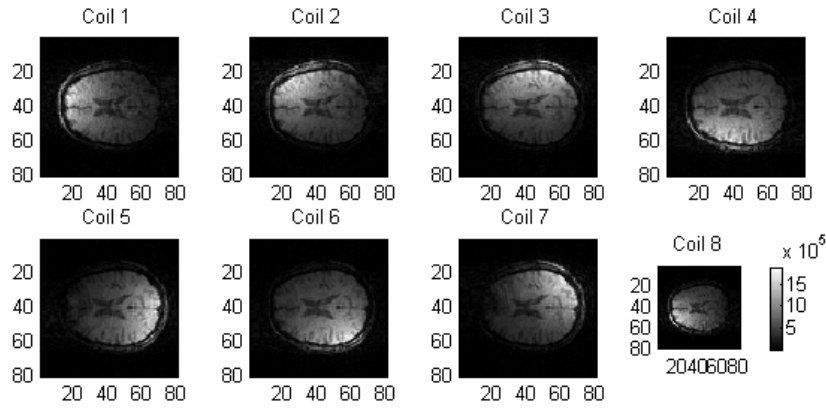


Figure 29. Images without SENSE reduction from the 8 separate receiver coils with varying sensitivity. One slice from each of the 8 coil volumes are shown.

4.4.2 Calculation of Raw Sensitivity Maps

A sum-of-squares image volume was then calculated from the images from the 8 surface receiver coils according to (28) (Figure 30). The raw sensitivity maps were calculated by dividing the image volumes from the surface coils with the quadrature image volume and the sum-of-squares image volume (Figure 31 and Figure 32).

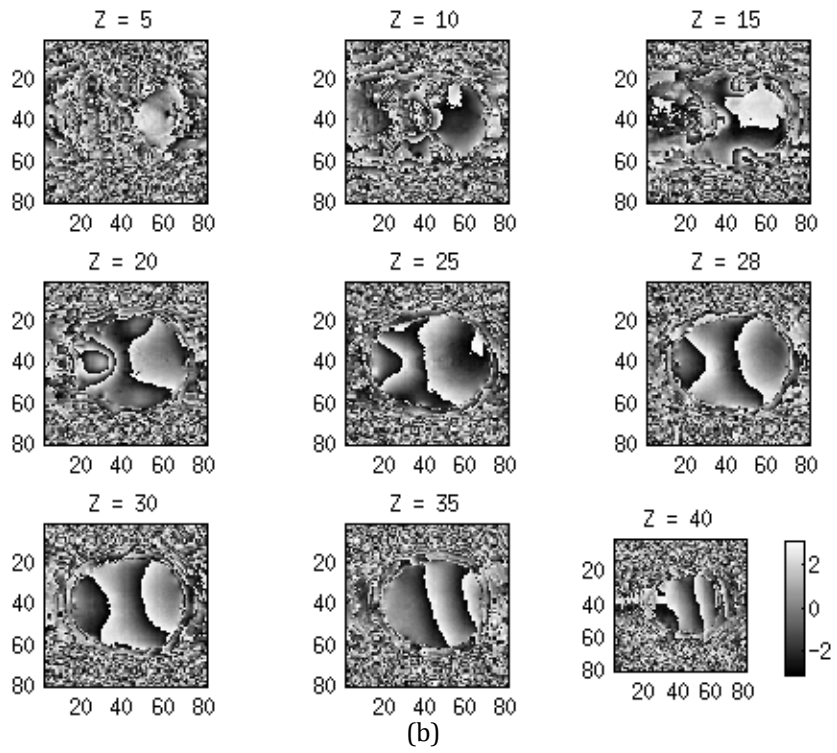
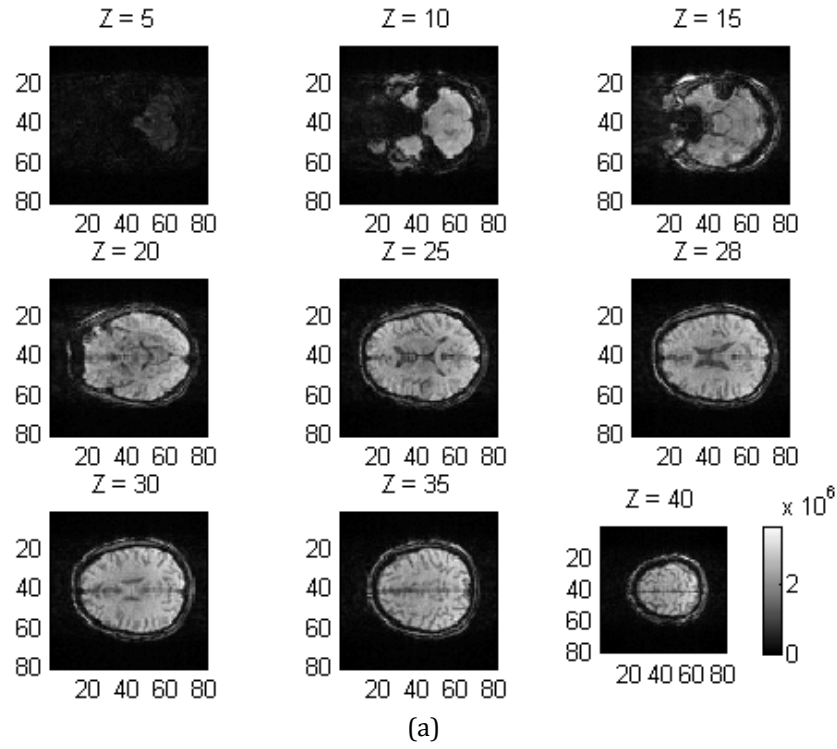


Figure 30. (a) Magnitude and (b) phase of a sum-of-squares image volume, calculated from the 8 separate sensitivity coils, used as reference as an alternative to the quadrature image volume when calculating the sensitivity maps.

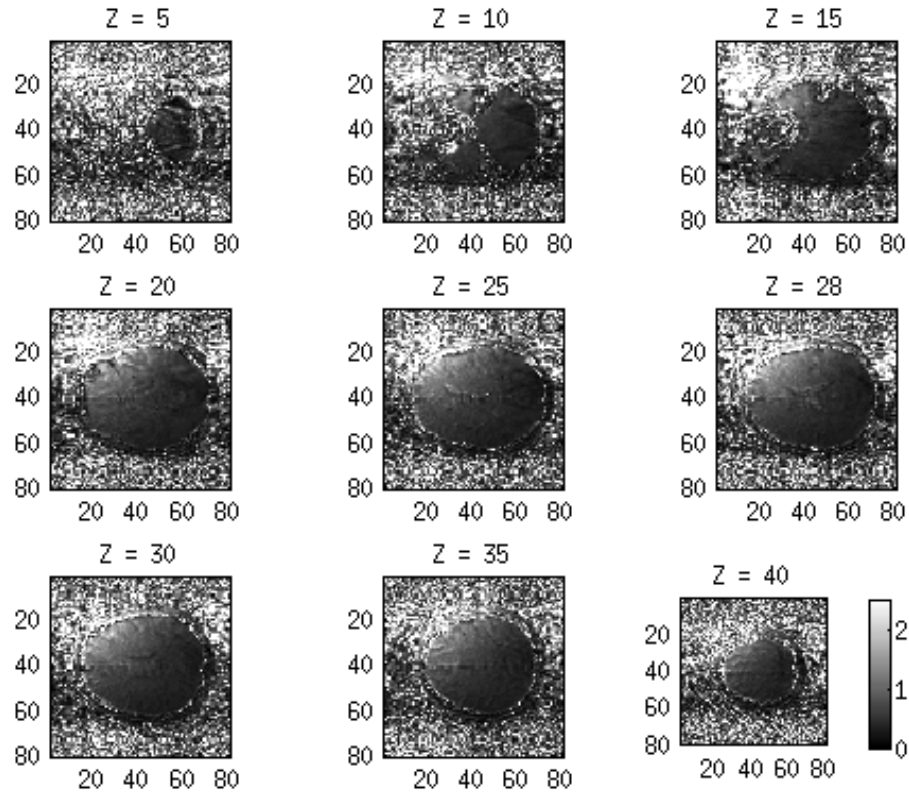


Figure 31. Raw sensitivity map for receiver coil 2 calculated by division with a quadrature image volume.

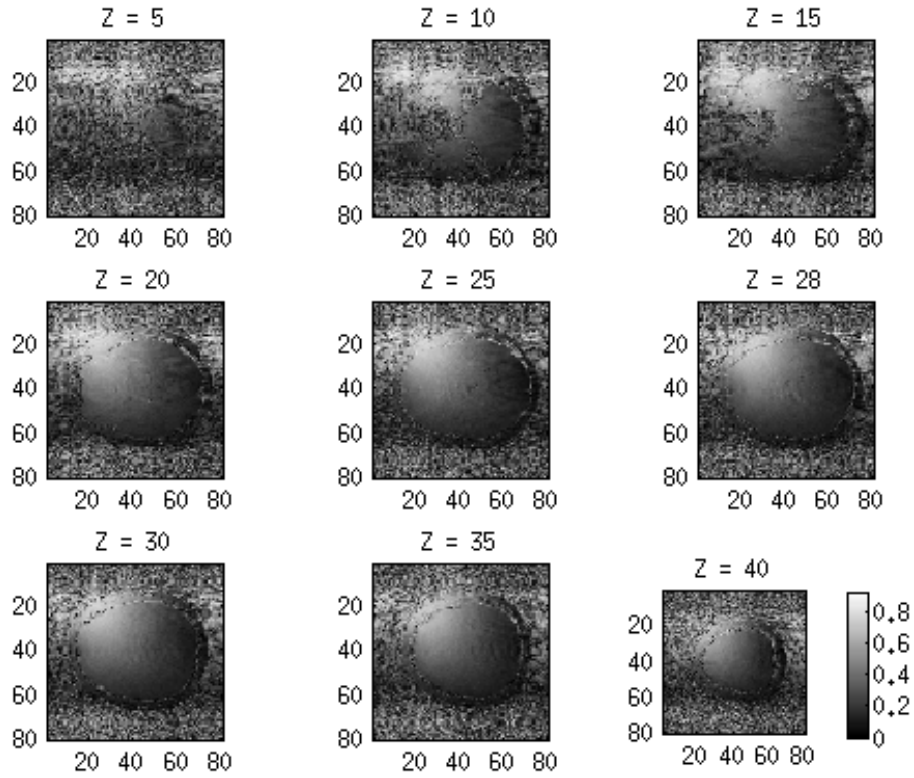


Figure 32. Raw sensitivity map for receiver coil 2 calculated by division with a sum-of-squares image volume.

4.4.3 Refinement of Sensitivity Maps Using Normalized Convolution

The raw sensitivity maps calculated with the two respective methods were then refined using normalized convolution. The certainty function was created by making a threshold at 5% of the maximum value of the sum-of-squares image (see Figure 33). As applicability function, Gaussian kernels of different size and standard deviations were used, like the ones shown in Figure 39. The resulting sensitivity maps were also multiplied with a mask that was developed by erosion and dilation of the certainty map in order to replace noisy and unreliable values at the outer parts of the sensitivity map (and accordingly, the final output as well) with 0 (Figure 34). The resulting sensitivity maps are shown in Figure 35 and Figure 36.

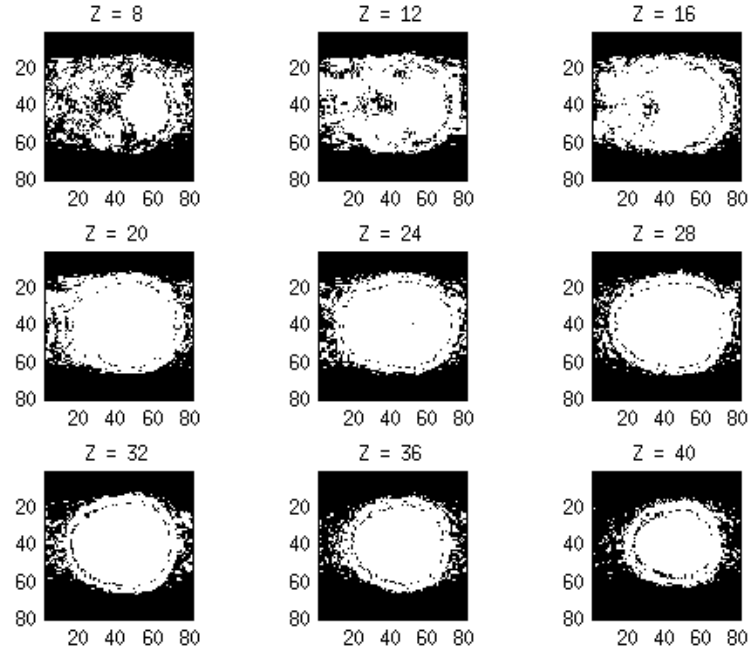


Figure 33. Certainty function used as input for the normalized convolution of the raw sensitivity maps.

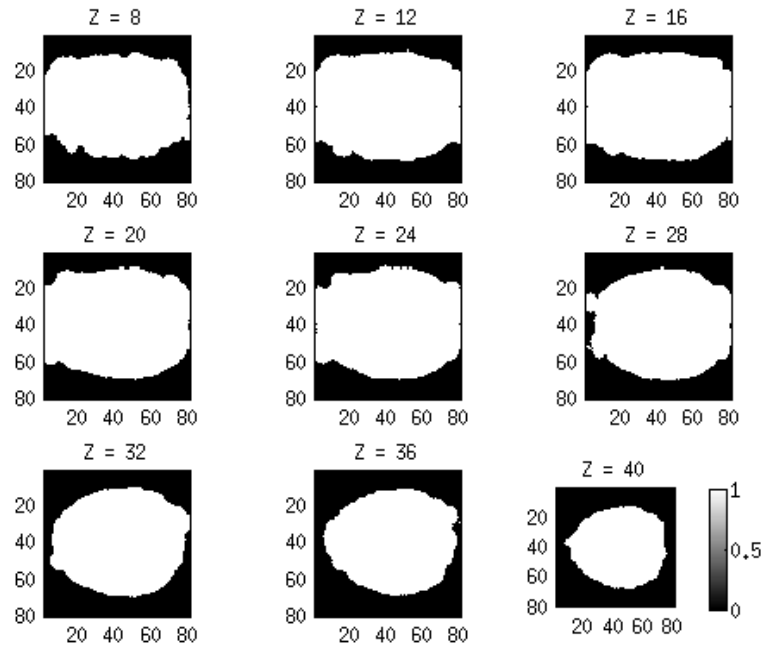


Figure 34. Mask multiplied with the sensitivity maps in order to replace unreliable values with 0.

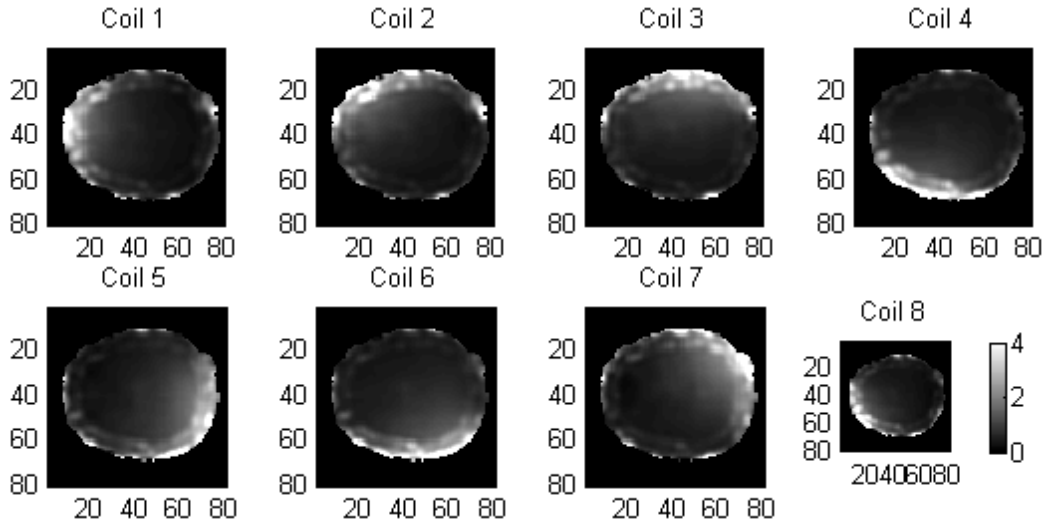


Figure 35. Sensitivity maps for the 8 receiver coils calculated from a quadrature image refined with normalized convolution. One slice in the (kx,ky) -plane from the sensitivity map of each coil is shown.

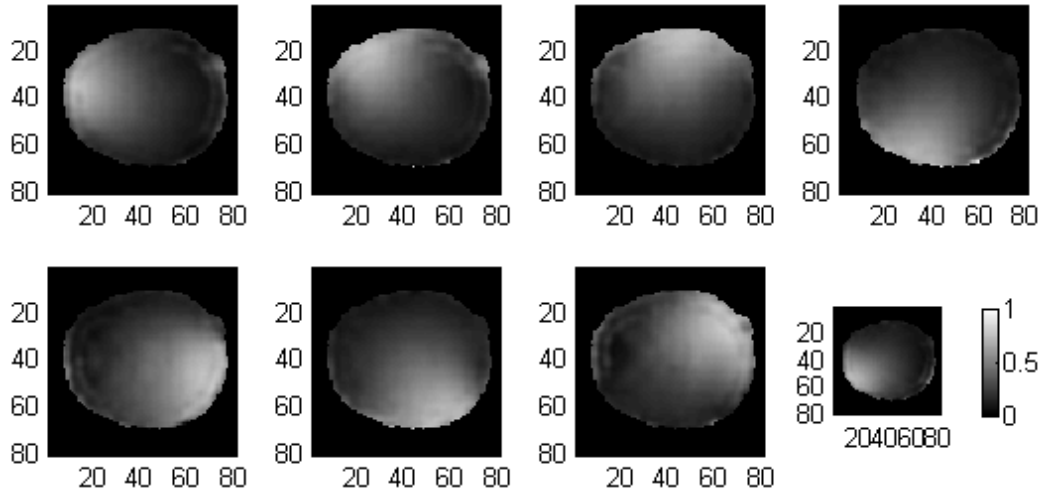


Figure 36. Sensitivity maps for the 8 receiver coils calculated from the sum-of-squares image refined with normalized convolution. One slice in the (kx,ky) -plane from the sensitivity map of each coil is shown.

4.4.4 Acquisition of SENSE Reduced Data

In order to simulate SENSE reduction, k -space rows were deleted from fully sampled surface coil images just before the inverse Fourier transformation. This results in images folded “from both sides”, and an example with reduction rate 5 can be seen in Figure 37.

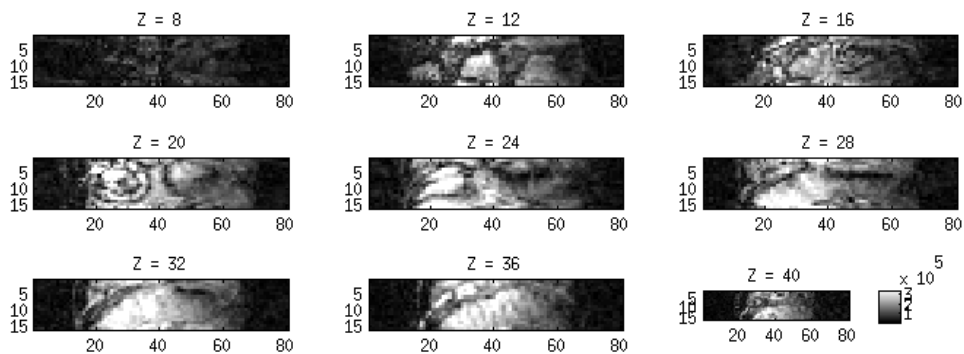


Figure 37. Folded image volume with reduction rate 5.

Data with reduction rate 2 and 4 were also recorded directly with the MR-scanner and reconstructed with the PRESTO-CAN method. Which rows to be corrected with the forward-and-back correction was decided on according to the explanation given in Section 4.4. An example of one of these folded image volumes is shown in Figure 38.

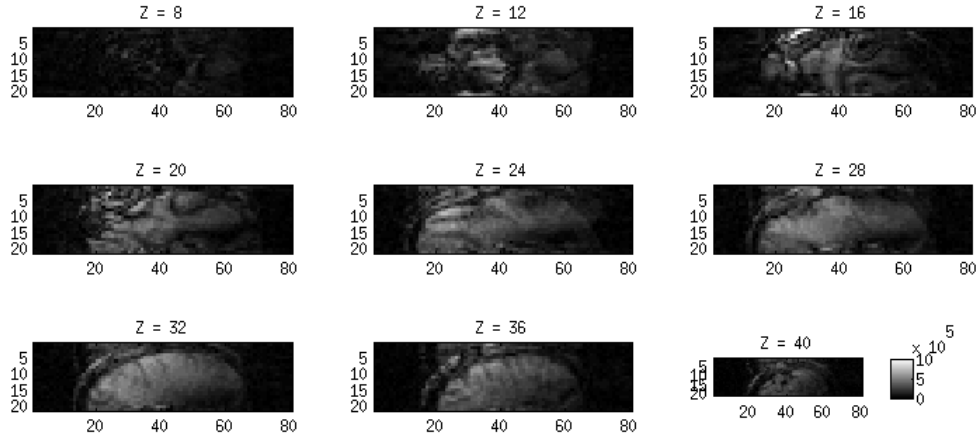


Figure 38. Folded image volume with SENSE reduction rate 4.

4.4.5 SENSE Reconstruction

Finally, the SENSE reconstruction algorithm was performed in order to unfold the images. Since the SENSE reduced images from the MR-scanner has been folded “from one side”, we get an equation system according to (19) which is solved using (26). The exact way this reconstruction algorithm is written depends on which SENSE reduction factors and EPI factors are used. For example, with EPI = 3 and multishot = 26 with SENSE reduction 4 as was initially used during the evaluation of this algorithm, the number of rows of the fully sampled k -space was 84 and consequently of the folded image $84/4 = 21$. With these settings, the 80 rows of the original image are superimposed on the 21 rows of the folded image according to Table 4 (compare this with Table 3 in section 4.3). The algorithm has to be adjusted accordingly.

Rows of original image	Rows of folded image
1-17	5-21
18-38	1-21
39-59	1-21
60-80	1-21

Table 4. Example of how the folding is done in an image with EPI = 3 and reduction rate $R = 4$, where 80 rows are reduced to 21.

4.4.6 Adjustable Parameters

In the experiments conducted in order to evaluate the implementation, different combinations of adjustable parameters were used in order to find the best possible result. Here follows a summary of the most important of these and how they can be adjusted

4.4.6.1 Way of Determining the Raw Sensitivity Maps

In calculating the raw sensitivity maps, the respective surface coil images can either be divided with a quadrature image (body coil image) or a sum-of-squares image, as explained in section 3.3.4.

4.4.6.2 Normalized Convolution of the Phase

The normalized convolution can either be applied directly on the complex raw sensitivity maps, on the magnitude only with the unaltered phase restored afterwards, or separately on the magnitude and the phase, with another (smaller) applicability function used when applied on the phase, as described in section 3.3.4.8.

4.4.6.3 Applicability Function

As applicability function for the normalized convolution, a Gaussian kernel is usually chosen. Both the size and the standard deviation of this can be adjusted. It was found that raw sensitivity maps determined by division with the quadrature image needed a larger applicability function since they were noisier. A good standard deviation was found to be 2, with an accompanying applicability function size of $7 \times 7 \times 7$ or $9 \times 9 \times 9$ voxels. For sensitivity maps based on the sum-of-squares image, the difference between using a sigma of 1 or 2 was not very significant. However, when applying normalized convolution on phase images, a smaller sigma of 1 with applicability function size $5 \times 5 \times 5$ voxels was chosen in order not to cause cancelling of values in regions containing voxels of strongly varying values.

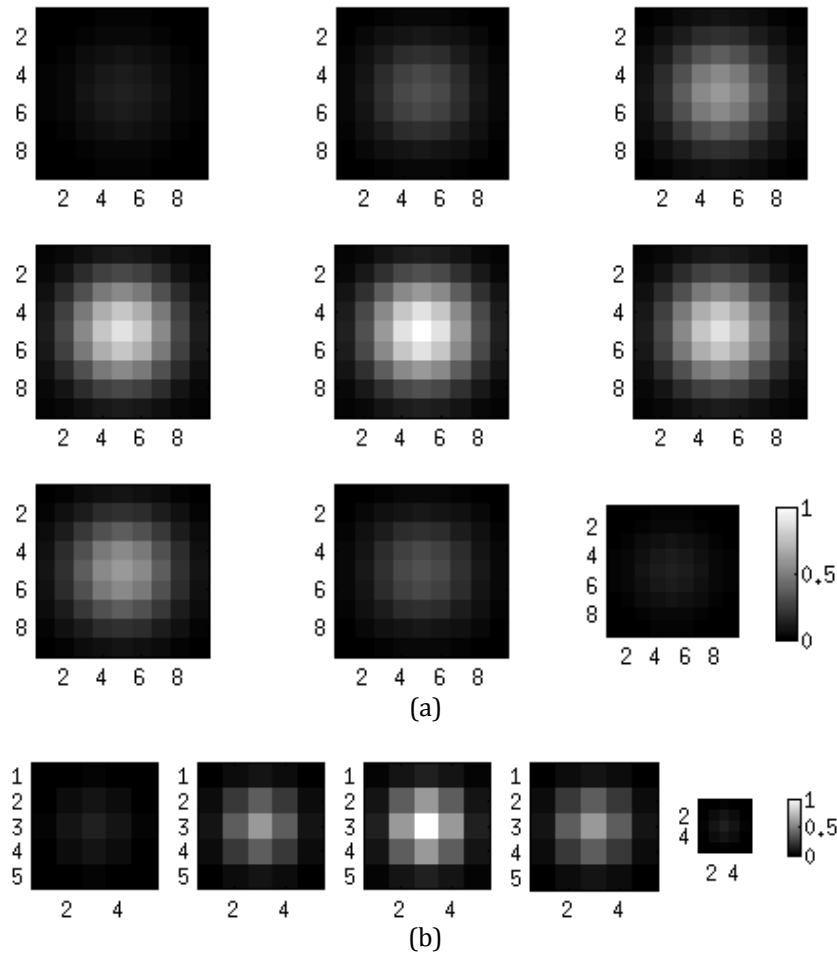


Figure 39. Applicability functions with (a) size $9 \times 9 \times 9$ voxels and standard deviation $\sigma = 2$ and (b) size $5 \times 5 \times 5$ voxels and standard deviation $\sigma = 1$.

4.4.6.4 Certainty Function

The certainty function for the normalized convolution is usually calculated by putting a threshold on the quadrature image (body coil image) or the sum-of-squares image. A good threshold level was found to be 5% of the maximum value of the sum-of-squares image. The result of this can be seen in Figure 33. The sum-of-squares image was chosen as basis for calculating the threshold since outlier values are averaged out, while the maximum value of the quadrature image can consist of an extremely high outlier.

4.4.6.5 Regularization

The possibility to include matrix regularization (as described in section 3.3.3) was also implemented. However, with the low-resolution images used in this implementation, no significant improvement in noise reduction could be measured even with a λ value as high as 10^{-1} , and with even larger values the unfolding was negatively affected. Therefore the same value of $\lambda = 10^{-3}$ originally recommended in [28] was used throughout.

5 Results

5.1 Sensitivity Maps

In this experiment, images with SENSE reduction factor 4 recorded by the MR-scanner was reconstructed using sensitivity maps that were created using different parameters. Images of such folded volume from one surface coil can be seen in Figure 38. Five different sensitivity maps were evaluated, three based on division by a quadrature image and two based on division by a sum-of-squares image. They are henceforth referred to as sensitivity maps A – E. The settings were as follows:

A – Raw sensitivity map calculated by division with quadrature image, normalized convolution applied on magnitude and phase together (see Section 3.3.4.8), applicability function size = $9 \times 9 \times 9$ voxels, standard deviation = 2.

B – Raw sensitivity map calculated by division with quadrature image, normalized convolution applied on magnitude only, applicability function size = $7 \times 7 \times 7$ voxels, standard deviation = 2.

C – Raw sensitivity map calculated by division with quadrature image, normalized convolution applied on magnitude and phase separately (see Section 3.3.4.8), applicability function sizes = $7 \times 7 \times 7$ and $5 \times 5 \times 5$ voxels respectively, standard deviations = 2 and 1 respectively.

D – Raw sensitivity map calculated by division with sum-of-squares image, normalized convolution applied on magnitude and phase together only, applicability function size = $7 \times 7 \times 7$ voxels, standard deviation = 2.

E – Raw sensitivity map calculated by division with sum-of-squares image, normalized convolution applied on magnitude only, applicability function size = $7 \times 7 \times 7$ voxels, standard deviation = 2.

Magnitude and phase images of one slice from each of the surface coils of the refined sensitivity maps are shown in Figure 40 and Figure 41. For larger images showing other slices as well as the raw sensitivity maps, see Appendix A.

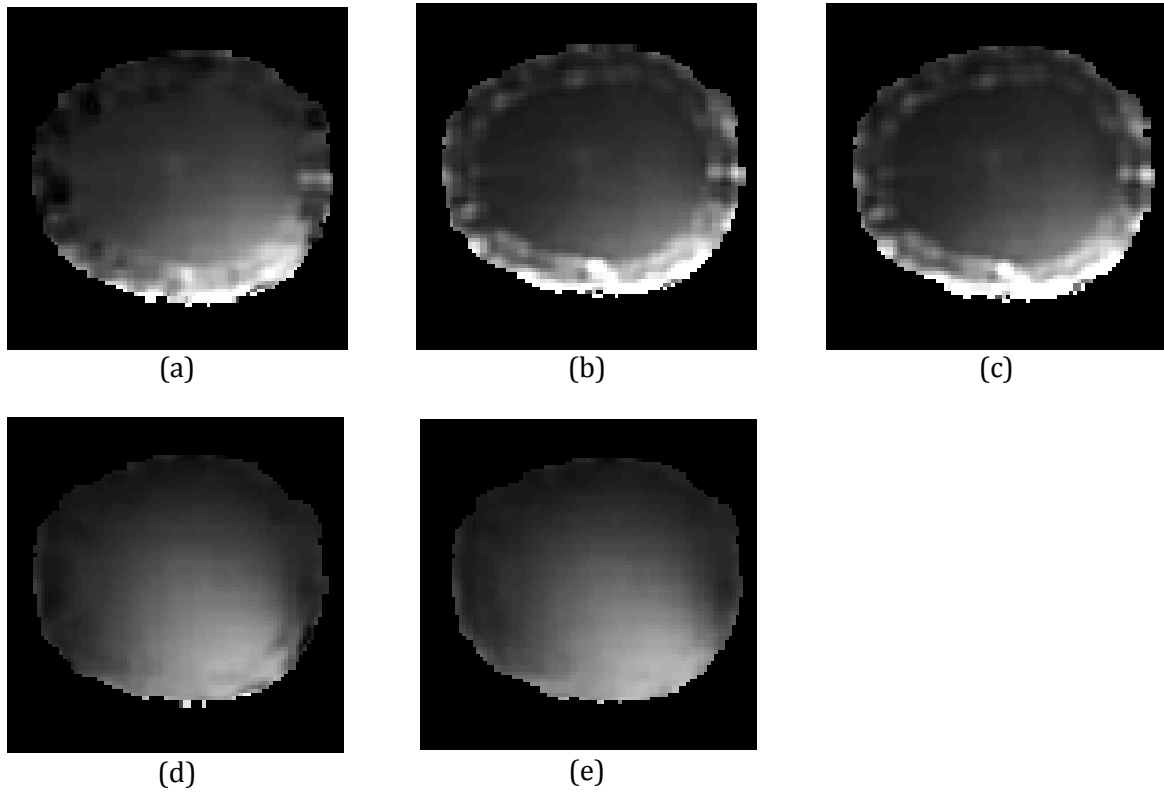


Figure 40. (a)-(e): Magnitude images of one slice from one of the receiver coils for sensitivity maps A-E, respectively.

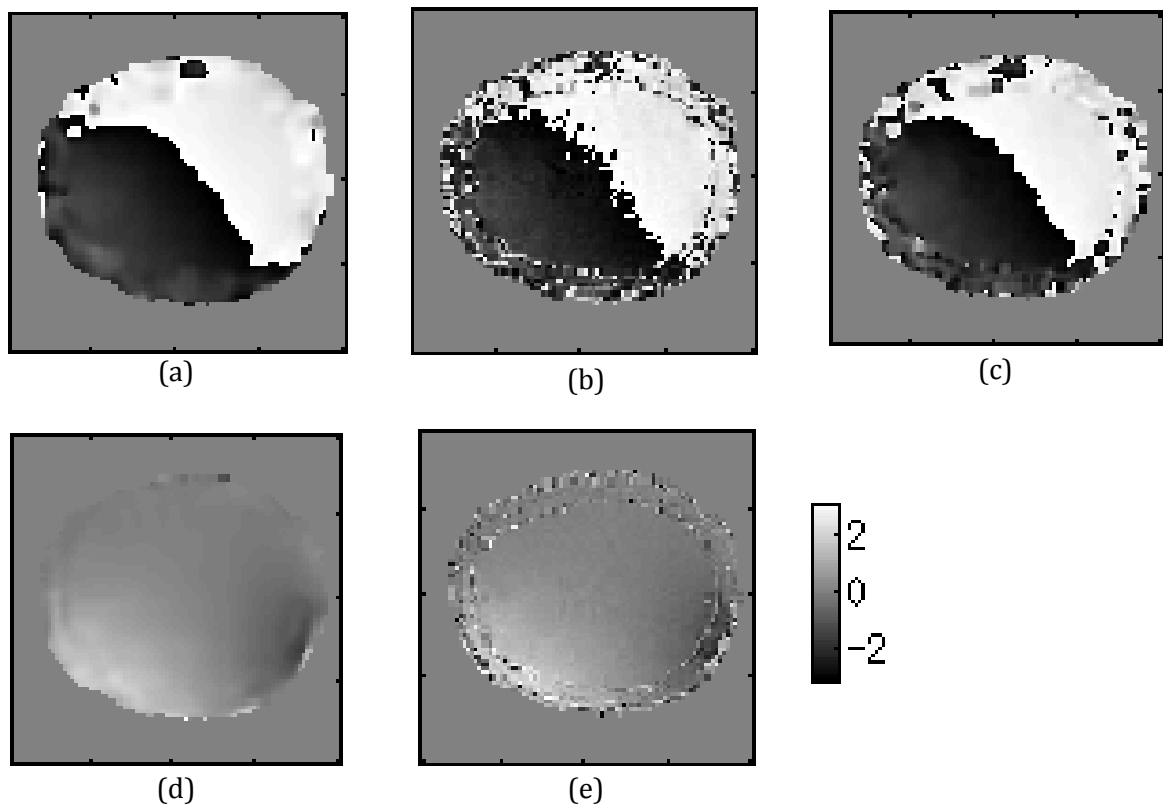


Figure 41. (a)-(e): Phase images of one slice from one of the receiver coils for sensitivity maps A-E, respectively.

5.2 Reconstruction of SENSE Reduction Performed by the MR-Scanner

Figure 42 and Figure 43 shows the results from SENSE reconstruction using each of the five sensitivity maps with reduction rate 2 and 4, respectively. Figures containing more slices as well as the phase are shown in Appendix B. Three images are shown for comparison: a quadrature image recorded with PRESTO-CAN without SENSE reduction, the output from Cartesian sampled data without SENSE reduction and the output from Cartesian sampled data recorded with the same reduction rates (2 and 4 respectively) and reconstructed by the MR-scanner.

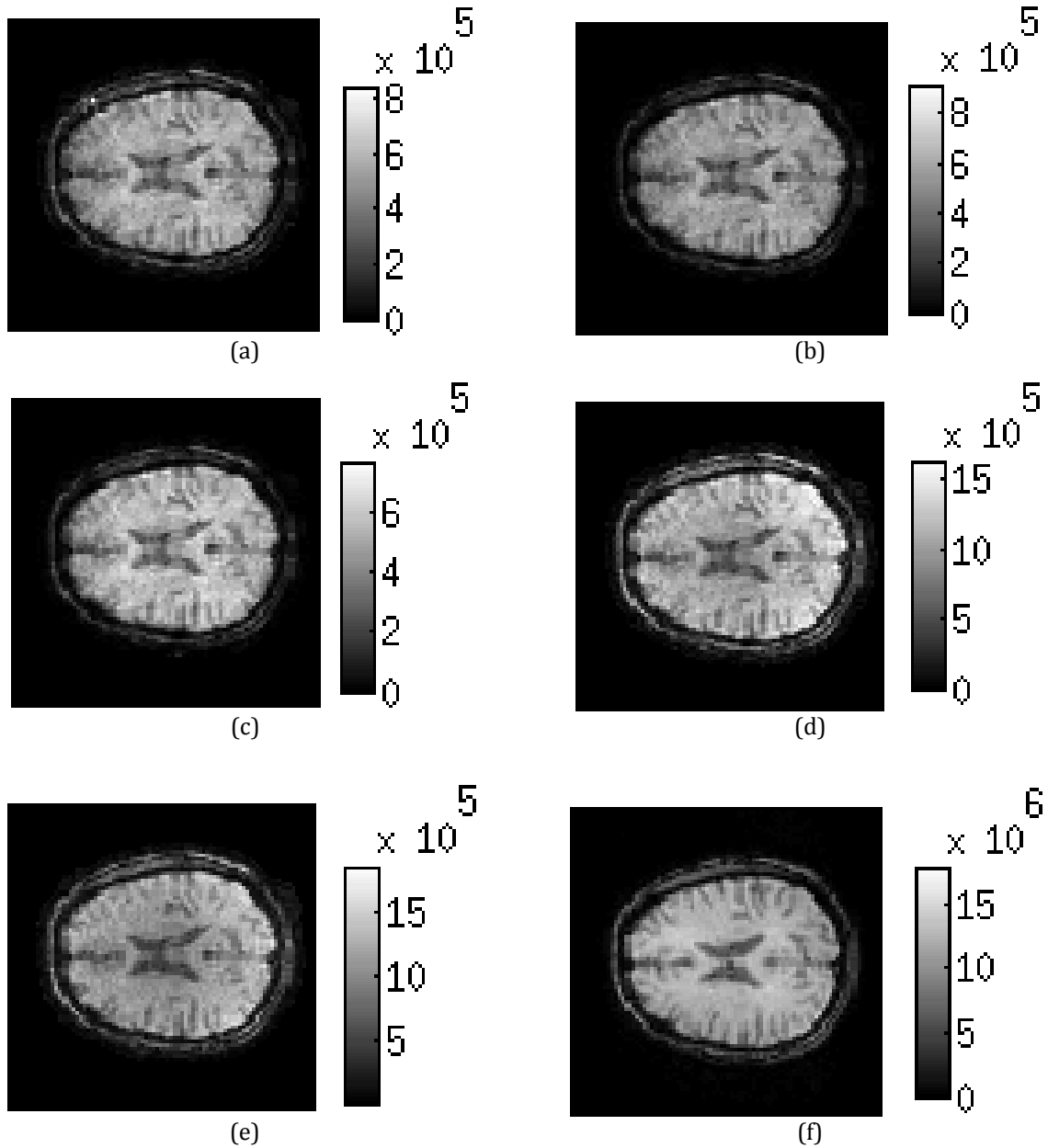


Figure 42. Results of reconstruction of in vivo data sampled with PRESTO-CAN with reduction rate 2.

(a)-(e): Magnitude of the outputs when using sensitivity maps A-E, respectively.

(f): Magnitude of the output from Cartesian sampled data with reduction rate 2 and reconstructed by the MR-scanner.

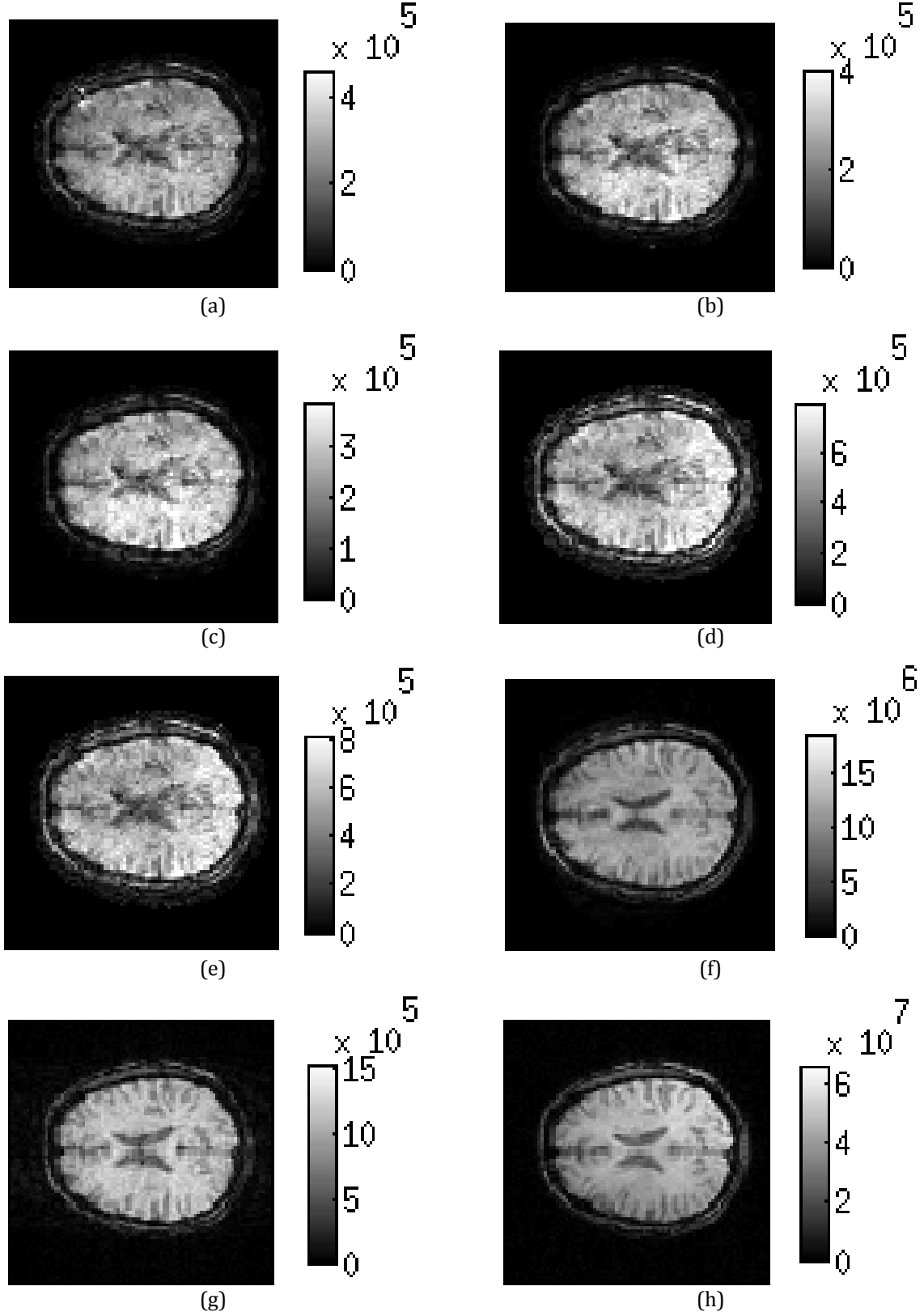


Figure 43. Results of reconstruction of in vivo data sampled with PRESTO-CAN with reduction rate 4.
(a)-(e): Magnitude of the outputs when using sensitivity maps A-E, respectively.
(f): Magnitude of the output from Cartesian sampled data with reduction rate 4 and reconstructed by the MR-scanner.
(g): Magnitude of a quadrature image recorded with PRESTO-CAN without SENSE reduction shown for comparison.
(h): Magnitude of the output from Cartesian sampled data without SENSE reduction shown for comparison.

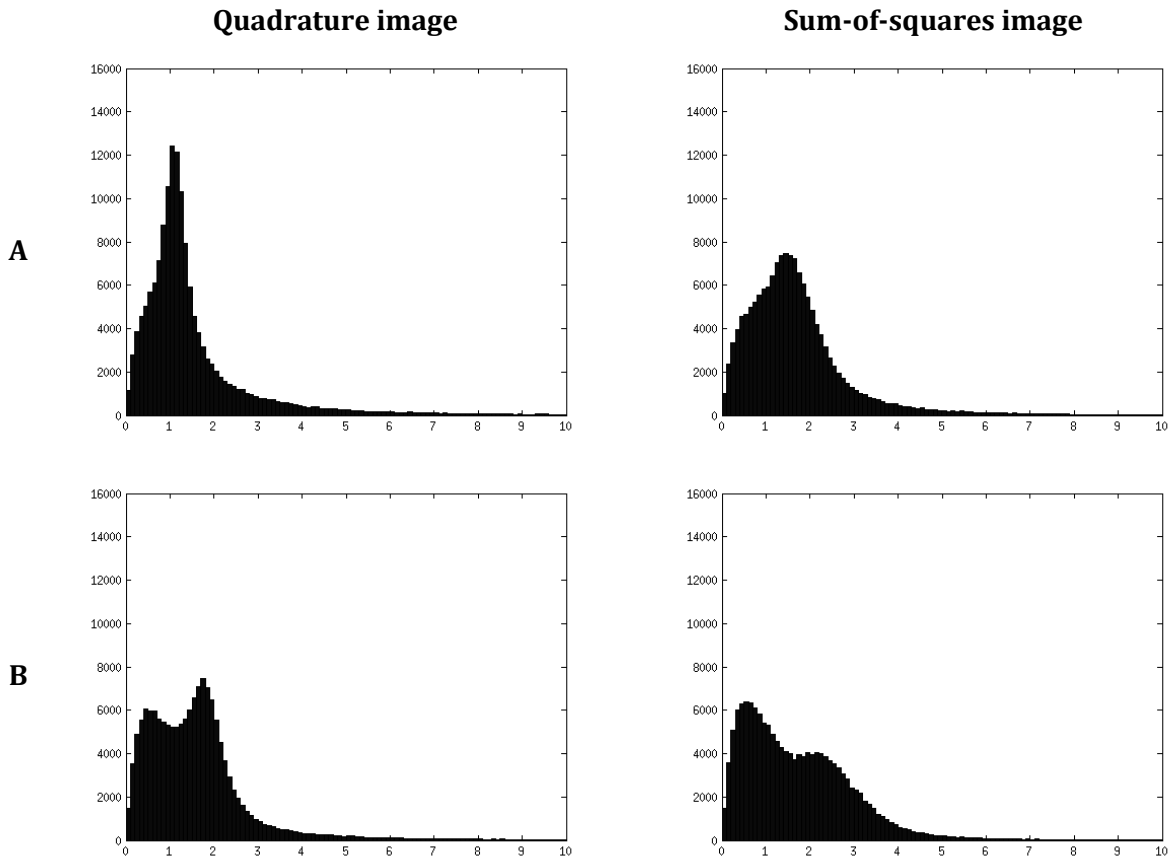
Since the results with the different sensitivity maps were quite similar, a simple statistical comparison of the outputs with reduction rate 4 was also done. The magnitudes of the outputs were compared with the magnitudes of the quadrature image and the sum-of-squares image as references. The sum-of-squares image was included in order to give a more fair comparison for the results of the sensitivity maps based on it, since their output has some intensity bias that we can accept but that would give bad results when compared to a homogenous image.

In the first comparison, the volumes to be compared were first normalized by dividing each with its maximum value in order for the values to vary between 0 and 1. Then, the output image was divided with the ratio between its own mean and the mean of the reference image, so that both images were normalized to have the same mean. Following this, the square of the difference between the two images was calculated. The mean of this squared difference over the whole images was finally taken. The results are shown in Table 5. The smaller values the better.

	A	B	C	D	E
Quadrature	0.0074	0.0077	0.0083	0.0091	0.0084
SoS	0.0058	0.0073	0.0079	0.0042	0.0045

Table 5. Mean of the squared difference between the outputs of SENSE reconstruction with reduction factor 4 using different sensitivity maps, and a reference image (quadrature and sum-of-squares).

As a complement to this, the ratio between the images to be compared was also measured. The ratio was calculated by dividing the output image with the reference image. Whenever division by 0 occurred, the output was set to 0. The resulting ratio image was then divided by its mean. Histograms of the respective ratio images are shown in Figure 44. Values of 0 and outliers higher than 10 have been excluded. The more the values are centered around 1, the better.



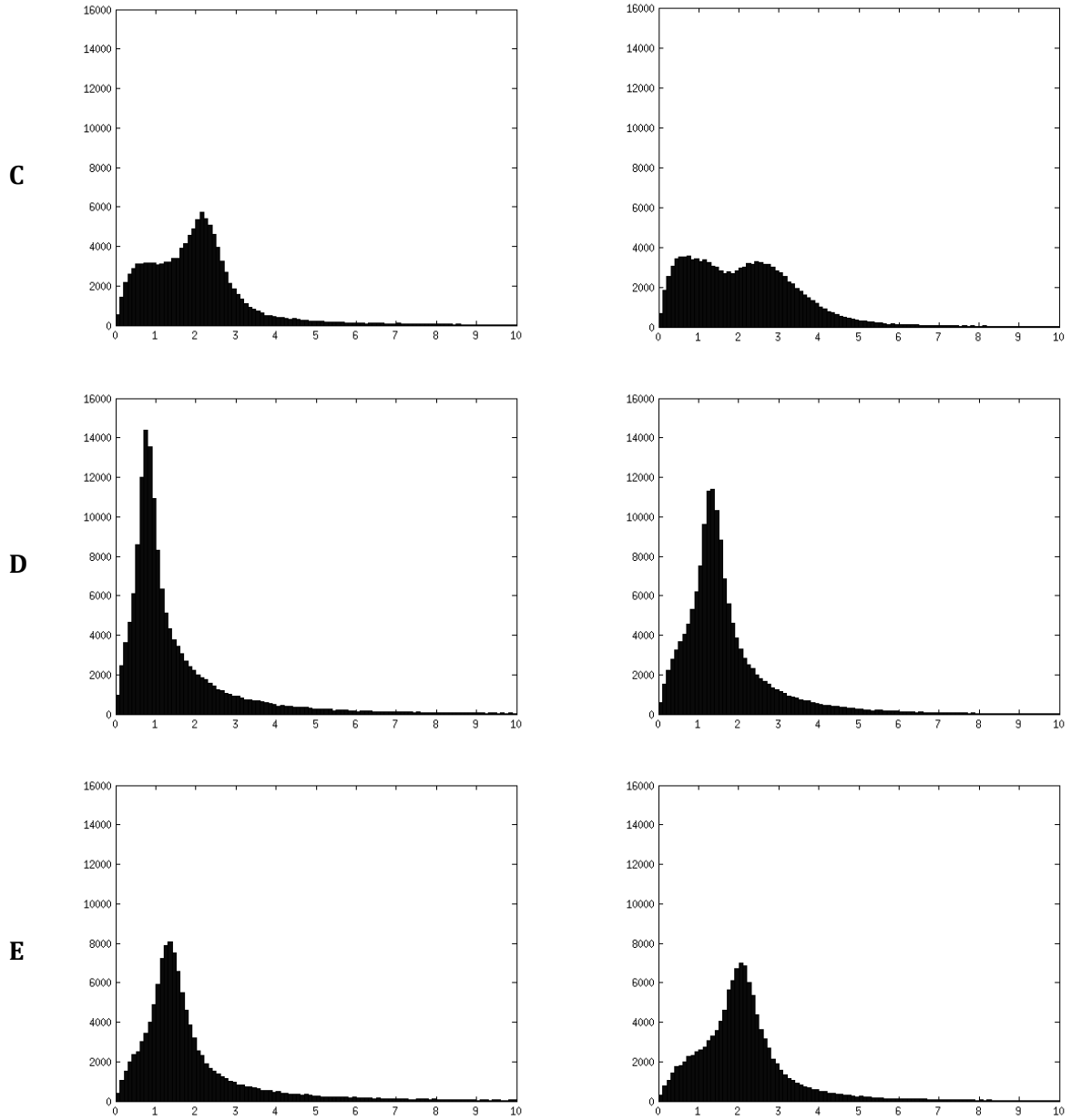


Figure 44. Histograms of the ratio between the outputs of SENSE reconstruction with reduction factor 4 using sensitivity map A-E and a reference image (quadrature or sum-of-squares).

A quick glance at Figure 44 suggests that the best result was achieved with sensitivity map D. Images showing the magnitude of more slices from this output are shown in Figure 45. As comparison, slices from the SENSE reconstruction output made by the MR-scanner itself during Cartesian sampling are shown in Figure 46. For a further discussion between the results, see chapter 6. For images of more slices of the outputs from the other sensitivity maps as well as phase images, see Appendix B.

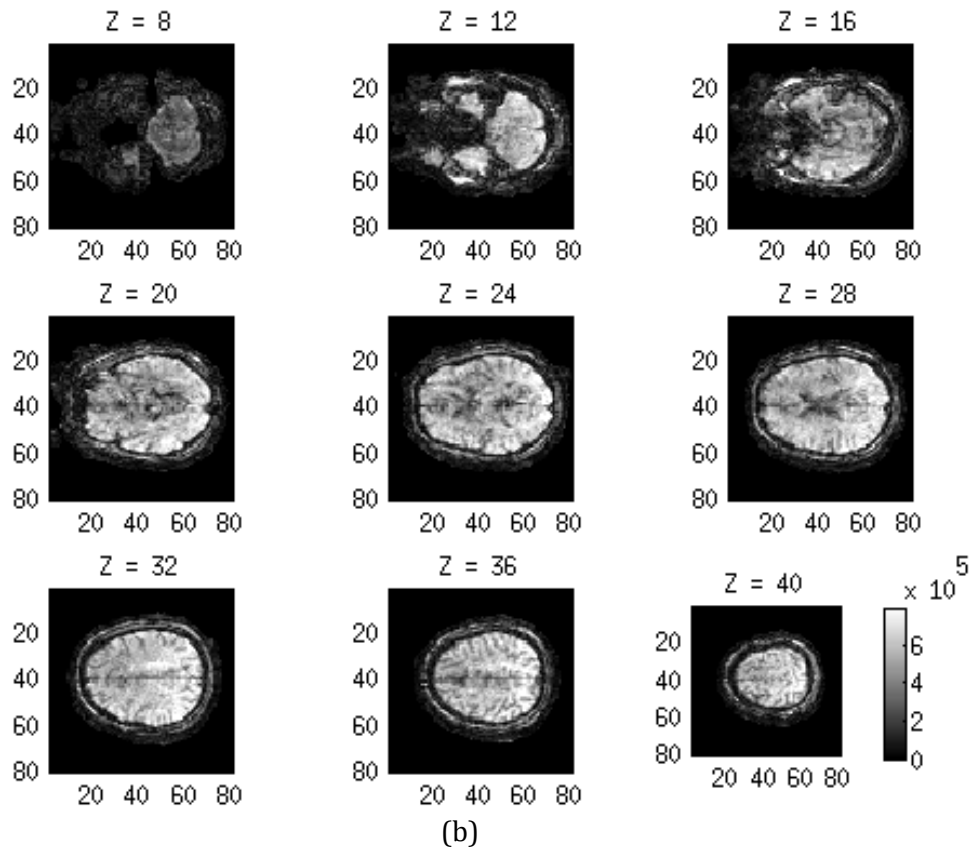
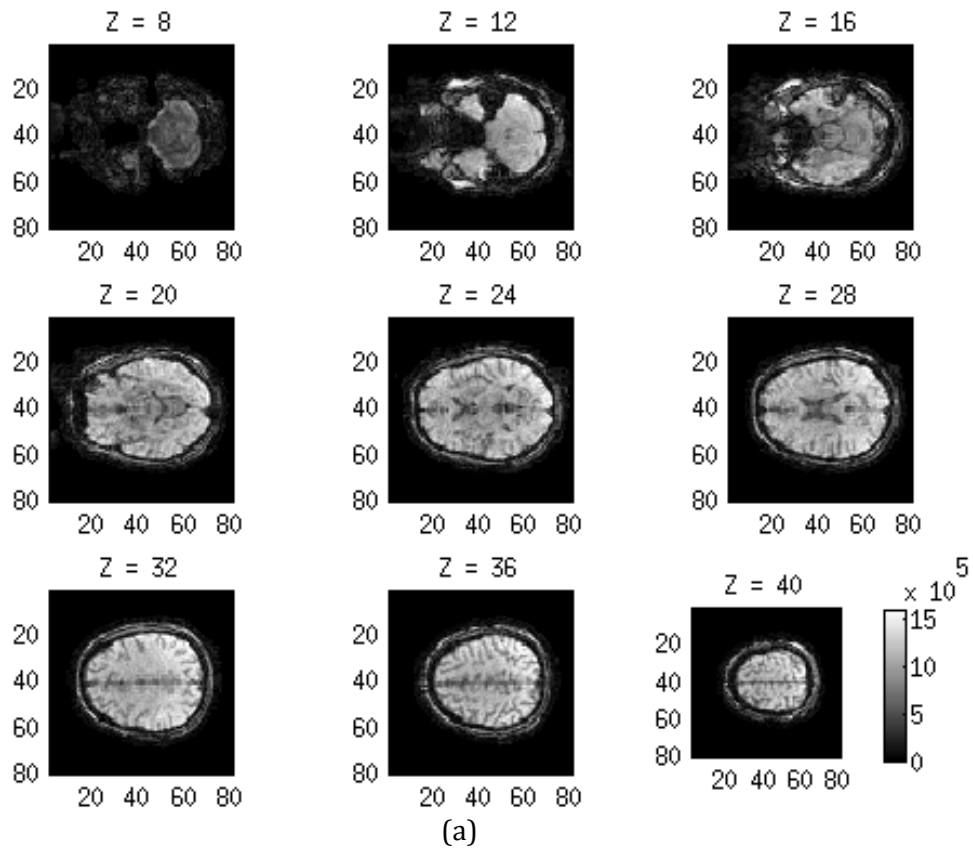


Figure 45. Results of SENSE reconstruction using sensitivity map D, based on division by a sum-of-squares image and normalized convolution applied on the magnitude and phase together, for reduction rates (a) 2 and (b) 4 respectively.

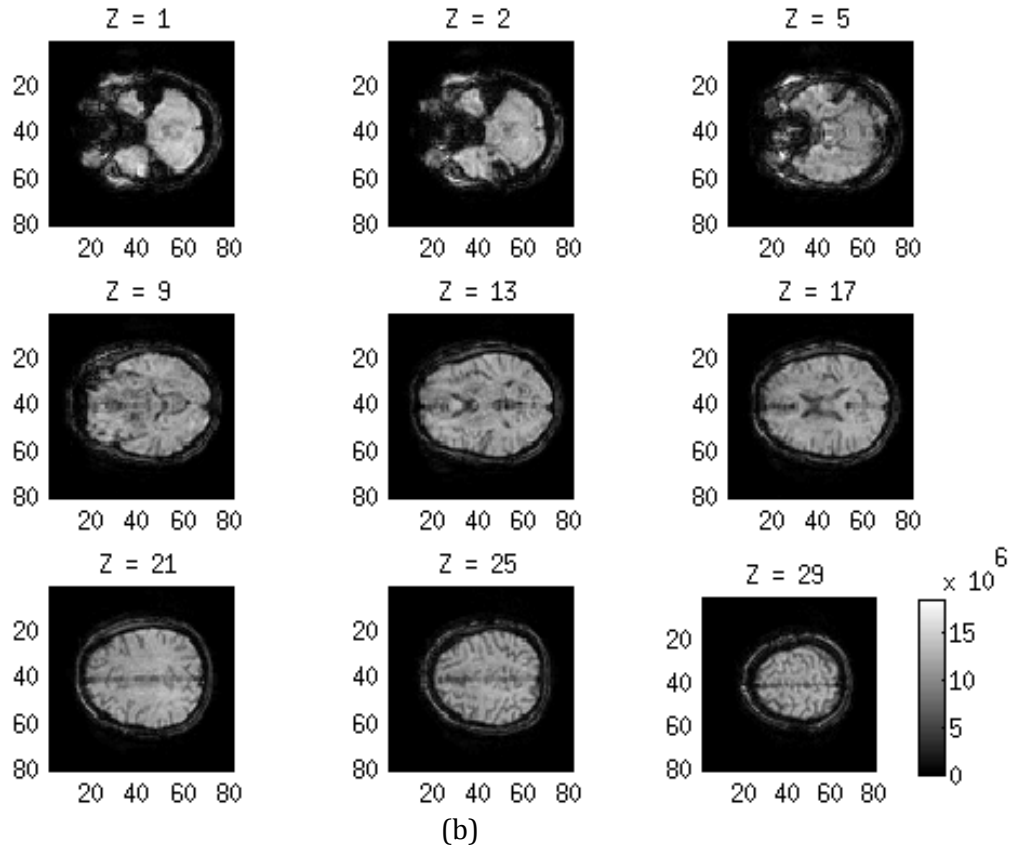
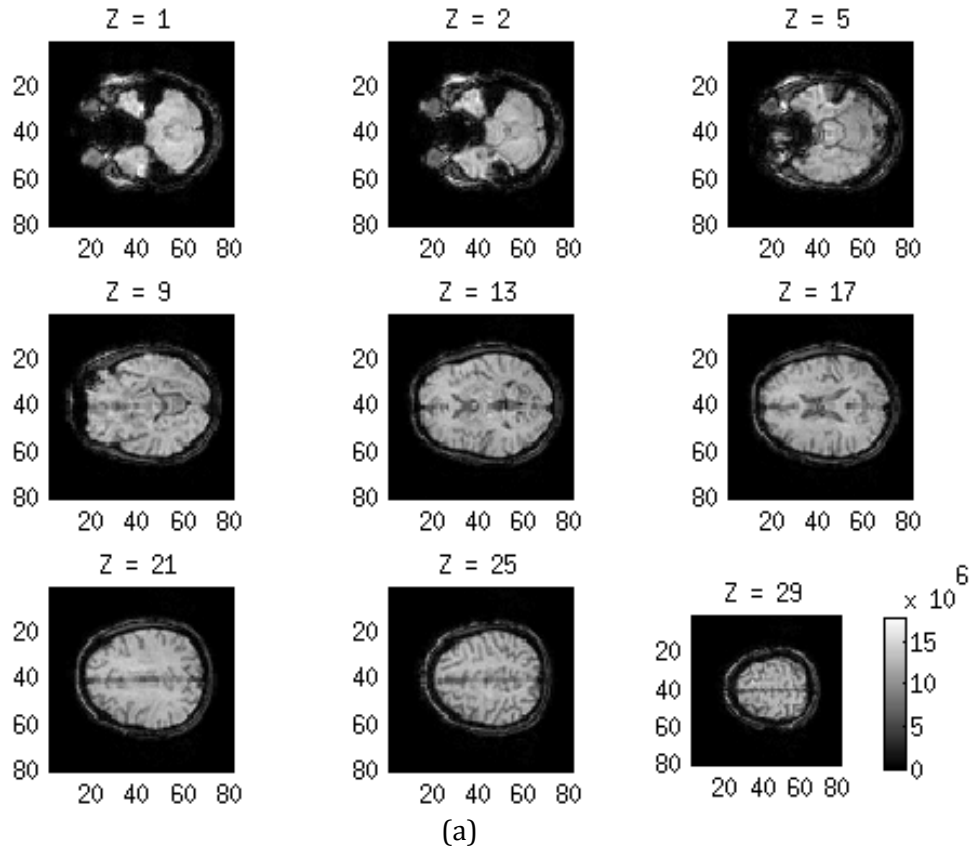
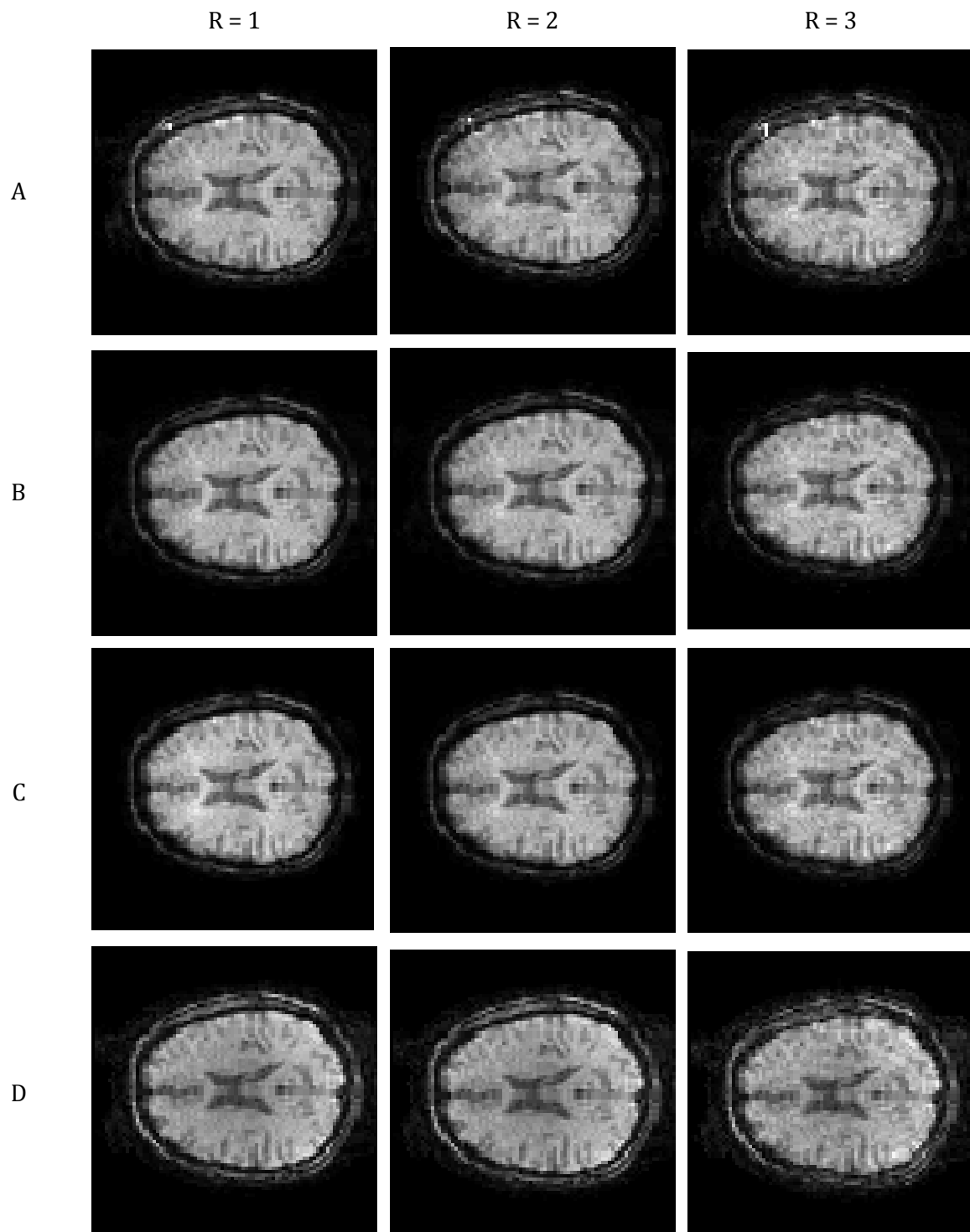
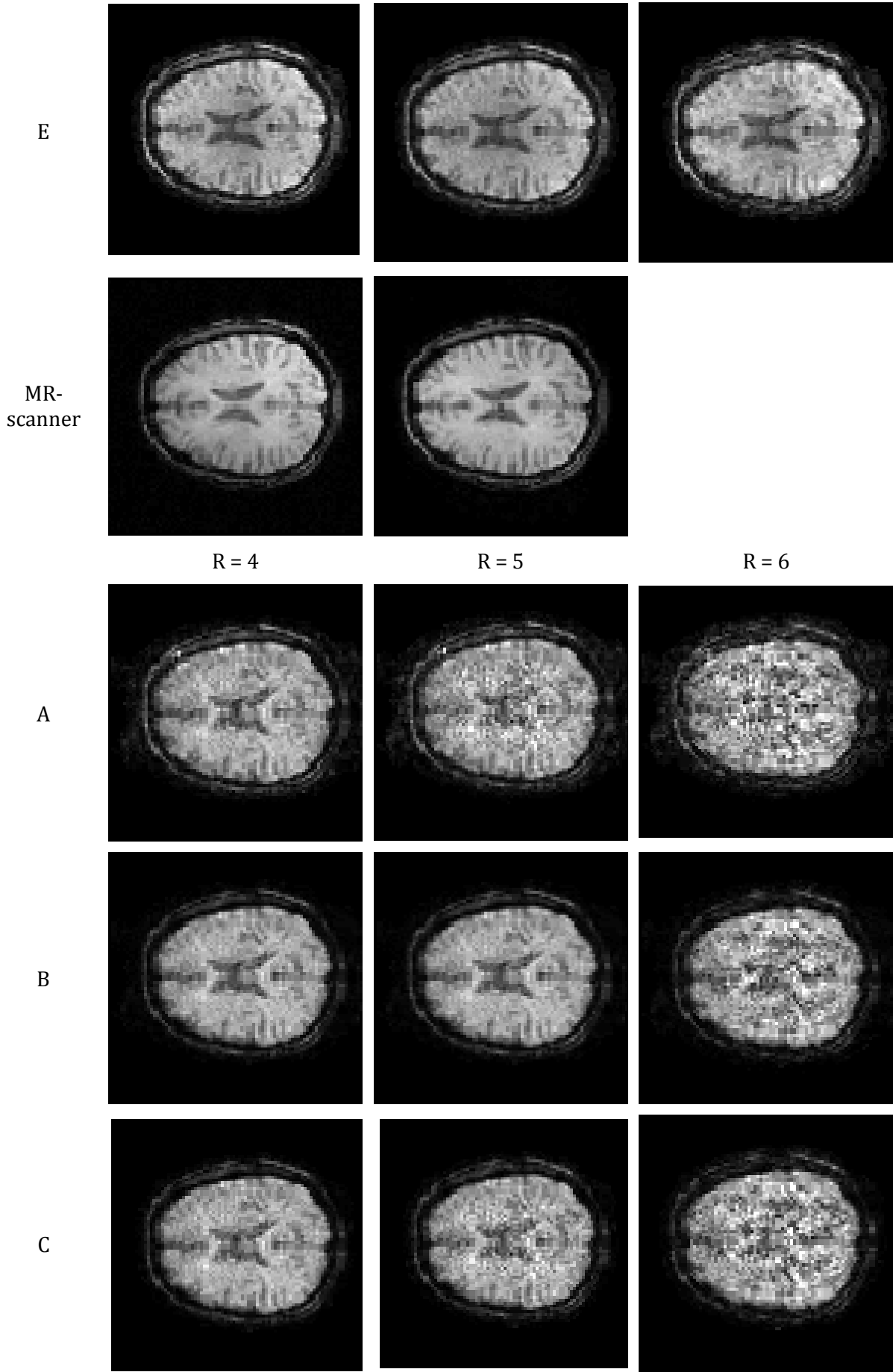


Figure 46. Results of SENSE reconstruction done by the MR-scanner itself using Cartesian sampling with reduction rates (a) 2 and (4) respectively.

5.3 Reconstruction of Manual SENSE Reduction

Figure 47 shows the results of SENSE reconstruction of data with reduction factors 1...6, where the SENSE reduction has been performed by manually removing k -space rows a posteriori from fully sampled data.





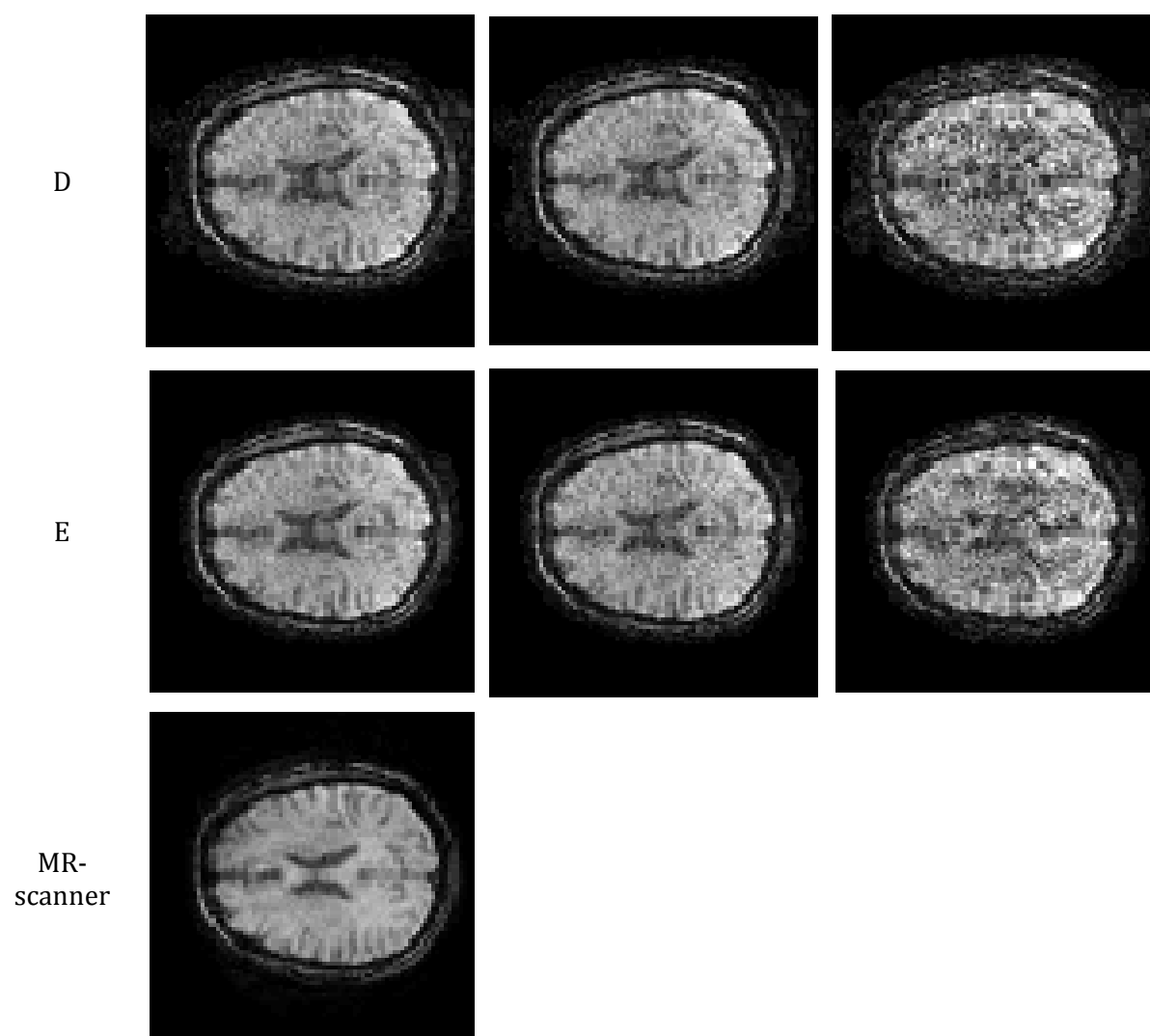


Figure 47. Results of SENSE reconstruction using different sensitivity maps with reduction rates 1...6, compared with images reconstructed from Cartesian sampled data made by the MR-scanner itself.

6 Discussion

According to the statistical analysis in section 5.2, both the mean of the differences and the histograms of the ratios between the outputs and the reference images indicate that the best results were achieved with sensitivity maps A, D and E, with D as the very best one. Of the sensitivity maps based on division by the quadrature image, the best one seems to have been A, where normalized convolution was applied on the magnitude and phase together using a larger applicability function with standard deviation 2. This indicates that in this case, the phase image of the raw sensitivity map did not change fast enough for any special treatment of the phase when applying normalized convolution to be needed. For sensitivity maps D and E based on division with a sum-of-squares image, the mean of the squared difference with the quadrature image was better for E, while the other results spoke in favor of D. Over all, both visual inspection of the results and the statistical analysis point out sensitivity map D as giving the best result. The images of the outputs of the SENSE reconstruction with this sensitivity map shown in Figure 45 can therefore be seen as the main result fulfilling the objective of this thesis to implement SENSE into PRESTO-CAN.

In Section 5.3, however, the best results seem to have been achieved with sensitivity maps B and E where normalized convolution is applied on the magnitude only (especially when looking at the results of reduction factors 4 and higher). This seems a little contradictory to the results in Section 5.2. It could be that the worse results of sensitivity maps B and E in the statistical analysis in Section 5.2 comes from intensity bias due to normalized convolution of the phase, while this at the same time leads to reduction of noise and artifacts which makes them look better in the results in Section 5.3. And of course, since the SENSE reduction was performed in different manners in Section 5.2 and 5.3 respectively, it could simple be that different methods give better results depending on the situation. In summary, it is difficult to draw any definitive general conclusion of which method of handling the phase when applying normalized convolution is to prefer. That the results here are generally better in Section 5.3 is not strange considering that the very same volumes that were SENSE reconstructed also were used for calculating the sensitivity maps, and in general we should be a little careful to draw too much conclusions based on the results of this experiment.

A more important question is which of the two main methods of calculating sensitivity maps, division by quadrature image or division by sum-of-squares image, is to prefer. We already made the conclusion that the best results in section 5.2 generally were achieved with sensitivity map D. The results in section 5.3 at the same time seem to be best for sensitivity map E, at least for $R = 4$ and $R = 5$ (in good competition with B). From this we can draw the conclusion that in general the results were a little better with the sum-of-squares method. As stated in section 3.3.4, the main drawback with using a body coil image (represented by the quadrature image in our case) is that it cannot be acquired at the same time as the surface coils images. During the acquisition of the in vivo images used in this thesis, the time between the acquisition of the quadrature image and the surface coil images was quite long (several minutes) due to that other scans with other settings such like other EPI factors and scans using PRESTO-CART were done in between. During this time, the magnetic field and thus the sensitivities of the coils could have changed slightly. In other words, the conditions were not optimized for the quadrature image to be used as a basis for creating sensitivity maps. If these conditions would have been better, the results for sensitivity maps A-C might also have been better compared to D and E.

Since the sum-of-squares image is calculated from the surface coil images themselves, we get rid of the problem of the images having been recorded at different moments in time. In return, the output usually has some intensity bias, and in our case we can see that the middle is a little darker compared to the images reconstructed by the MR-scanner. This intensity bias between the result and the recorded object comes from the fact that the sum-of-squares image generally does not have the same intensity as the recorded object. However, since this intensity bias is constant over time, it might not be a problem when used for fMRI applications. In fMRI, we are mainly interested in changes in intensity between different points in time of each voxel rather than the intensity relationships between different voxels, and this is not affected by the fact that we have a slight constant intensity difference between the retrieved images and the recorded object.

As can be seen by comparing images (f) (acquired with PRESTO-CART) and (g) (acquired with PRESTO-CAN) in Figure 43, images acquired and reconstructed with PRESTO-CAN without SENSE reduction contains a little more noise compared to when using Cartesian sampling. This can be accepted since PRESTO-CAN has other advantages of Cartesian sampling, especially when it comes to temporal resolution. In [30], it is argued that the sum-of-squares method generally gives better SNR than when using a body coil or quadrature image as reference. This can also be confirmed by the results shown in this thesis. However, that we generally have a greater need of noise reduction in PRESTO-CAN images together with the fact that we can live with the intensity bias in the fMRI application we are using the method for, inclines us to draw the conclusion that the sum-of-squares method is the most suitable method of acquiring sensitivity maps for SENSE parallel imaging with PRESTO-CAN.

Comparing the results of reduction rate 2 (Figure 42) with those of reduction rate 4 (Figure 43) shows that while we get totally acceptable results with reduction factor 2, the noise level is considerably higher when we increase the reduction factor to 4. As stated in Section 1.2, the minimum reduction rate with acceptable noise level with 8 receiver coils should be at least between 2.66 and 4. Therefore, it is a little disappointing that the result with reduction rate 4 is so noisy, especially since we got acceptable results with reduction rate 4 both for the simulated 3D data sampled in the same way as PRESTO-CAN (section 4.2), as well as for the real data acquired with PRESTO-CART (section 4.3). It is not unlikely that the many steps in the procedure for reconstructing images acquired with PRESTO-CAN, for example the correction procedures and the Cartesian interpolation, leads to increased noise levels when parallel imaging is applied, but due to time restrictions it has unfortunately not been possible to analyze these more thoroughly in this thesis. In order to determine the exact limit of what reduction rate can be applied on real data with a noise level acceptable for clinical use, it would have been necessary to make more recordings with the MR-scanner with reduction rates of intermediate values between 2 and 4. This is also the reason to why a more thorough analysis of how different reduction rates affect the signal-to-noise ratio and image quality was not able to be performed.

Another glance at the results in section 5.3 can also make us consider that with sensitivity maps B and E the results are quite acceptable for $R = 4$ and still only moderately noisy for $R = 5$. This at least shows that in theory, under perfect conditions, there is a possibility to get acceptable image quality with a reduction rate between 4 and 5 with data achieved with PRESTO-CAN. However, in order to be fully honest we should also point out that we have a slight advantage due to the fact that the brain does not fill out the whole FOV in the y -direction.

6.1 Future Work

In order to further evaluate parallel imaging according to the SENSE method with PRESTO-CAN, further data acquisition needs to be done with a wider selection of different reduction rates applied so that comparisons between the results of SENSE reconstruction of these can be done. More EPI factors also need to be tested as well as a true 3D-plus-time fMRI experiment where PRESTO-CAN and PRESTO-CART are compared at different SENSE reduction rates. To get better results with sensitivity maps based on division with a reference image (body coil or quadrature image), the time between the acquisition of the reference image and the SENSE reduced data should be made shorter. Other ways of calculating the certainty functions used for the normalized convolution could also be investigated more thoroughly. And while one of the objectives of this thesis has been to show that normalized convolution can be used as an alternative to polynomial fitting in order to refine the sensitivity maps, a comparison between the two by also implementing the latter would of course also have been nice. A combination of the two could possibly also be used.

7 Conclusions

In this thesis, we have shown that it is indeed possible to use parallel imaging according to the SENSE method together with the non-Cartesian 3D fMRI method PRESTO-CAN. In this way we have made it possible to simultaneously make use of the advantages in terms of increased temporal resolution that is provided by the radial sample pattern in the (k_x, k_z) -plane as well as by the reduced scan time due to the implementation of Cartesian SENSE in the k_y -direction. Using normalized convolution in order to refine the sensitivity maps used for the SENSE reconstruction, we have been able to reconstruct images with nearly no quality loss using in vivo data recorded with 8 receiver coils and the reduction rate $R = 2$. In addition, relatively good results were achieved even with $R = 4$. This means that the temporal resolution can be increased with at least a factor of 2, and possibly even higher depending on the demands on image quality. We have also shown that the way of determining raw sensitivity maps most suitable for use with the PRESTO-CAN method is to divide the images from the surface coils with a sum-of-squares image calculated from the same images rather than using a homogenous image (body coil image or quadrature image) recorded at a different moment in time. To sum everything up, while PRESTO-CAN already allows for better temporal resolution in fMRI than conventional methods using fully Cartesian sample patterns, the successful implementation of parallel imaging according to the SENSE method performed in this thesis has contributed even more to this.

8 References

- [1] M. Magnusson, O. D. Leinhard, P. Brynolfsson, P. Thyr, and P. Lundberg, "3D magnetic resonance imaging of the human brain - novel radial sampling, filtering and reconstruction," in *Proc of the 12th IASTED International Conference of Signal and Image Processing (SIP 2010)*, Calgary, 2010, Available from: <http://liu.diva-portal.org/smash/record.jsf?searchId=2&pid=diva2:386056>.
- [2] M. Magnusson, O. Dahlqvist Leinhard, P. Brynolfsson, and P. Lundberg, "Radial k-space sampling: step response using different filtering techniques," in *ISMRM Workshop on Data sampling and Image Reconstruction*, The Enchantment Resort, Sedona, Arizona, 2009.
- [3] M. Magnusson, O. Dahlqvist Leinhard, P. Brynolfsson, and P. Lundberg, "Improved temporal resolution in radial k-space sampling using an hourglass filter," in *Proceedings of the ISMRM 17th Scientific Meeting & Exhibition*, Honolulu, Hawaii, USA, 2009.
- [4] M. Magnusson, O. Dahlqvist Leinhard, and P. Lundberg, "A 3D-plus-time radial-Cartesian hybrid sampling of k-space with high temporal resolution and maintained image quality for MRI and fMRI," in *ISMRM 2011*, Montreal, 2011.
- [5] K. P. Pruessmann, M. Weiger, M. B. Scheidegger, and P. Boesiger, "SENSE: sensitivity encoding for fast MRI," *Magnetic Resonance in Medicine*, vol. 42(5), pp. 952-962, Nov 1999.
- [6] P. Thyr, "Method for Acquisition and Reconstruction of non-Cartesian 3-D fMRI," Linköping, Student thesis LITH-ISY-EX--08/4058--SE, 2008.
- [7] P. Brynolfsson, "Using Radial k-space Sampling and Temporal Filters in MRI to Improve Temporal Resolution," Linköping, Student thesis LIU-IMH/RV-A--10/003--SE, 2010.
- [8] M. Ragnehed et al., "Visual grading of 2D and 3D functional MRI compared with image-based descriptive measures," *European Radiology*, vol. 20, pp. 714-724, March 2010.
- [9] B. Madore and N. J. Pelc, "SMASH vs. SENSE," *Proc. Intl. Sot. Mag. Reson. Med.*, vol. 8, 2000.
- [10] M. A. Bernstein, K. F. King, and J. Z. Xiaohong, *Handbook of MRI Pulse Sequences*. Burlington, MA: Elsevier Academic Press, 2004, ISBN 0-12-092861-2.
- [11] J. P. Hornak. (1996) The Basics of MRI. [Online]. <http://www.cis.rit.edu/htbooks/mri/>
- [12] A. Eklund, M. Andersson, and H. Knutsson. (2010, October) TBMI02 Medical Image Analysis Course Compendium. [Online]. http://www.imt.liu.se/edu/courses/TBMI02/pdfs/TBMI02_course_compendium.pdf
- [13] CMIV. (2011, May) CMIV (Center for Medical Image Science and Visualization). [Online]. <http://www.cmiv.liu.se/about-cmiv/photos/facilities/mrilight>
- [14] J. Rydell, "Advanced MRI Data Processing," Linköping University, Linköping, PhD thesis 2007.

- [15] S. F. W. Neggers, E. J. Hermans, and N. F. Ramsey, "Enhanced sensitivity with fast three-dimensional blood-oxygen-level-dependent functional MRI: comparison of SENSE-PRESTO and 2D-EPI at 3 T," *NMR in Biomedicine*, vol. 21, pp. 663-676, January 2008.
- [16] O. Friman, "Adaptive analysis of functional MRI data," Linköping University, Linköping, PhD thesis 2003.
- [17] G. Liu, G. Sobering, J. Duyn, and C. T. W. Moonen, "A functional MRI technique combining principles of echo-shifting with a train of observations (PRESTO)," *Magnetic Resonance in Medicine*, vol. 30, no. 6, pp. 764-768, December 1993.
- [18] J. O'Sullivan, "A fast sinc function gridding algorithm for Fourier inversion in computer tomography," *IEEE Trans. Med. Imaging*, vol. MI-4, no. 4, pp. 200-207, 1985.
- [19] J. Pauly. (2007, October) Non-Cartesian Reconstruction. Lecture notes.
- [20] P. B. Roemer, W. A. Edelstein, Hayes, S. P. C. E. Souza, and O. M. Mueller, "The NMR phased array," *Magnetic Resonance in Medicine*, vol. 16, pp. 192-195, 1990.
- [21] J. W. Carlson, "An algorithm for NMR imaging reconstruction based on multiple RF receiver coils," *Journal of Magnetic Resonance Imaging*, vol. 74, pp. 376-380, 1987.
- [22] M. Hutchinson and U. Raff, "Fast MRI data acquisition using multiple detectors," *Magnetic Resonance in Medicine*, vol. 6, pp. 87-91, 1988.
- [23] D. K. Sodickson and W. J. Manning, "Simultaneous acquisition of spatial harmonics (SMASH): Fast imaging with radiofrequency coil arrays," *Magnetic Resonance in Medicine*, vol. 41, pp. 1009-1022, 1997.
- [24] K. P. Pruessmann, P. Börnert, and P. Boesiger, "Advances in sensitivity encoding with arbitrary k-space trajectories," *Magnetic Resonance in Medicine*, vol. 46(4), pp. 638-651, Oct 2001.
- [25] M. A. Griswold et al., "Generalized autocalibrating partially parallel acquisitions (GRAPPA)," *Magnetic Resonance in Medicine*, vol. 47(6), pp. 1202-1210, Jun 2002.
- [26] N. Seiberlich, "Parallel Imaging: Principles and Implementation," in *ISMRM*, Stockholm, 2010.
- [27] L. Eldén and L. Wittmeyer-Koch, *Numerisk analys - en introduktion*, 3rd ed. Lund, Sverige: Studentlitteratur, 1987.
- [28] K. F. King and L. Angelos, "SENSE Image Quality Improvement Using Matrix Regularization," in *Proceedings of the ISMRM 9th Scientific Meeting*, Glasgow, 2001, p. 1771.
- [29] T. Öhman, "The Influence of the Reference Measurement in MRI Image Reconstruction Using Sensitivity Encoding (SENSE)," Karolinska University Hospital, Solna, Student thesis 2006.

- [30] E. G. Larsson, D. Erdogmus, R. Yan, J. C. Principe, and J. R. Fitzsimmons, "SNR-optimality of sum-of-squares reconstruction for phased-array magnetic resonance imaging," *Journal of Magnetic Resonance*, vol. 163, pp. 121-123, 2003.
- [31] D. J. Griffiths, *Introduction to Electrodynamics*.: Prentice Hall, 1998.
- [32] K. P. Pruessmann, M. Weiger, M. B. Scheidegger, and P. Boesiger, "Coil sensitivity maps for sensitivity encoding and intensity correction," in *Proceedings of the ISMRM 6th Annual Meeting*, Sydney, 1998, p. 2087.
- [33] H. Knutsson and C-F. Westin, "Normalized and differential convolution: Methods for interpolation and filtering of incomplete and uncertain data," in *CVPR*, 1993, pp. 515-523.
- [34] G. Farnebäck, "Polynomial Expansion for Orientation and Motion Estimation," Linköping University, Department of Electrical Engineering, Computer Vision, Linköping, Doctoral thesis ISBN 91-7373-475-6, 2002.
- [35] R. C. Gonzalez and R. E. Woods, *Digital Image Processing*, 3rd ed. USA: Addison-Wesley Publishing Company, 2008.
- [36] L. Tiemao, Z. Xuyuan, and G. Xin, "Super-resolution reconstruction of MR image based on structure-adaptive normalized convolution," in *ISCP2010 Proceedings*, 2010, pp. 760-762.
- [37] A. Katartzis and M. Petrou, "Robust bayesian estimation and normalized convolution for super-resolution image reconstruction," in *Proceedings of the IEEE Computer Society Conference on Computer Vision and Pattern Recognition (CVPR)*, 2007, pp. 1-7.
- [38] G. Farnebäck. (2001) Spatial Domain Toolbox. [Online]. http://lsvn.lysator.liu.se/svnroot/spatial_domain_toolbox/trunk/

Appendix A: Sensitivity Maps

In this appendix are shown one magnitude and phase of one slice from every receiver coil of the raw sensitivity maps as well as the refined sensitivity maps A-E described in Section 5.1.

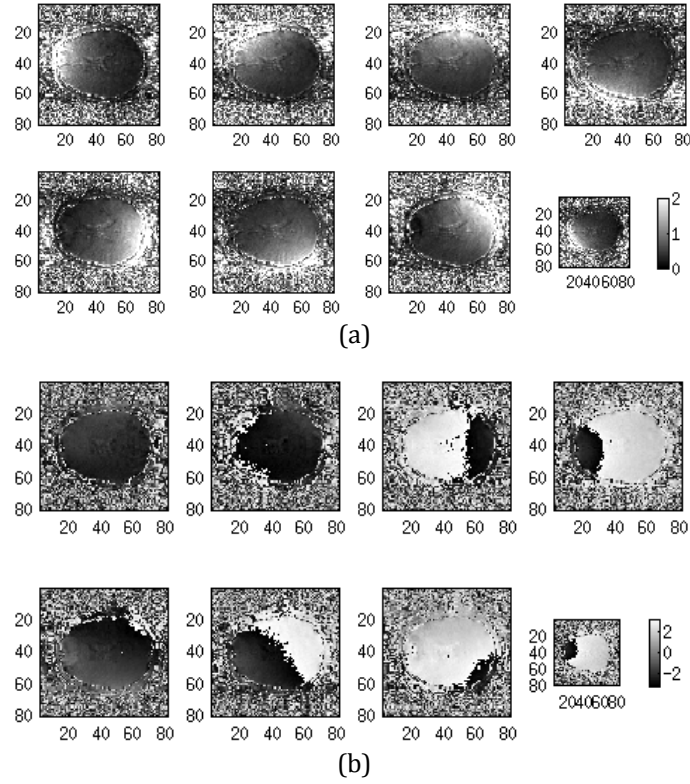


Figure 48. (a) Magnitude and (b) phase of one slice in the (k_x, k_y) -plane of a raw sensitivity map for all 8 receiver coils, calculated by division with a quadrature image volume.

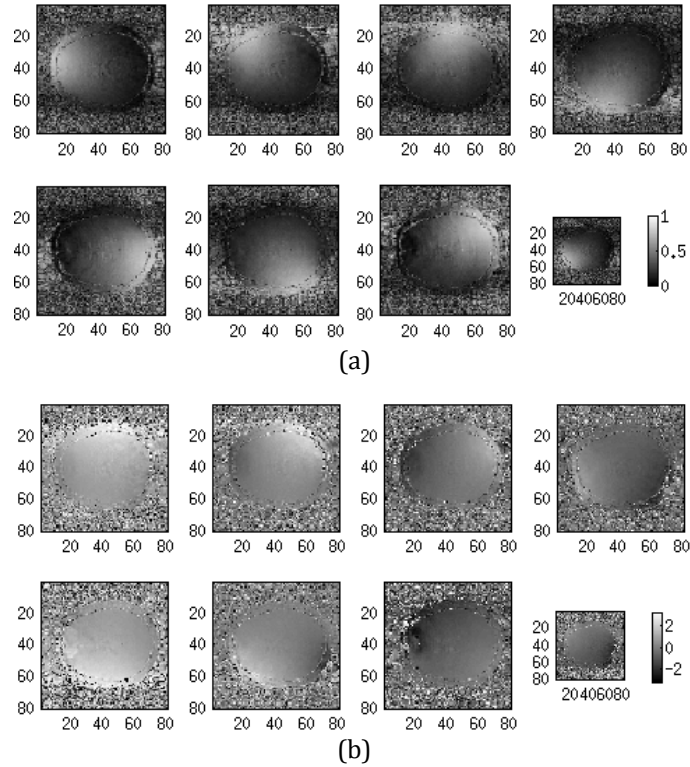


Figure 49. (a) Magnitude and (b) phase of one slice in the (k_x, k_y) -plane of a raw sensitivity map for all 8 receiver coils, calculated by division with a sum-of-squares image volume.

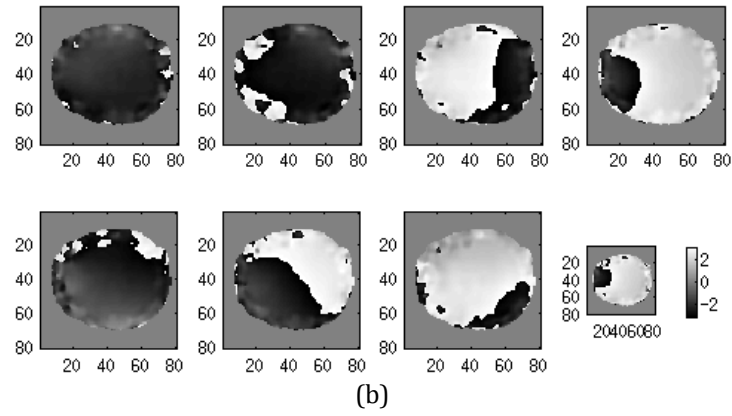
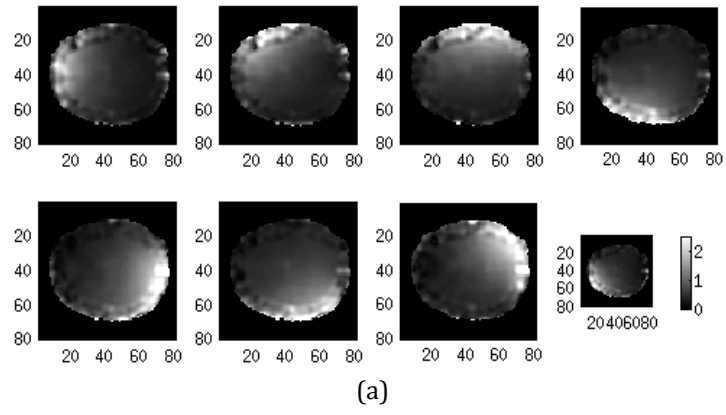


Figure 50. (a) Magnitude and (b) phase of one slice from each of the surface coils of sensitivity map A.

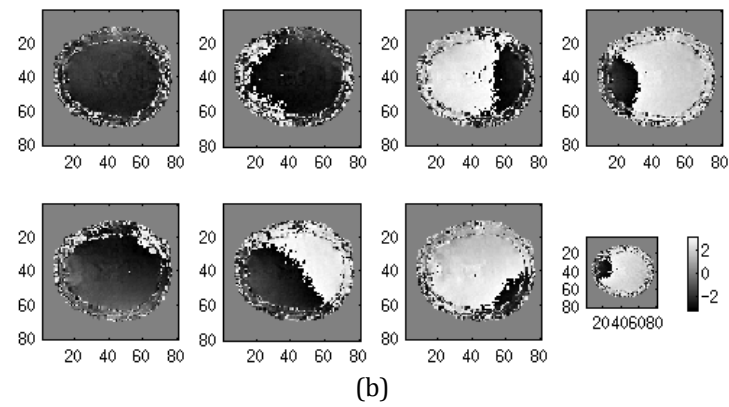
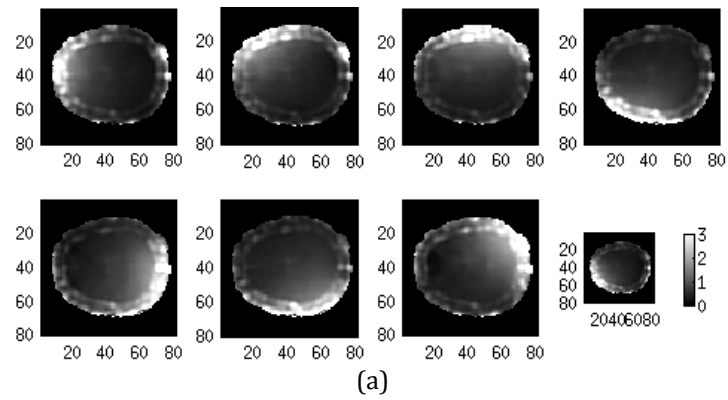


Figure 51. (a) Magnitude and (b) phase of one slice from each of the surface coils of sensitivity map B.

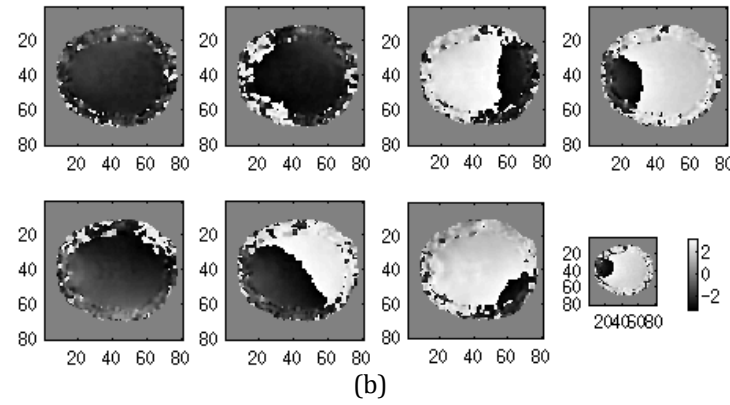
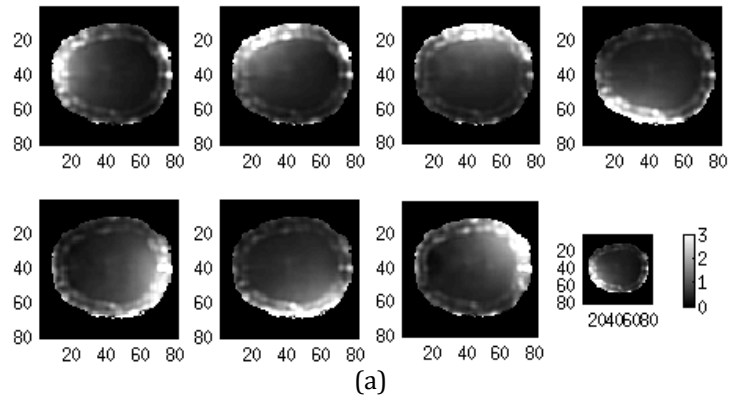


Figure 52. (a) Magnitude and (b) phase of one slice from each of the surface coils of sensitivity map C.

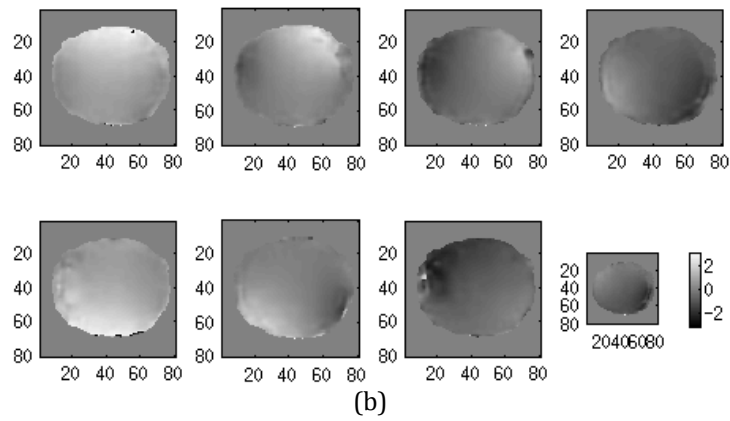
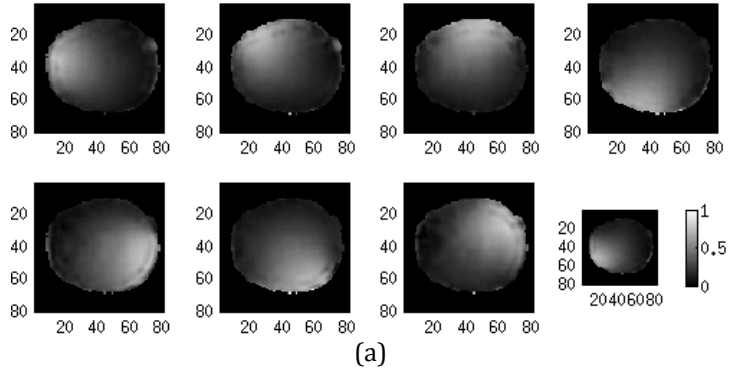


Figure 53. (a) Magnitude and (b) phase of one slice from each of the surface coils of sensitivity map D.

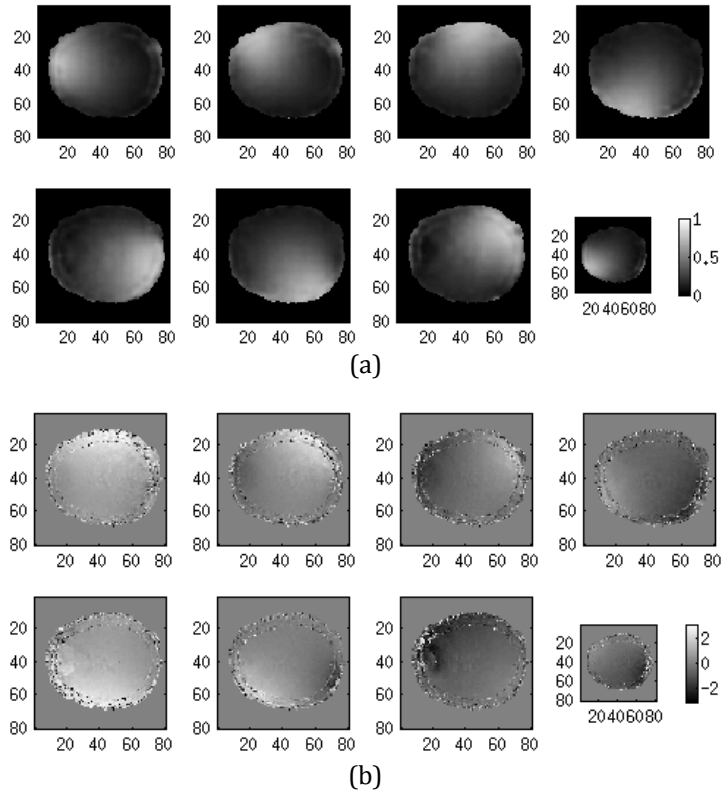


Figure 54. (a) Magnitude and (b) phase of one slice from each of the surface coils of sensitivity map E.

Appendix B: Results of SENSE Reconstruction

In this appendix are shown more slices as well as phase images of SENSE reconstruction using the sensitivity maps described in section 5.1.

Reduction Rate 2

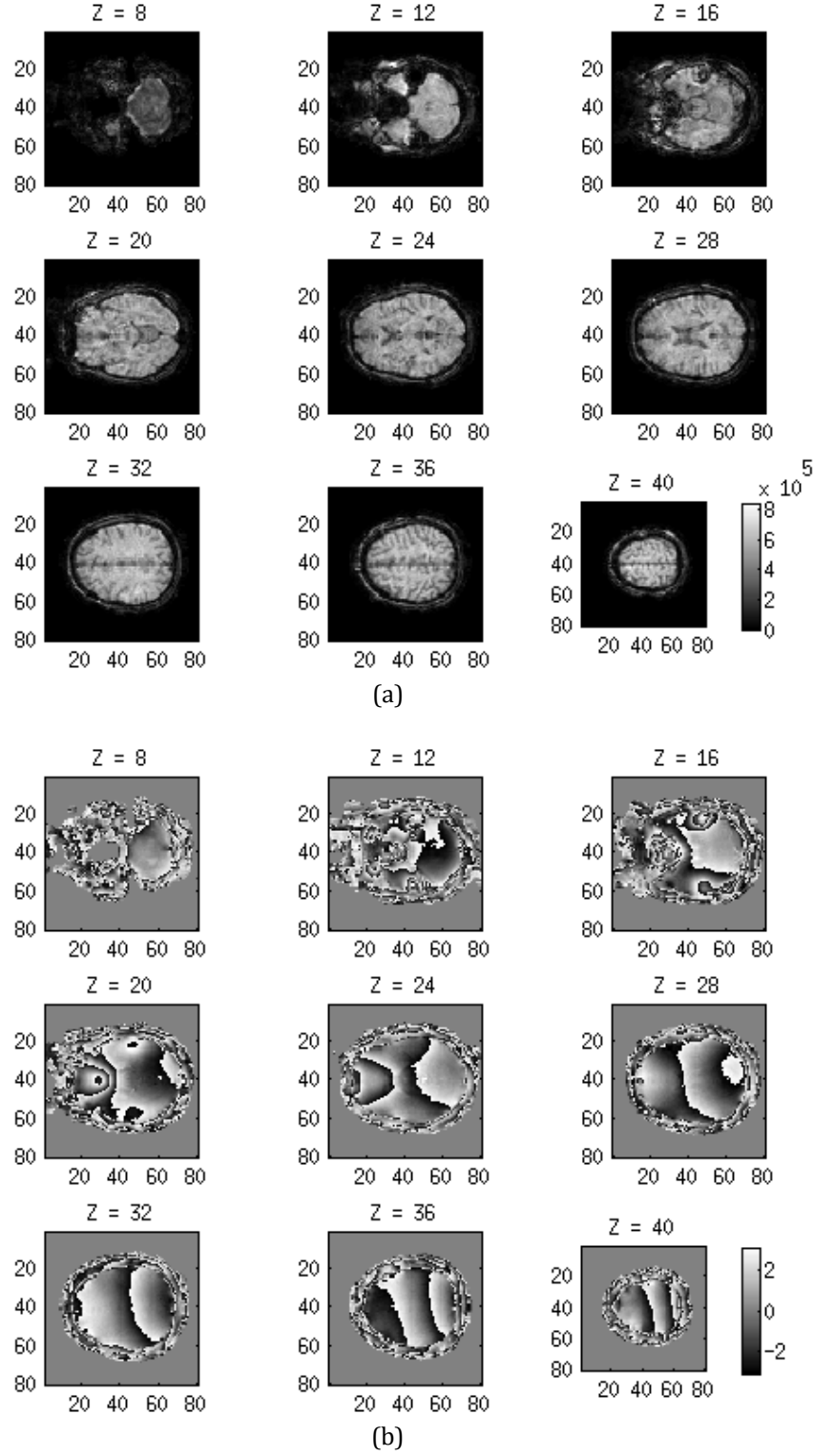


Figure 55. (a) Magnitude and (b) phase image volumes of the output after SENSE reconstruction with reduction rate 2 using sensitivity map A.

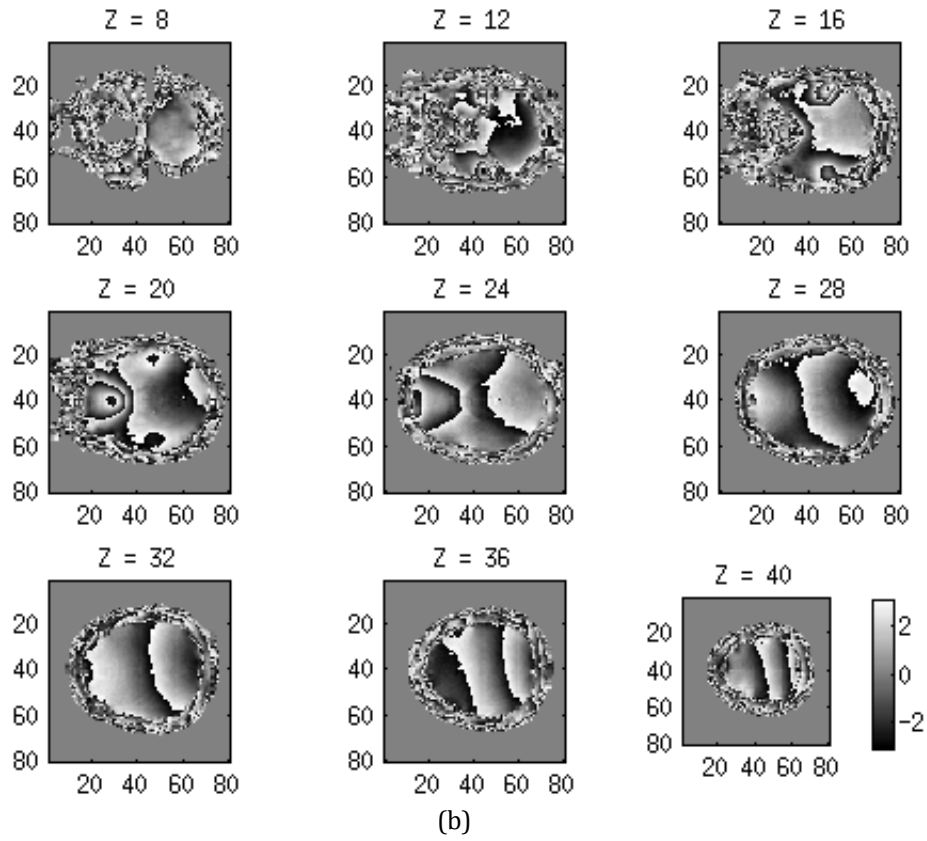
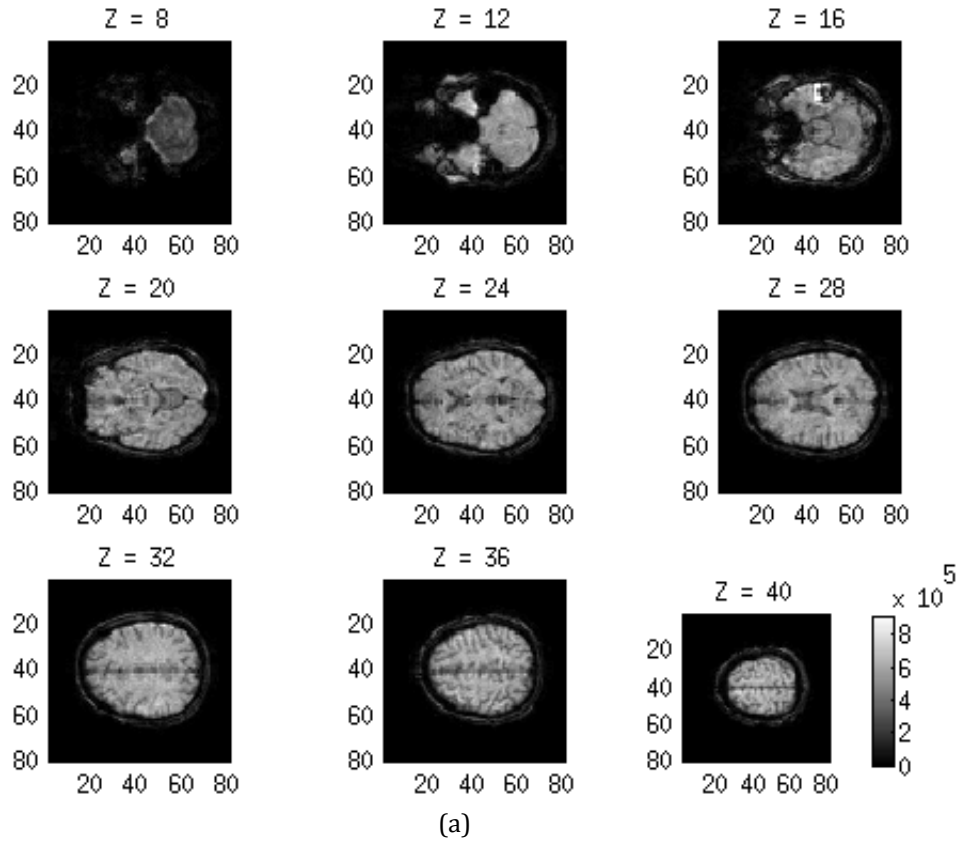
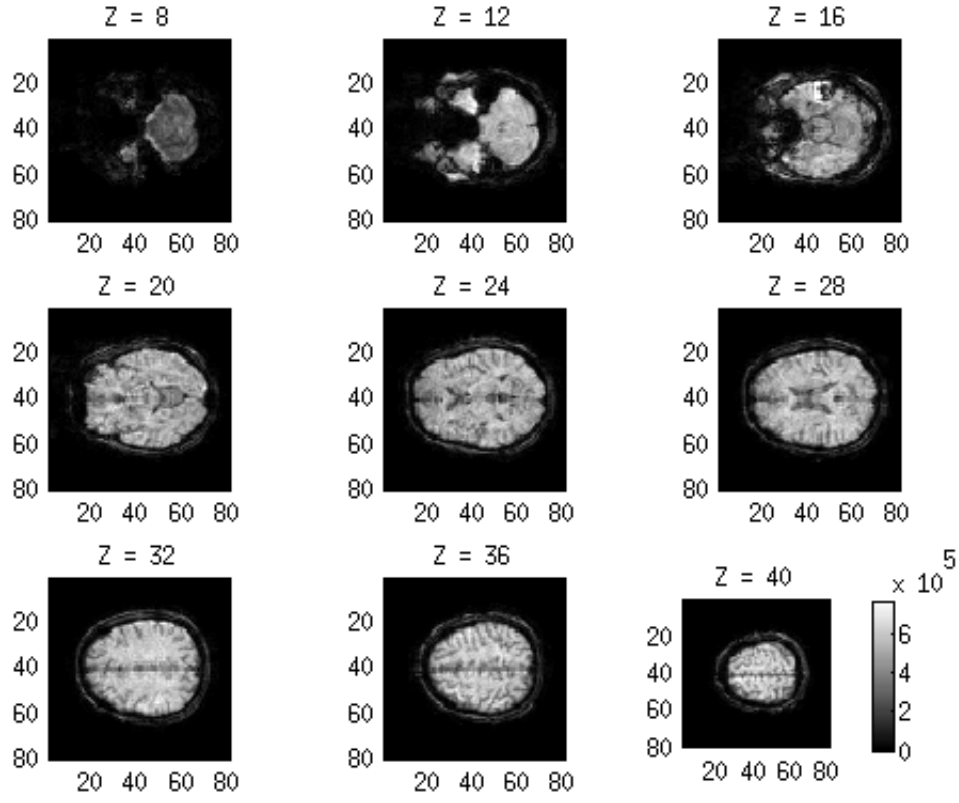
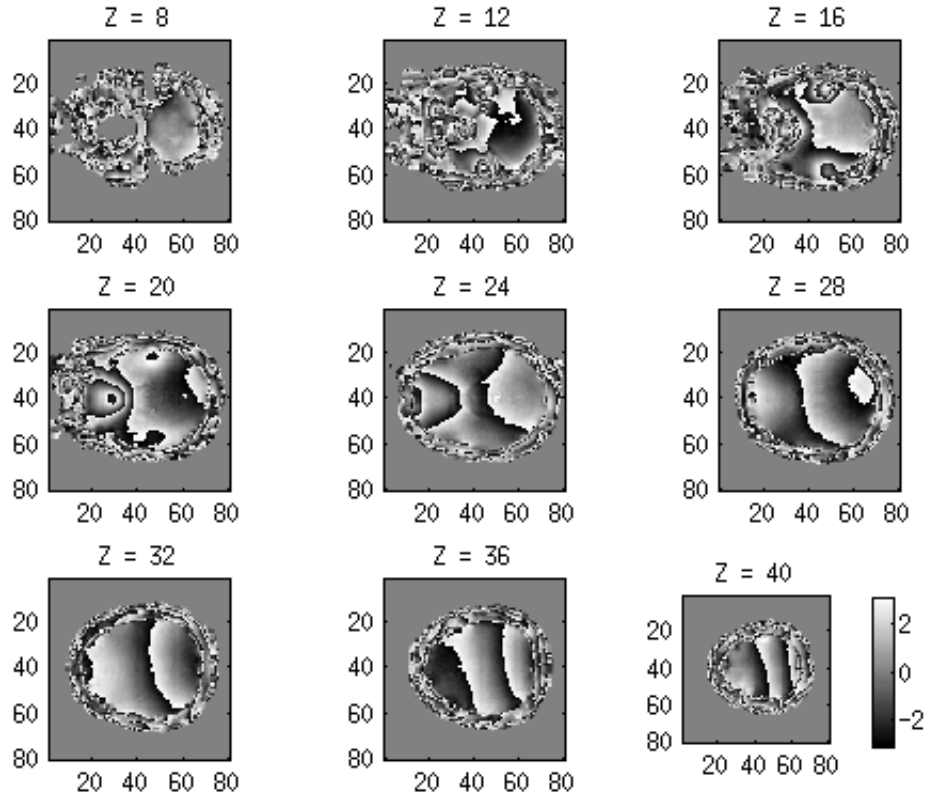


Figure 56. (a) Magnitude and (b) phase image volumes of the output after SENSE reconstruction with reduction rate 2 using sensitivity map B.



(a)



(b)

Figure 57. (a) Magnitude and (b) phase image volumes of the output after SENSE reconstruction with reduction rate 2 using sensitivity map C.

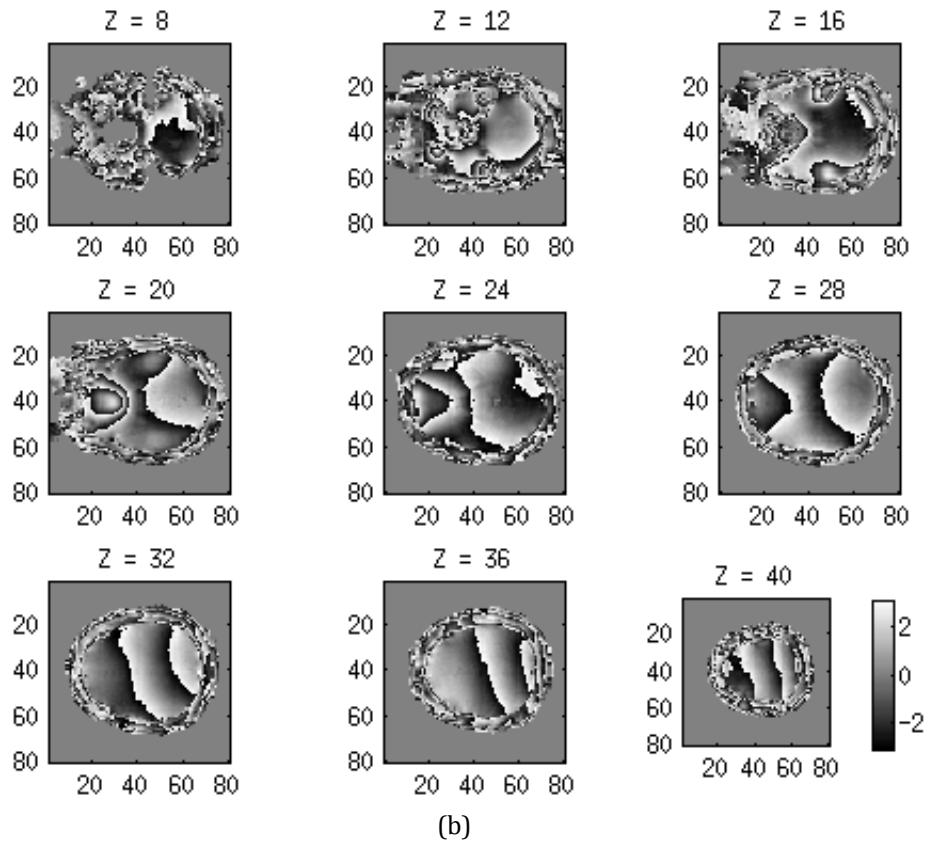
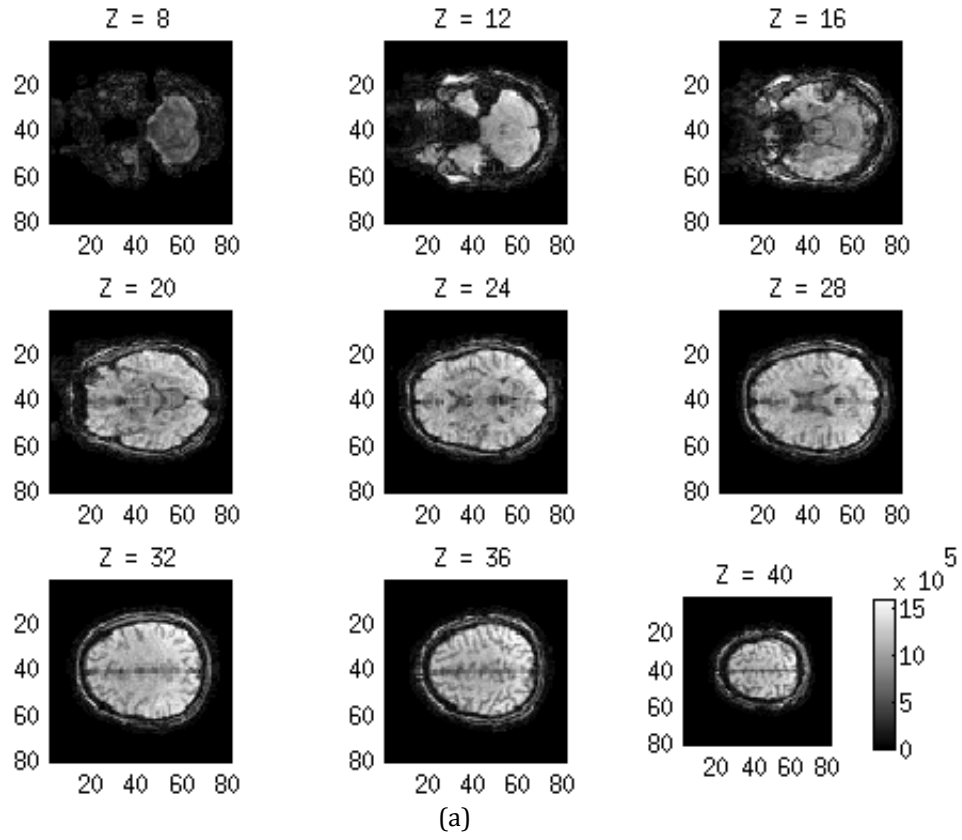


Figure 58. (a) Magnitude and (b) phase image volumes of the output after SENSE reconstruction with reduction rate Z using sensitivity map D.

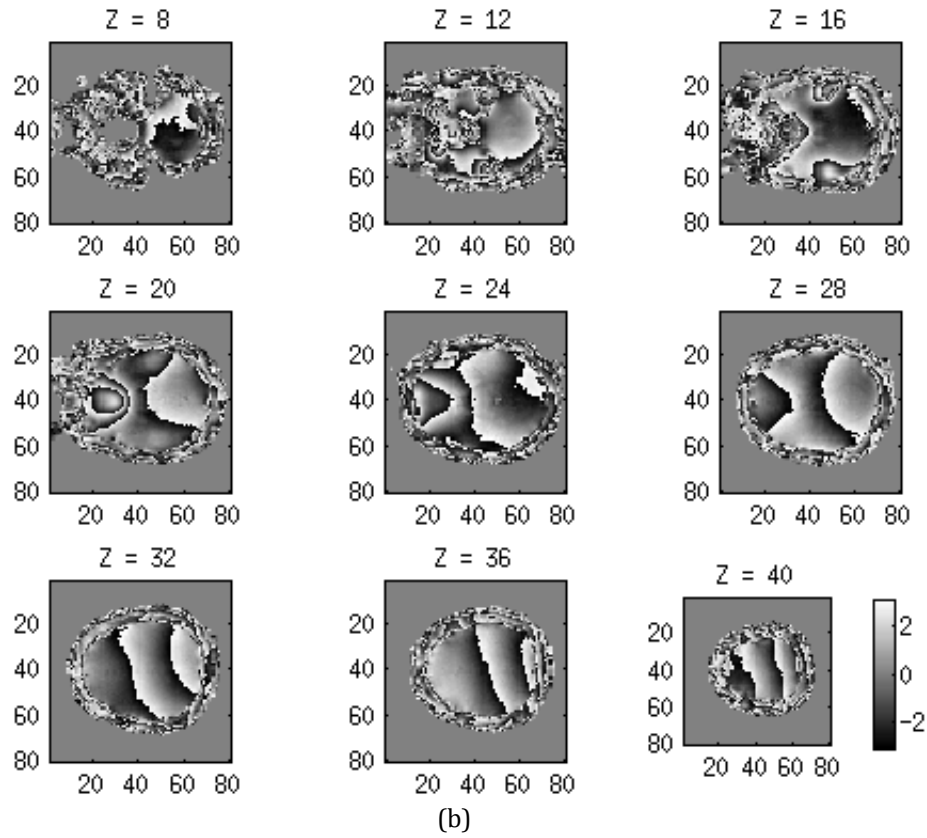
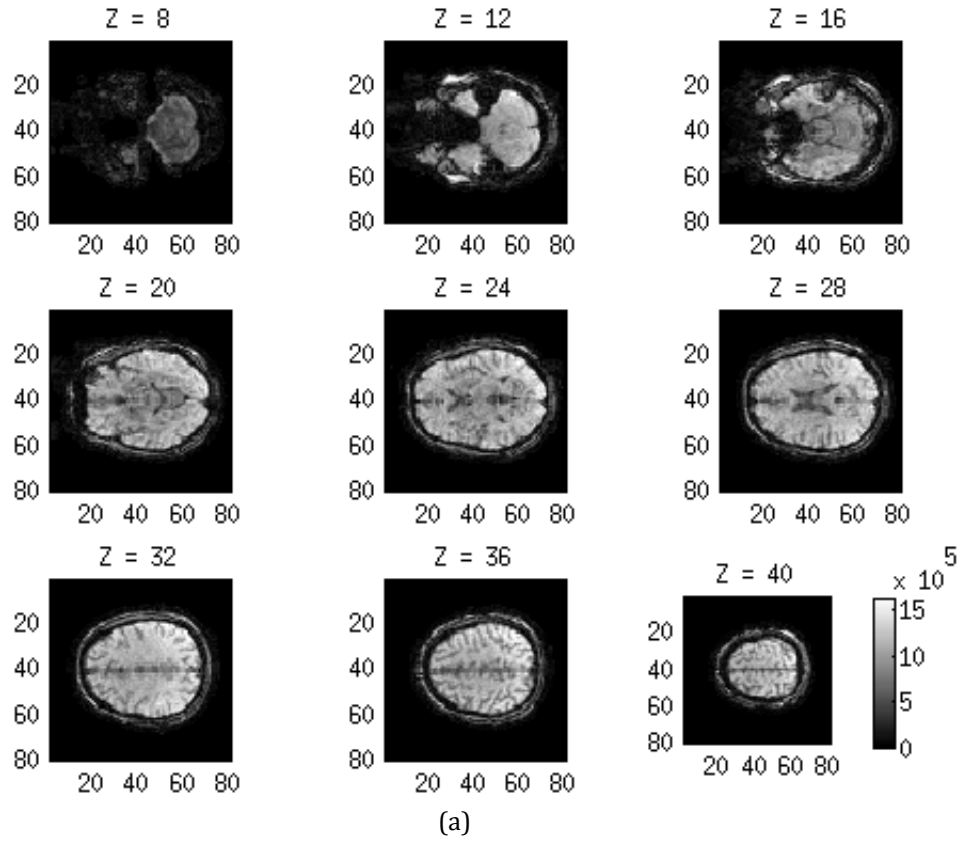


Figure 59. (a) Magnitude and (b) phase image volumes of the output after SENSE reconstruction with reduction rate 2 using sensitivity map E.

Reduction Rate 4

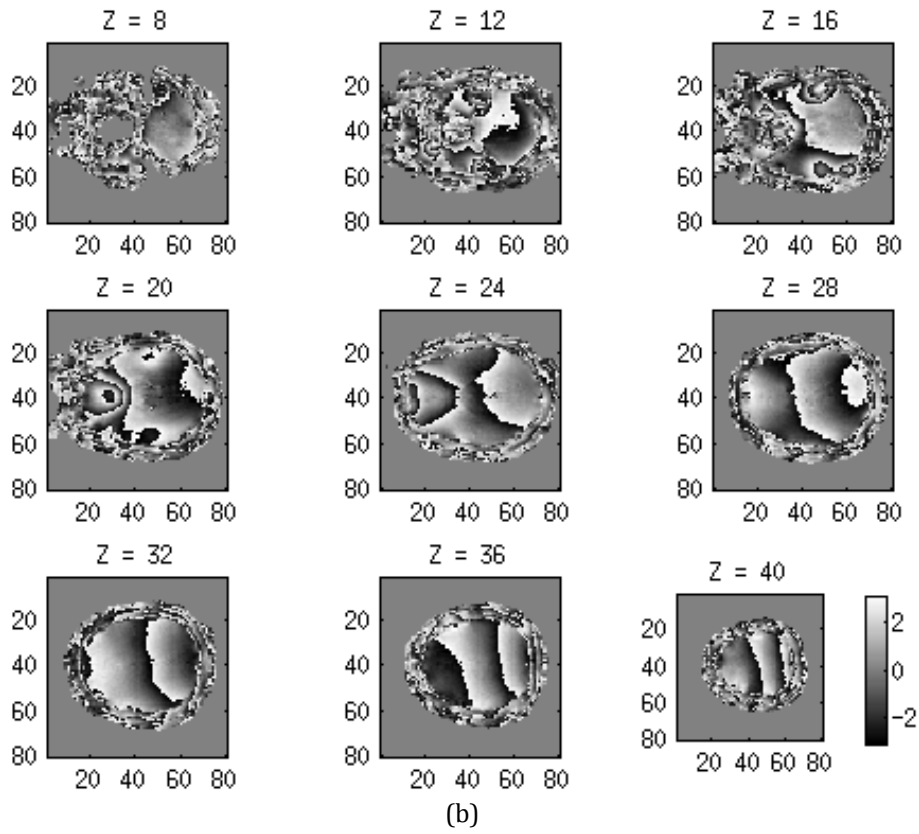
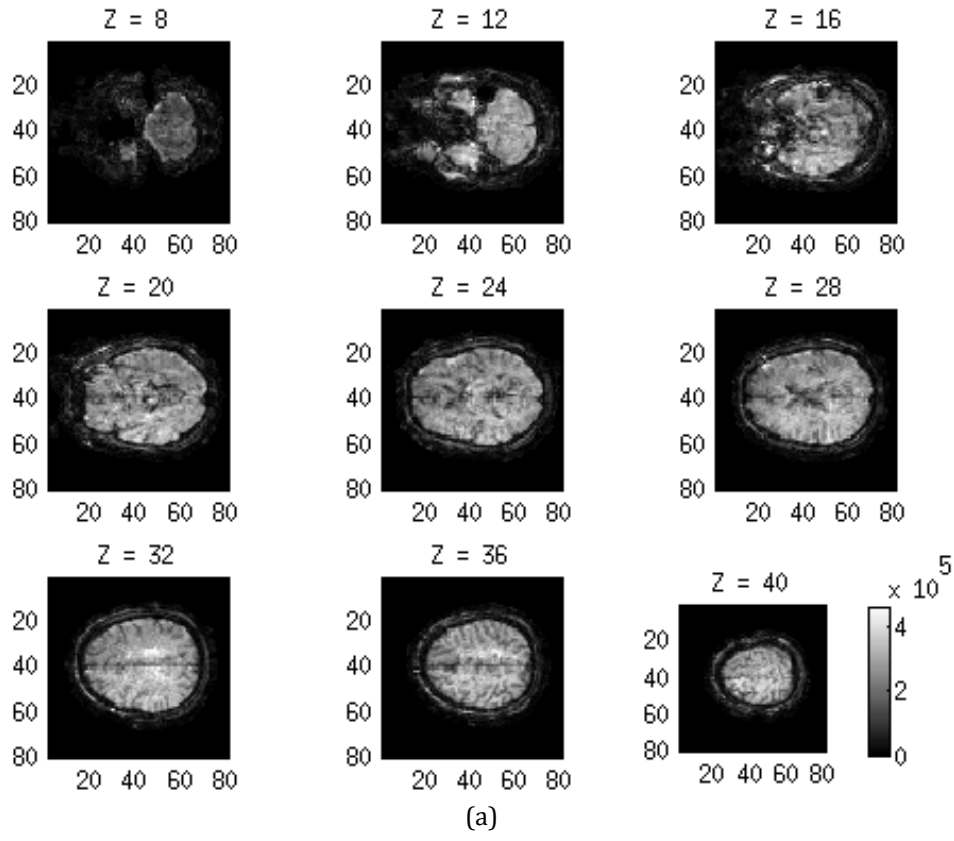


Figure 60. (a) Magnitude and (b) phase image volumes of the output after SENSE reconstruction with reduction rate 4 using sensitivity map A.

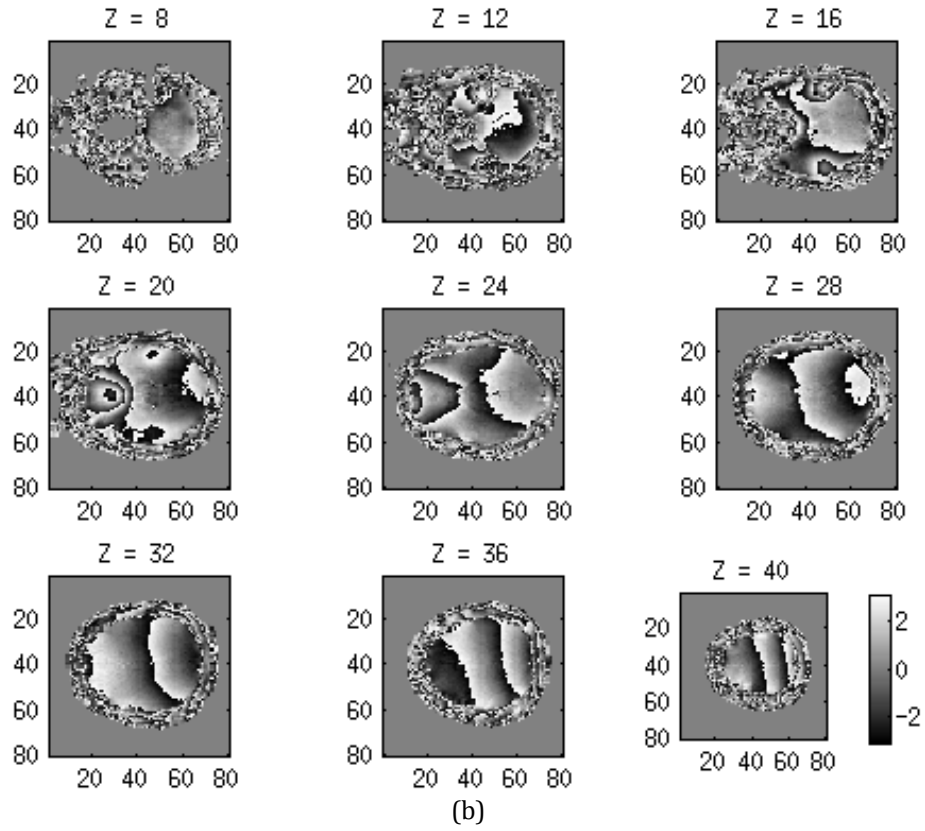
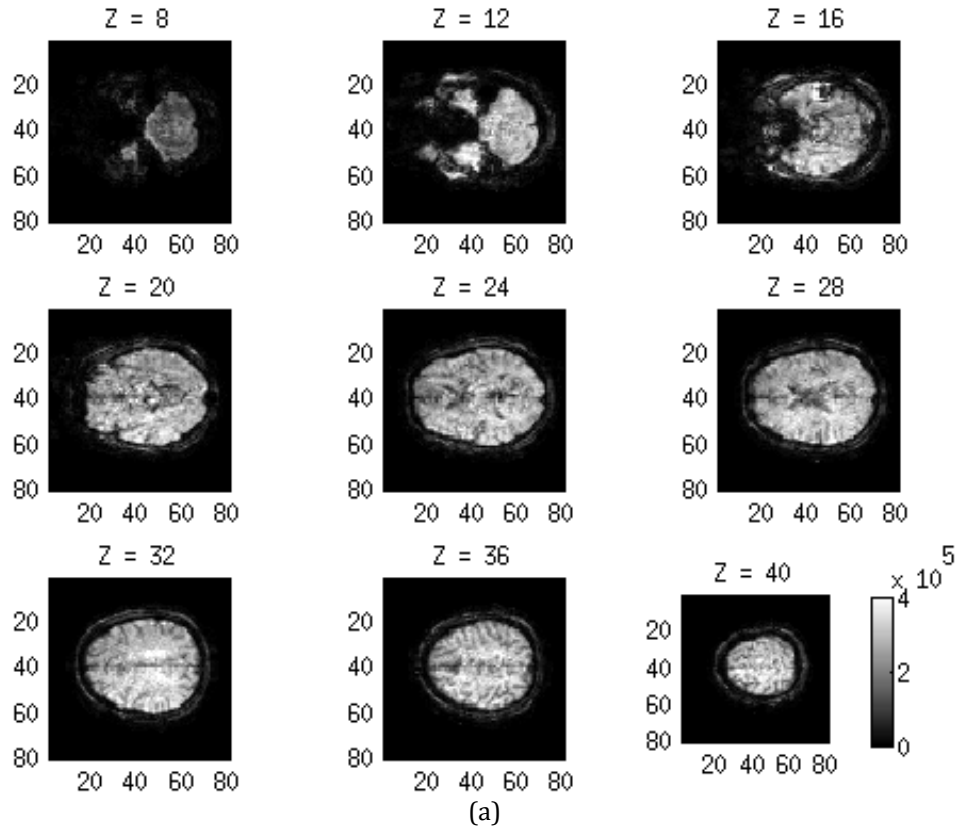


Figure 61. (a) Magnitude and (b) phase image volumes of the output after SENSE reconstruction with reduction rate 4 using sensitivity map B.

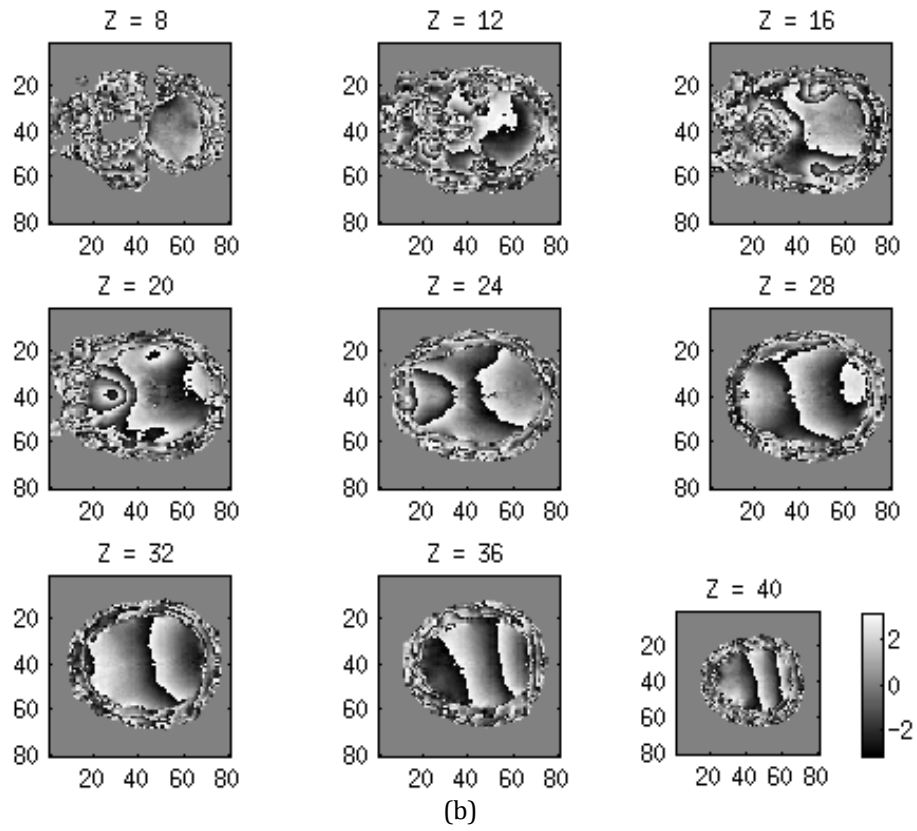
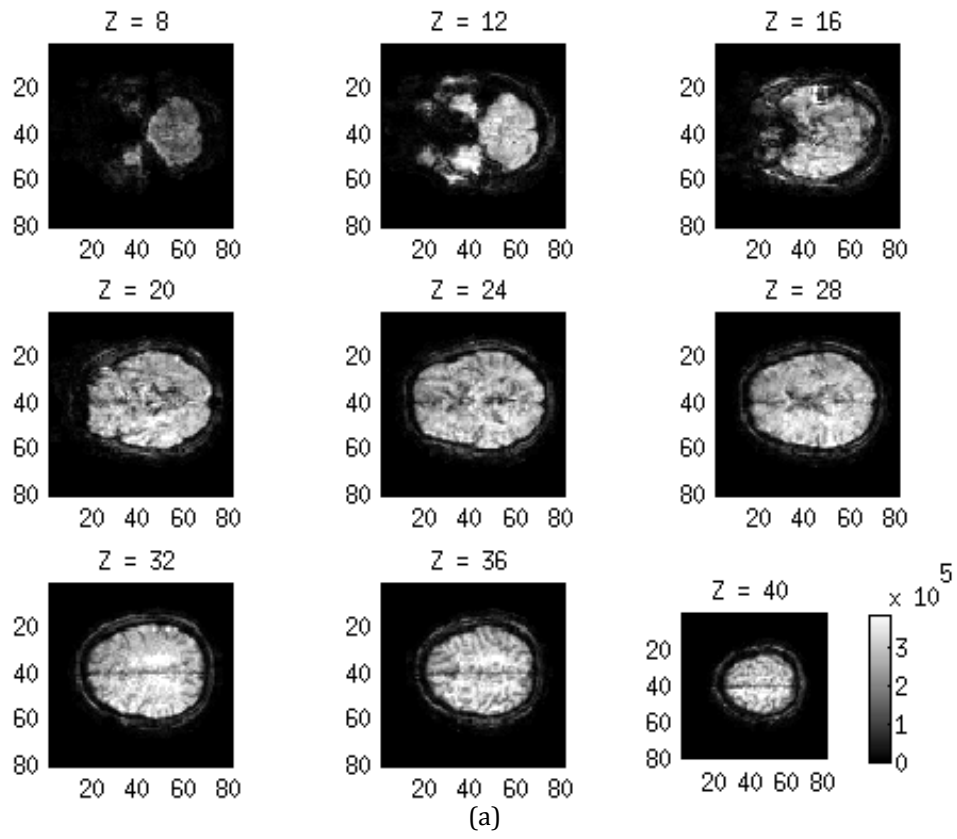


Figure 62. (a) Magnitude and (b) phase image volumes of the output after SENSE reconstruction with reduction rate 4 using sensitivity map C.

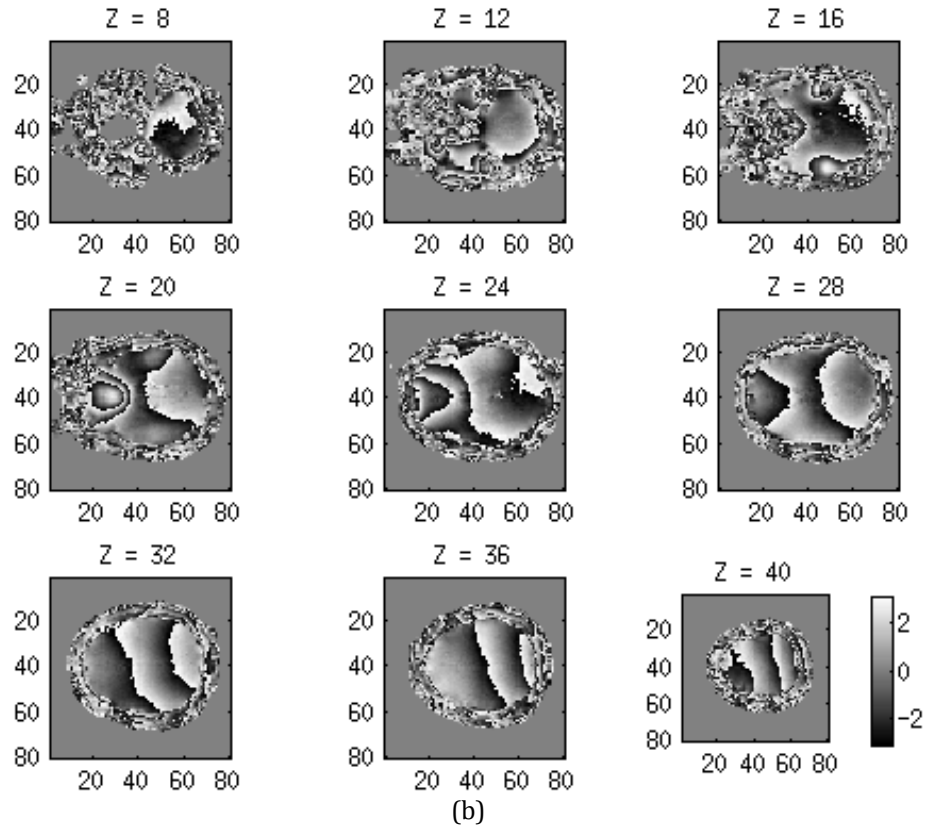
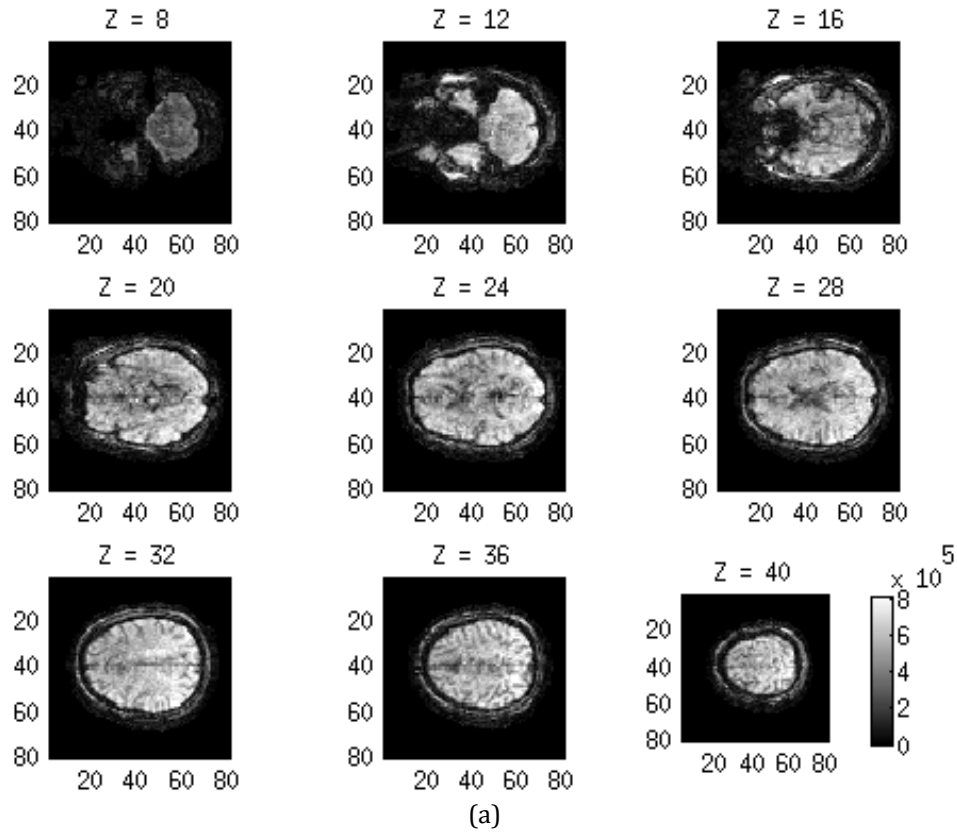


Figure 63. (a) Magnitude and (b) phase image volumes of the output after SENSE reconstruction with reduction rate 4 using sensitivity map D.

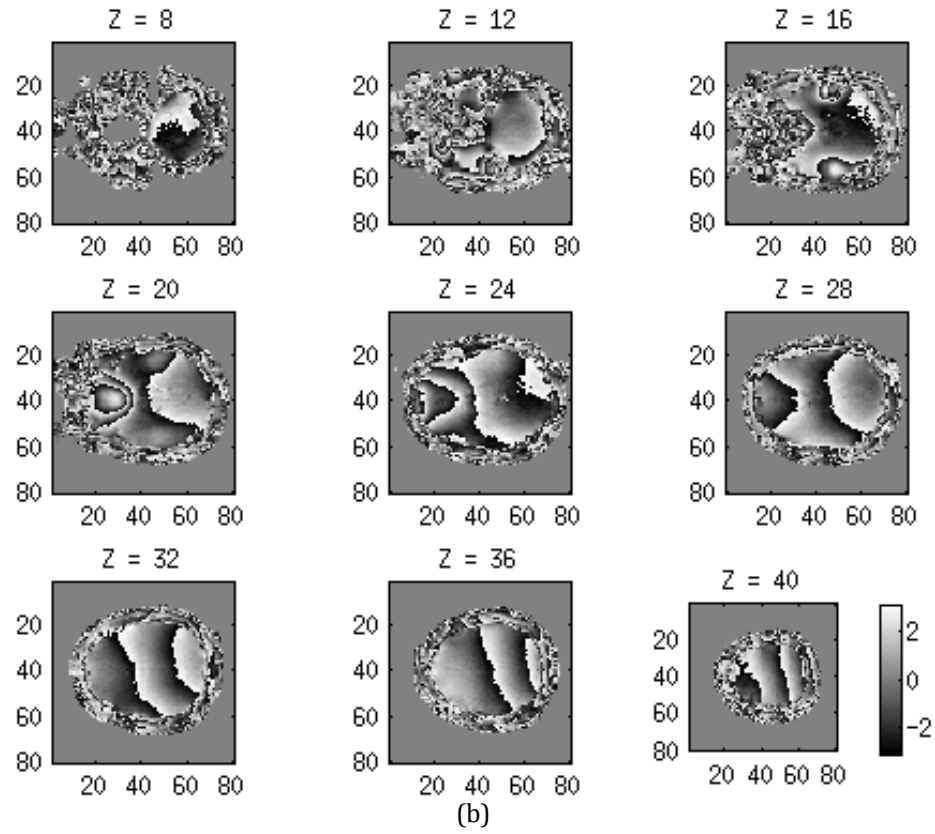
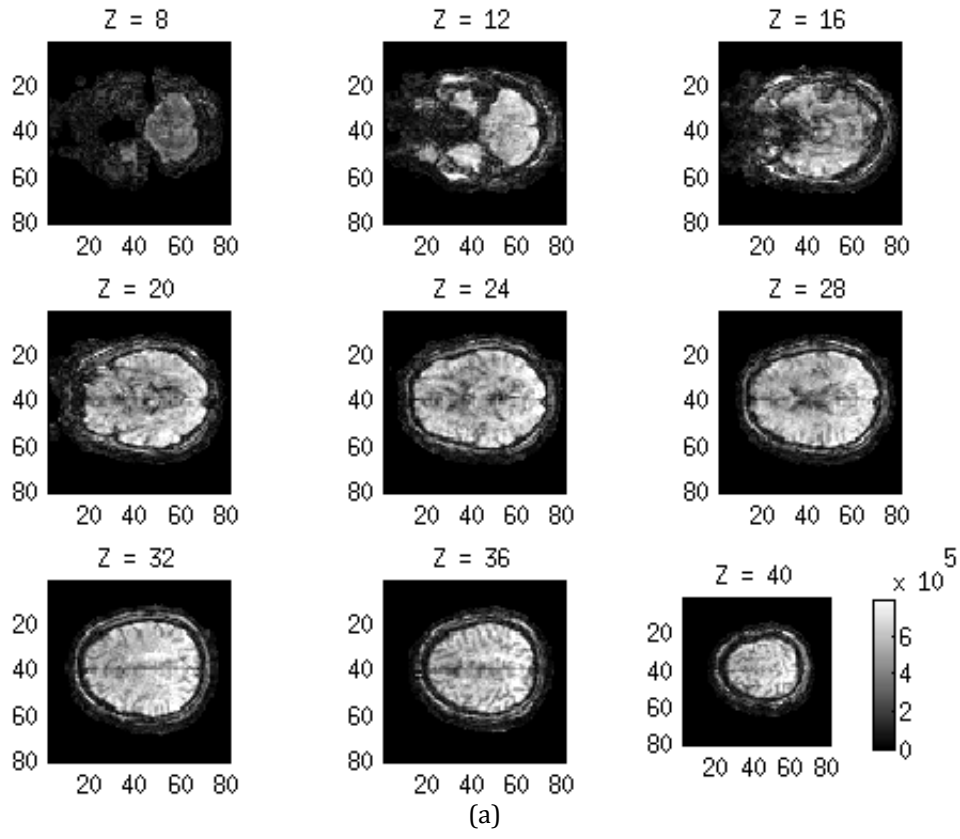


Figure 64. (a) Magnitude and (b) phase image volumes of the output after SENSE reconstruction with reduction rate 4 using sensitivity map E.